Investigating the large N limit of SU(N) Yang-Mills gauge theories on the lattice

DISSERTATION

zur Erlangung des akademischen Grades

doctor rerum naturalium
(Dr. rer. nat.)

im Fach Physik
Spezialisierung: Theoretische Physik

eingereicht an der
Mathematisch-Naturwissenschaflichen Fakultät
der Humboldt-Universität zu Berlin

von

Herrn M.Sc. Miguel Francisco García Vera

Präsident der Humboldt-Universität zu Berlin
Prof. Dr.-Ing. Dr. Sabine Kunst

Dekan der Mathematisch-Naturwissenschaftlichen Fakultät
Prof. Dr. Elmar Kulke

Gutachter/innen:
1. Prof. Dr. Rainer Sommer
2. Prof. Dr. Ulrich Wolff
3. Prof. Dr. Biagio Lucini

Tag der mündlichen Prüfung: 02.06.2017

Abstract

In this thesis we present results for the topological susceptibility χ_{YM}, and investigate the property of factorization in the 't Hooft large N limit of SU(N) pure Yang-Mills gauge theory. The study of χ_{YM} is motivated by the Witten-Veneziano relation, which explains the large mass of the η' meson when compared to the rest of light pseudoscalar mesons. A key component in the lattice gauge theory computation of χ_{YM} is the estimation of the topological charge density correlator, which is affected by a severe signal to noise problem. To alleviate this problem, we introduce a novel algorithm that uses a multilevel type approach to compute the correlation function of observables smoothed with the Yang-Mills gradient flow. When applied to the topological charge density and the Yang-Mills energy density, our results agree with a scaling of the error proportional to $1/n$, instead of the $1/\sqrt{n}$ scaling from traditional Monte-Carlo simulations, where n is the number of independent measurements.

We compute the topological susceptibility in the pure Yang-Mills gauge theory for the gauge groups with $N = 4, 5, 6$ and three different lattice spacings. In order to deal with the freezing of topology, we use open boundary conditions, which allows us to go to finer lattice spacings when compared to previous works in the literature. In addition, we employ the theoretically sound definition of the topological charge density through the gradient flow. Our final result for the dimensionless quantity $t_0^2\chi_{\text{YM}} = 7.03(13) \times 10^{-4}$ in the limit $N \to \infty$, represents a new quality in the verification of the Witten-Veneziano formula.

Lastly, we use the lattice formulation to verify the factorization of the expectation value of the product of gauge invariant operators in the large N limit. We work with Wilson loops smoothed with the Yang-Mills gradient flow and simulations up to the gauge group SU(8). Loops at different N are matched using the scale t_0, and thanks to the favourable renormalization properties of the flow, we study factorization in the continuum. Our extrapolations to $1/N \to 0$ are compatible with factorization, and, for our particular observables, we observe the coefficients of the $1/N$ expansion to be of O(1). Our data allow us not only to verify factorization, but also to test the $1/N$ scaling up to very high precision, where we find it to agree very well with a series in $1/N^2$ as predicted originally by 't Hooft for the case of the pure Yang-Mills gauge theory.

Keywords:
Lattice QCD, large N limit, topological susceptibility, multilevel algorithm, factorization

Zusammenfassung

In dieser Arbeit präsentieren wir Resultate der topologischen Suszeptibilität χ_{YM} und untersuchen die Faktorisierung der reinen SU(N) Yang-Mills Eichtheorie im 't Hooft'schen Grenzwert großer N. Die Bestimmung von χ_{YM} wird motiviert durch die Witten-Veneziano Relation, die die große Masse des η'-Mesons im Verleich zu den restlichen leichten pseudoskalaren Mesonen erklärt. Ein entscheidender Teil der Berechnung von χ_{YM} in der Gittereichtheorie ist die Abschätzung des topologischen Ladungsdichtekorrelators, die durch ein schlechtes Signal-Rausch-Verhältnis beeinträchtigt ist. Um dieses Problem abzuschwächen, führen wir einen neuen, auf einem mehrstufigen Vorgehen beruhenden Algorithmus ein, um die Korrelationsfunktion von Observablen zu berechnen, die mit dem Yang-Mills Gradientenfluss geglättet wurden. Angewandt auf die topologische Ladungsdichte und die Yang-Mills Energiedichte erhalten wir Ergebnisse, deren Fehlerskalierung mit $1/n$ übereinstimmt anstatt mit der $1/\sqrt{n}$ Skalierung traditioneller Monte-Carlo Simulationen, wobei n die Anzahl der unabhängigen Messungen ist.

Wir bestimmen die topologische Suszeptibilität in der reinen Yang-Mills Eichtheorie für Eichgruppen mit $N = 4, 5, 6$ und drei verschiedenen Gitterabständen. Um die Einfrierung der Topologie zu umgehen, wenden wir offene Randbedingungen an, durch die wir in der Lage sind, bis jetzt in der Literatur unerreicht kleine Gitterabstände simulieren zu können. Zusätzlich wenden wir die korrekte Definition der topologischen Ladungsdichte durch den Gradientenfluss an. Unser Endresultat der dimensionslosen Größe $t_0^2\chi_{\text{YM}} = 7.03(13) \times 10^{-4}$ im Limes $N \to \infty$ repräsentiert eine neue Qualität in der Verifikation der Witten-Veneziano Formel.

Schließlich benutzen wir die Gitterformulierung, um die Erwartungswertfaktorisierung des Produkts eichinvarianter Operatoren im Grenzwert großer N zu verifizieren. Wir arbeiten mit durch den Yang-Mills Grandientenfluss geglätteten Wilsonschleifen und Simulationen bis zur Eichgruppe SU(8). Schleifen bei unterschiedlichen N werden mit Hilfe der Skala t_0 angepasst und dank der günstigen Renormierungseigenschaften des Flusses untersuchen wir die Faktorisierung im Kontinuum. Unsere Extrapolationen zu $1/N \to 0$ sind in Übereinstimmung mit Faktorisierung und wir erhalten Koeffizienten der $1/N$-Entwicklung unserer Observablen von O(1). Unsere Daten erlauben uns nicht nur die Verifizierung der Faktorisierung, sondern auch einen hochpräzisen Test des $1/N$ Skalierungsverhaltens. Hier finden wir, wie ursprünglich vorhergesagt durch 't Hooft für den Fall der reinen Yang-Mills Eichtheorie, eine sehr gute Übereinstimmung mit einer Reihe in $1/N^2$.

Schlagwörter: Gitter-QCD, Grenzwert großer N, topologische Suszeptibilität, mehrstufiger Algorithmus, Faktorisierung

Contents

1. Introduction

The 20th century was without a doubt one of the most fruitful periods in the history of physics. The discovery of both general relativity and (especially) quantum mechanics has had a tremendous impact not only on the scientific world, but also on our everyday life. Most of the technology that we use today, is in some way or another connected to the physics of the quantum world, and it is remarkable that such a wide range of phenomena can be explained by a single theory. The broader scope of this thesis is precisely the quantum theory of elementary particle physics, which can be understood in a unified way through the so-called Standard Model (SM) of particle physics.

The Standard Model is a local quantum field theory (QFT) with the gauge group SU(3)×SU(2)×U(1). If we add to this the existence of the 6 quarks, 6 leptons (and their corresponding antiparticles) and the Higgs Field, we are in a position to describe all the particles and interactions that form the visible matter in the universe. However, in spite of knowing all the constituents and the basic theory that governs their interactions, obtaining analytical predictions is still an enormous challenge, and in most cases one has to rely on approximations such as perturbation theory or effective field theories. One particularly challenging ingredient of the SM is the subject of study of Quantum Chromodynamics (QCD), which deals with the strong sector, represented by the SU(3) colour group.

Not considering the quark masses, QCD can be described by a single parameter, the coupling strength $\alpha_s = g^2/4\pi$. A well known feature is the fact that it is a running coupling, i.e., it depends on the energy scale of the process being considered. In the case of QCD, this implies that there exist two clearly different regimes, on the one hand, at low energies (or large distances), the theory is confining, which is the reason why quarks are always observed in bound colourless states in matter. On the other hand, when nucleons are probed with very energetic photons, the quarks inside of them transport the energy as if they were free particles, which is a manifestation of the property of asymptotic freedom. The energy scale which is associated with the splitting of these two different regimes is given in terms of the Λ parameter of QCD, which is on the order of a few hundred MeV.

At large energies, the small value of α_s allows the use of perturbative techniques; in contrast, at low energies one must find a way to obtain predictions non-

pertubatively. Up to date, the lattice formulation of QCD is the most successful way to not only obtain non-perturbative predictions, but also to formulate quantum field theories in a formal and mathematically well defined manner. The main idea originated from the pioneering work of Wilson in 1974 [1], and has since then evolved to become a branch of particle physics on its own.

In simple terms, the lattice formulation of QCD consists in discretizing the spacetime, so the path integral is defined on a countable set of points. If in addition, the theory is restricted to live on a finite size box, the problem consists in evaluating a finite (but in practice very large) number of integrals. The final ingredient is to work in the Euclidean formulation of the theory, where the probability density looks very similar to the Boltzmann weight factor from statistical mechanics. Importance sampling then makes it possible to compute expectation values up to very high accuracy with a manageable computational effort. With the current algorithmic development and the use of some of the top computer centres in the world, lattice QCD is now able to provide predictions which can be directly contrasted with experiments and provide crucial input for checks of the Standard Model.

Lattice QCD has without a doubt contributed enormously to the understanding of non-perturbative phenomena. However, in many cases a more analytical way to "solve" QCD would be desirable. Notably, one of the Millenium Problems[1] is concerned with the existence of the mass gap in non-abelian Yang-Mills gauge theories, which only supports the fact that solving QCD is on the forefront of particle physics interest. In this sense, it is useful to study theories similar to QCD which could help to understand some of the purely theoretical and phenomenological properties that we observe in the real world. One such theory was coincidentally also introduced in 1974 by 't Hooft [2] in his groundbreaking work about the large N limit of SU(N) Yang-Mills gauge theories.

In the original paper, 't Hooft considered the limit on which the rank of the gauge group N is taken to infinity while the rescaled bare coupling $\lambda = g^2 N$ is kept constant. Remarkably, in this limit the theory simplifies in many ways and it was originally thought that it could be solved analytically. Unfortunately, this has not been the case for the SU(N) gauge theory in four dimensions. In spite of this, the study of the 't Hooft limit of QCD has provided an explanation for phenomena such as the OZI rule or the large mass of the η' meson.

From a more theoretical perspective, the interest on large N QCD has grown on the recent years due to its connection to the gauge-string duality. The connection was already suggestive from the original work of 't Hooft, where it was shown that the Feymann diagrams can be organized in powers of $1/N$ according to their topological nature, in a similar way to the expansion in the string coupling g_s in string theory. More recently, in the seminal works of Refs. [3, 4, 5], an explicit correspondence between Type II B string theory and $\mathcal{N} = 4$ U(N) Yang-Mills theory was

[1] www.claymath.org/millenium-problems/yang–mills-and-mass-gap

conjectured, on which the large N limit corresponds to a classical limit on the string side. In this context, the large N limit offers a good framework to further explore the consequences of the gauge-string duality. We do not go further into this topic and the reader is invited to dive into the vast literature on this subject [6, 7].

Clearly, one can use the lattice to study the large N limit of gauge theories. This however, turns out to be very challenging due to the increase in the number of degrees of freedom at larger N, but when feasible, it can provide valuable input to both phenomenologists and theorists alike. We would also like to mention that some of the simplifications in the limit $N \to \infty$ actually make it simpler to simulate the theory on the lattice, given that the colour degrees of freedom can be interchanged with the spatial degrees of freedom, and large N gauge theories can be simulated on very small lattices.

Another simplification in the large N limit is the fact that quark loop effects are suppressed (quenched approximation). Quenched simulations are significantly simpler to put in a computer as one does not have to deal with the fermionic part of the action. Nowadays, state of the art lattice QCD simulations include full dynamical quarks, but in the first years of lattice QCD, most simulations were done in the quenched limit, mainly due to computational limitations. In general, the initial quenched calculations provided results which are very close to the ones obtained in the full theory [8]. In the large N limit, the quenched case is not an approximation, so it is feasible to simulate the quenched theory at various finite values of N and then extrapolate to $N \to \infty$. The case of the meson spectrum for example, has been computed in this way in Ref. [9] working up to $N = 17$ (see also references therein).

A common factor across all the large N simulations is the incredible confirmation of the $1/N$ scaling predicted by 't Hooft. Notice that this is not trivial, as this constitutes a non-perturbative verification of the scaling expected from a perturbative analysis. A large number of studies have looked at the N dependence of different quantities, such as baryon masses [10], glueball masses [11] or the spectrum of confining flux tubes on a finite size lattice [12]. A rather recent review of all the developments in large N on the lattice has been presented in Ref. [13] and the reader is invited to go through the references presented there.

In this work, we add to the literature on the large N limit of QCD by focusing on two particular aspects. The first one is related to the $\mathrm{U(1)_A}$ problem, which finds an elegant solution in the large N framework. Basically, the quantum anomaly that breaks the global $\mathrm{U(1)_A}$ symmetry in QCD is related to the topological properties of the underlying theory, and it connects the mass of the η' meson to the topological susceptibility χ_{YM} in the large N limit. We leave the discussion of the $\mathrm{U(1)_A}$ problem for Chapter 3, while we present our computation of χ_{YM} on Chapter 6. It is worth noting that the introduction of the lattice formulation is necessary in order to compute χ_{YM}, which is not accessible experimentally.

The second problem we want to tackle in this work has to do with the property of factorization in the large N limit. For a large class of operators, the large N limit

implies that their correlation functions are dominated by disconnected diagrams. In particular, this suggests that quantum fluctuations are suppressed in the 't Hooft limit. This observation led to the idea that a single gauge configuration (up to gauge transformations), or "master field", would saturate the path integral [14, 15]. Although it was shown that this idea in its simplest form was not applicable to large N QCD, it already pointed out to the idea of volume independence, which has survived much longer.

Volume independence is made evident when looking at the Makeenko-Migdal equations for the expectation value of closed Wilson loops. Such equations form a closed set of Schwinger-Dyson equations which require some regularization procedure to be made sense of. Using the lattice regularization, the authors in [16] showed that provided factorization and other conditions are met, in the large N limit, the equations are independent of the space-time volume. Using this fact, in principle one can study the 't Hooft limit of SU(N) Yang-Mills theory on arbitrarily small volumes. Clearly this makes lattice investigations of the large N limit of gauge theories a more viable proposal. In this work, we examine the property of factorization, which is a necessary condition for volume reduction to work.

In addition to the more physics oriented part of this work, we have also explored some algorithmic developments which have been (partially) used to obtain some of the results presented in this thesis. In particular, we were interested in the type of multi-level algorithms [17, 18] which have shown to have a great potential in speeding up lattice computations.

The organization of this thesis is as follows: in Chapter 2 we review the fundamentals of the 't Hooft large N limit and discuss the property of factorization. In Chapter 3 we look into the $\mathrm{U}(1)_{\mathrm{A}}$ problem and how it links the topological susceptibility χ_{YM} to the mass of the η' meson. In Chapter 4 we present the fundamentals of the lattice formulation of SU(N) Yang-Mills gauge theories. Then, in Chapter 5 we focus on the multi-level algorithm and describe a way to make it compatible with observables smoothed with the Yang-Mills gradient flow, at least in the pure gauge theory case. In Chapter 6 we present our results for the computation of the large N limit of χ_{YM} on the lattice. Next, in Chapter 7, our results concerning factorization of smooth Wilson loops are presented. Finally, in Chapter 8 we summarise our work. We leave for the appendix the presentation of the code produced as part of this thesis.

2. The large N limit of SU(N) Yang-Mills gauge theories

The focus of this thesis is a generalization of QCD on which the gauge group SU(3) is exchanged by SU(N). The rank N of the group is taken as a free parameter, and as pointed out by 't Hooft in 1974 [2], in the limit when the number of colours $N \to \infty$, the theory simplifies in many ways. It was hoped that this simplification would make feasible to discover an analytical solution; something that has not yet been accomplished, and (semi-)analytical solutions have only been found in simpler models [19, 20, 21]. Nonetheless, the large N expansion is still a valuable tool to explain several phenomenological properties of QCD, and allows in many cases to get a better theoretical understanding of the underlying physics.

2.1 The large N topological expansion

We start from the Lagrangian density in Euclidean space-time for an SU(N) Yang-Mills gauge theory with N_{f} fermion fields in the fundamental representation, which can be written in the following way

$$\mathcal{L} = -\frac{1}{2}\,\mathrm{Tr}\left(F_{\mu\nu}F_{\mu\nu}\right) + \sum_{f=1}^{N_{\mathrm{f}}} \bar{\Psi}_f \left(\gamma_\mu D_\mu + m_f\right) \Psi_f \,, \tag{2.1}$$

where Ψ represents a fermionic field and the bosonic part is written in terms of the gauge connection A_μ by means of $F_{\mu\nu} = \partial_\mu A_\nu - \partial_\nu A_\mu + g\left[A_\mu, A_\nu\right]$. The covariant derivative is written as $D_\mu = \partial_\mu + gA_\mu$, and $A_\mu = A^a_\mu T^a$ is given in terms of the anti-hermitian generators of the $\mathfrak{su}(N)$ Lie algebra T^a, which are normalized such that $\mathrm{Tr}\left(T^a T^b\right) = -\frac{1}{2}\delta^{ab}$.

As shown by 't Hooft , it turns out that if one wants to consider the theory at $N \to \infty$, a sensible limit is obtained when the gauge coupling $g \to 0$ at the same time. To see the way it works, it is convenient to first introduce the double line notation for Feynman diagrams. Considering the relation between the lie algebra generators

$$\sum_{a=1}^{N^2-1} (T^a)^{ij} (T^a)^{kl} = \frac{1}{2}\left(\delta^{il}\delta^{kj} - \frac{1}{N}\delta^{ij}\delta^{kl}\right) , \tag{2.2}$$

the free propagator $\left\langle A_\mu^{ij}(x) A_\nu^{kl}(y)\right\rangle \propto \delta^{il}\delta^{kj}$, where the second term in Eq. (2.2) vanishes in the limit $N \to \infty$. Similarly, keeping track of the colour index for the free fermionic propagator one has $\left\langle \Psi^i(x)\bar{\Psi}^j(y)\right\rangle \propto \delta^{ij}$. Schematically this is shown by representing each Kronecker delta by an oriented arrow

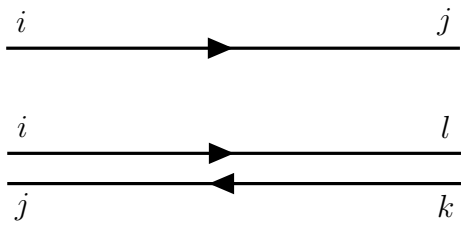

Using this notation is extremely useful if we are interested in keeping track of the powers of N carried by any given Feynman diagram. Basically, every closed index loop in the double line notation includes a sum over an independent colour index, so it gives a power of N. To showcase how this works, consider the diagrams in Figure 2.1, which provide corrections to the gluon self-energy. On the left, the diagrams are presented in the standard notation, while on the right, they are expressed using the 't Hooft double line notation. Let us now naively count the powers of N for each of them. Including the multiplicity associated to the degrees of freedom of the external gluons, the upper diagram is proportional to N^3 (N^2 coming from the external degrees of freedom and an extra power of N for the closed index loop), while the diagram on the bottom, which includes one quark loop, is only proportional to N^2 (no internal index loops). This simple analysis already shows one of the most remarkable properties of large N QCD, and it is the fact that quark loop effects are suppressed at large N.

In his original paper, 't Hooft noticed that $1/N$ can be used as an expansion parameter, and diagrams can be organized according to their topological properties. The proof goes order by order in perturbation theory. Using the double line notation, consider the amplitude for a diagram with V_3 three point vertices, V_4 four point vertices, P propagators and F index loops. The diagram can be given a topological meaning by comparing it to a polyhedron, where every index loop F forms a facet, P form the edges, and each vertex V_i is also a vertex in the figure. Then, using Euler's formula

$$F - P + V = 2 - 2H , \tag{2.3}$$

where H is the genus of the polyhedron and V is the sum of vertices, 't Hooft showed that the amplitude $\mathcal{A}$ for such diagram is given by

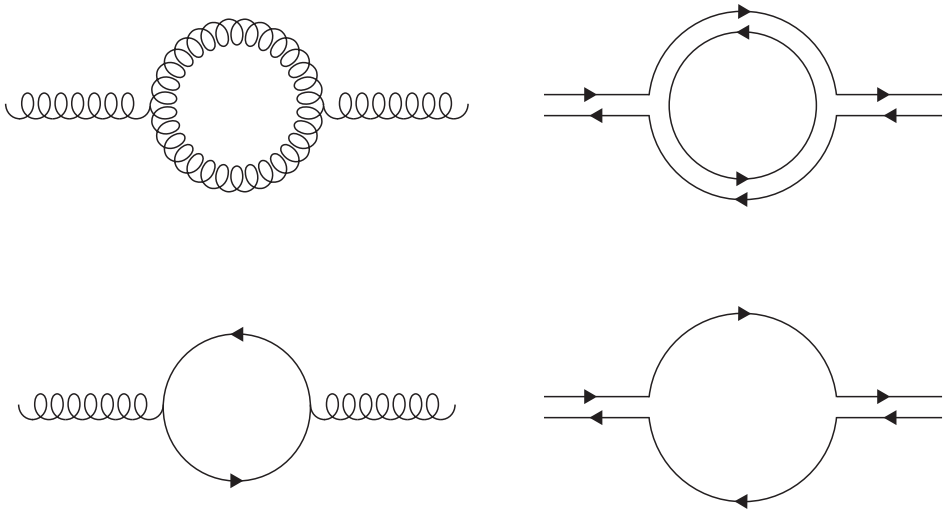

Figure 2.1: Loop corrections to the gluon self-energy. On the left, we show the diagrams using the standard notation, while on the right we show them using the double line notation. The diagram including a quark loop is suppressed by a power of $1/N$.

$$\mathcal{A} \propto g^{V_3+2V_4} N^F = \left(g^2 N\right)^F \left[\left(g^2 N\right)^{-1} N\right]^{2-2H} . \tag{2.4}$$

The second factor in Eq. (2.4) is purely geometrical, while the first one depends on the number of index loops. The topological expansion from 't Hooft is obtained when the limit $N \to \infty$ is taken while keeping the quantity $\lambda = g^2 N$ fixed, the N dependence is then encoded in the factor N^{2-2H}, which shows that the diagrams can be organized according to their topology. Quark loop effects can be added to Eq. (2.4) by considering that they are represented by a single colour line and can be thought of as a missing face, or a topological boundary. Thus, quark loop effects are suppressed by a factor of $1/N$ as we have shown with an example in Figure 2.1. In the general case of B fermion loops, one must add a factor of N^{-B} to Eq. (2.4).

Let us also motivate the definition of $\lambda = g^2 N$ from a different perspective. For a general gauge group SU(N), the β function describes the running of the coupling with respect to an energy scale μ. A sensible large N limit should have a non-divergent β function and ideally preserve the familiar properties form real world QCD, such as asymptotic freedom. To see how this is realized let us look at the leading order formula for the β function which is given by

$$\beta(g) = \mu \frac{\partial g}{\partial \mu} = -\frac{1}{(4\pi)^2} \left(\frac{11N - 2N_\mathrm{f}}{3}\right) g^3 - \frac{1}{(4\pi)^4} \left[\frac{34}{3} N^2 - N_\mathrm{f} \left(\frac{13N}{3} - \frac{1}{N}\right)\right] g^5 + O(g^7) . \tag{2.5}$$

The expression is clearly divergent as $N \to \infty$, at a fixed value of the bare coupling

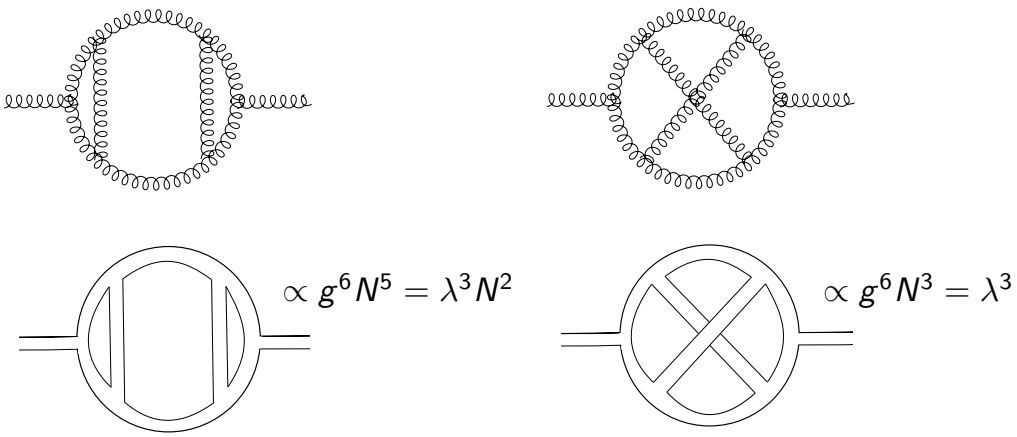

Figure 2.2: Planar (left) and non-planar (right) diagrams contributing the gluon propagator. In the large N expansion, the leading diagrams are planar diagrams.

g. The 't Hooft limit corresponds to the case in which $g \to 0$ such that $\lambda = g^2 N$ is kept fixed. Changing variables, the β function is

$$\beta(\lambda) = \mu \frac{\partial \lambda}{\partial \mu} = -\frac{11 - 2\frac{N_\mathrm{f}}{N}}{24\pi^2}\lambda^2 - \frac{1}{(4\pi^4)}\left[68 - 2\frac{N_\mathrm{f}}{N}\left(13 + \frac{3}{N^2}\right)\right]\lambda^3 + O(\lambda^4)\,, \quad (2.6)$$

where the 't Hooft coupling λ can be considered as the fundamental coupling of the theory. As can be seen from Eq. (2.6), a sensible large N limit can also be obtained if N_f is scaled such that the ratio N_f/N is kept constant. This limit is known as the Veneziano limit [22], and in this scenario fermions contribute at the leading order, so the theory is somewhat more involved than the simpler 't Hooft limit. Notice that as long as $N_\mathrm{f}/N \to 0$, the 't Hooft limit preserves asymptotic freedom, and in particular, for the case of the pure gauge theory, which is our main interest, $N_\mathrm{f} = 0$, so the first two universal coefficients of the β function are N independent.

2.1.1 The planar limit

Notice that the leading contribution in Eq. (2.4) comes from those diagrams with a trivial topology, i.e. diagrams with no holes ($H = 0$). Consider the two upper diagrams in Figure 2.2. Using the double line notation, one can readily obtain the N dependence by counting the number of closed index loops. Although the two diagrams look very similar, the one on the right is suppressed by a power of $1/N^2$ with respect to the one on the left. In the topological expansion, the diagram on the left is called a planar diagram as it can be drawn on a sheet of paper without any line crossings. On the contrary, the one on the right can only be drawn without line crossing on a surface with a hole, such as a torus.

The fact that the leading contribution in the large N limit comes only from planar diagrams motivated several attempts to solve the theory analytically. From a perturbative point of view, the number of planar diagrams increases only exponentially with the loop order, in contrast to the general case where the growth is factorial. Despite these simplifications, an analytical solution to the large N limit of QCD in 3+1 dimensions has not yet been found.

2.2 Factorization

One remarkable feature of gauge theories in the large N limit is the property of factorization. Factorization tells us that given the product of gauge invariant operators $\mathcal{O}_i$, the expectation value of the product is given by

$$\langle \mathcal{O}_1 \dots \mathcal{O}_k \rangle = \langle \mathcal{O}_1 \rangle \dots \langle \mathcal{O}_k \rangle + \mathrm{O}(1/N)\,. \tag{2.7}$$

It is important to mention that Eq. (2.7) holds for a set of "well defined" observables, either local gauge invariant purely gluonic operators, fermionic bilinear operators or closed Wilson loop operators.

The validity of the equation can be readily established by considering the rules for the topological expansion presented in the previous section. An example on how the property follows from the large N counting rules is shown in Figure 2.3. The upper diagram shows a disconnected contribution, where the external line can represent either a quark-antiquark pair production diagram (simply add the corresponding fermionic currents) or a Wilson loop, $W = \mathrm{Tr}\left(\mathcal{P}\, exp\left(ig \int dz^\mu A_\mu(z^\mu)\right)\right)$. On the other hand, the lower diagram represents a connected contribution. Using the double line notation (Figure 2.3 right), it is clear that the connected part is suppressed by a power of $1/N^2$ with respect to the disconnected contribution.

It is desirable to have a non-perturbative proof of factorization. Such idea was discussed in Refs. [23, 24], where the authors use the Makeenko-Migdal loop equations (Schwinger-Dyson equations for the loop average) [25] to prove factorization in a non-pertubative fashion. The key assumption for the proof is the assumption that the solution is unique. Once the equations have been formally defined, one must give a regularization prescription, and as already pointed out in [25], a good choice is to use a lattice regulator. One can write a convenient lattice analog of the Makeenko-Migdal equations and then the continuum limit must be taken in a well defined manner. What this means is rather not clear, as loop observables on the lattice suffer from severe ultraviolet divergences which must be dealt with in some particular fashion.

Another more mathematically oriented proof of factorization is given in Ref. [26] for SO(N) and more recently in Ref. [27] for the more relevant case of SU(N) Yang-Mills gauge theory. The proof is mathematically more rigorous but is limited to the lattice theory in the non-physical strongly coupled regime. Nevertheless, it is

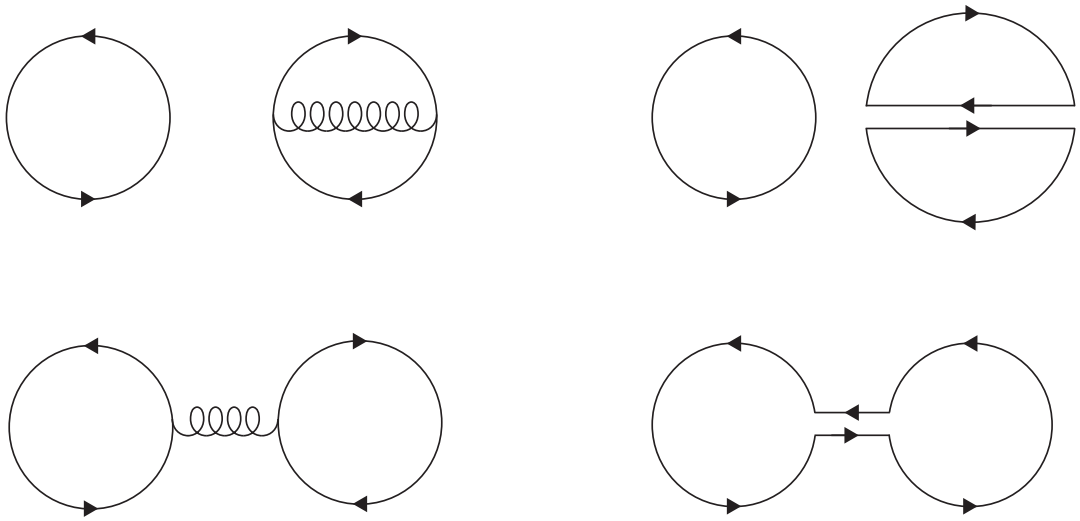

Figure 2.3: Comparison between a disconnected (upper diagrams) and connected (lower diagrams) contribution. By using the double line notation (right), one can readily see that the dominant term comes from the disconnected part which is $\mathrm{O}(g^2N^3) = \mathrm{O}(\lambda N^2)$, while the connected one is $\mathrm{O}(g^2N) = \mathrm{O}(\lambda)$.

interesting to note that the proof is based on a sum over trajectories in a string theory on the lattice, which in a way can be interpreted as one type of string-gauge duality.

Notice that Eq. (2.7) implies that the variance of operators in large N goes to zero

$$\left\langle \mathcal{O}^2 \right\rangle - \left\langle \mathcal{O} \right\rangle^2 = \mathrm{O}(1/N^2)\,. \tag{2.8}$$

Moreover, rescaling the gauge $\sqrt{\lambda/N}A_\mu \to \hat{A}_\mu$ and fermion $\Psi \to \sqrt{N}\hat{\Psi}$ fields, the Lagrangian density from Eq. (2.1) can be rewritten with an overall N factor in front of it. The explicit N factor resembles the case of $\hbar$ in quantum mechanics. In this sense, the large N theory is analogue to the classical limit of a quantum system on which $\hbar$ is interchanged by $1/N$. Assuming this to be the case, it was pointed out by Witten that a single gauge configuration (or rather gauge orbit) would saturate the path integral, and any observable could be written in terms of this "master field" [14, 15]. In particular, given the fact that quark loops are suppressed at large N, one could use the master field to calculate the meson spectrum directly. Although the idea is quite promising, the explicit construction of the master field turned out to be only possible in simple models [21, 28], while in the more general case, the solution consists in a reformulation of the problem (constructing the master field requires the knowledge of all the connected Green's functions) [29, 30].

Yet another perspective from which factorization and the classical analogue of

large N can be obtained is discussed in [31]. The proposal in this case is to construct a coherent state basis for the large N theory which can be used to build a classical phase space and derive a classical Hamiltonian which encodes the dynamics of the original quantum model. At the formal level this can be done for U(N) gauge theories by introducing an appropriate group of unitary transformations, which applied to an initial state generate the required coherent states. Again in this case, an specific solution has not been built for the 4 dimensional Yang-Mills gauge theory.

As we have tried to show, there are several approaches to the problem of factorization, and most of them tackle the problem from different perspectives. In the last part of this section we would like to briefly discuss an additional property that emerges from Eq. (2.7) and which has received a great deal of attention in the large N lattice community. This is the property of volume reduction originally proposed in Ref. [16].

Volume reduction basically states that the infinite volume large N theory can be studied in an arbitrarily small lattice. This means that the space-time degrees of freedom are essentially encoded in the components of very large matrices. Other than the theoretical implications of such claim, the conjecture presents tremendous practical advantages, given that the effort that has to be put to simulate theories with large rank N is compensated by a reduction in the space-time volume. This has in practice allowed state of the art simulations to reach values of $N \propto \mathrm{O}(10^2)$.

In the original proposal; using the fact that the product of Wilson loops can be factorized, the loop equations for the large N lattice gauge theory in infinite volume were shown to be the same as those of a single site model with periodic boundary conditions. The corrections are suppressed by powers of $1/N$ which shows that the theories are equivalent in the large N limit, with the added caveat that center symmetry ($\mathbb{Z}$ for finite N) must not be broken. Unfortunately, it was immediately shown that the centre symmetry is spontaneously broken for theories in $d > 2$ dimensions [32, 33].

Following this, there were several proposals which tried to cure the problem and rescue volume reduction. One option, as noted in Ref. [34], is to renounce to the full volume reduction and settle for a partial volume reduction in the sense that the large N and infinite volume limit results can only be computed on lattices of a critical size $L_c(N)$, but not smaller than that. Although L_c could in practice be small; reducing considerably the amount of computer time needed for a simulation, the problem arises once the continuum limit is attempted, as L_c becomes increasingly larger and at some point the partial volume reduction looses its practical advantage.

If the reduction to a single lattice site wants to be saved, the most relevant proposals include the so called Adjoint Eguchi-Kawai model [35], which stabilizes the center symmetry by introducing fermions in the adjoint representation; and the Twisted Eguchi-Kawai model [36, 37, 38], on which the single site model has twisted instead of periodic boundary conditions. In particular, the latter proposal has shown significant progress in the recent years (see Refs. [39, 40, 41] for some examples).

3. Topological susceptibility and the $\mathrm{U}(1)_{\mathrm{A}}$ problem

As discussed previously, the large N expansion of $\mathrm{SU}(N)$ Yang-Mills theory provides an elegant solution for the $\mathrm{U}(1)_{\mathrm{A}}$ problem and provides a quantitative explanation for the large mass of the η' meson. In the following, we briefly review the history of this problem and the relevance of a large N computation of the topological susceptibility χ_{YM}.

3.1 The fate of the $\mathrm{U}(1)_{\mathrm{A}}$ symmetry

Since the introduction of the quark model by Gell-Mann and Zweig [42, 43] in the 1960's, the understanding of the global flavour symmetries of QCD has played a crucial role to explain the masses of the bound states of the theory. In the case of the theory with massless quarks, the QCD Lagrangian is invariant under a global $\mathrm{U}(N_{\mathrm{f}})$ symmetry associated to each chirality. In the real world, with massive particles, this symmetry is only approximate, but given the small masses of the u and d quarks, the effects of the symmetry can still be observed in the spectrum. Going further, considering that the typical scale for this approximation is around 1 GeV, even the s quark can be considered approximately massless.

Let us describe how chiral symmetry is manifest in the fermion sector of QCD. The left (L) and right (R) handed components of a general Dirac spinor are defined as

$$\Psi_L = \left(\frac{1-\gamma_5}{2}\right)\Psi\,, \qquad \Psi_R = \left(\frac{1+\gamma_5}{2}\right)\Psi\,, \tag{3.1}$$

where $\gamma_5 = -\gamma_1\gamma_2\gamma_3\gamma_4$. If these transformations are applied to the massless Dirac Lagrangian (chiral limit), the left and right handed components decouple

$$\bar{\Psi}\not{D}\Psi = \bar{\Psi}_L\not{D}\Psi_L + \bar{\Psi}_R\not{D}\Psi_R\,, \tag{3.2}$$

and can be rotated independently. In terms of the chiral components, the flavour symmetry can be written as $\mathrm{U}(N_{\mathrm{f}})_{\mathrm{L}} \times \mathrm{U}(N_{\mathrm{f}})_{\mathrm{R}}$, where N_{f} corresponds to the number

of massless (or approximately massless) quarks, which is either 2 or 3. For the discussion that follows it is more convenient to write the symmetry in the following way: $SU(N_f)_L \times SU(N_f)_R \times U(1)_V \times U(1)_A$.

Let us now briefly discuss the fate of each part of the symmetry. First, the $U(1)_V$ symmetry is conserved even in the massive case and it is manifested through baryon number conservation. The $SU(N_f)_L \times SU(N_f)_R$ symmetry is spontaneously broken to $SU(N_f)_V$; as observed from the existence of a non-zero fermionic condensate $\langle \bar{\Psi}\Psi \rangle \neq 0$ [1]. Notice that this symmetry is preserved in the case of degenerate quark masses, so in the case of $N_f = 2$, given the similar mass of u and d quarks, the symmetry is only mildly broken[2].

For spontaneously broken continuous symmetries, the Goldstone theorem tells us that the breaking comes accompanied with the appearance of massless Goldstone bosons. For our model of QCD with $N_f = 3$ massless quark flavours, one expects the presence of 8 Goldstone bosons from the breaking of $SU(N_f)_L \times SU(N_f)_R$ and 1 from the breaking of the $U(1)_A$ symmetry. In real world QCD, with 3 light but not massless quarks, one expects to find light mesons corresponding to the would be Goldstone bosons. One can readily identify some of these particles, the 3 π mesons, the 4 K mesons and the η meson. There is still one particle missing in this picture, and as pointed out by Weinberg in Ref. [46], if the non-zero mass of the would be Goldstone boson associated to the breaking of the $U(1)_A$ symmetry had the same origin as the one of the rest of previously mentioned mesons, the mass of the ninth pseudo Goldstone boson should be bounded by the condition $m_{GB} < \sqrt{3} m_\pi$. However, the lightest pseudoscalar meson compatible with the $U(1)_A$ symmetry is the η' meson, whose mass is about 958 MeV, and is therefore too heavy to be the particle predicted by Weinberg.

3.1.1 The chiral anomaly

The case of the $U(1)_A$ symmetry is special, as it is in fact explicitly broken. The breaking is not observed in the classical Lagrangian, but it is only a consequence of quantum corrections. This explicit breaking is known as the chiral anomaly, and in simple terms, it arises because the fermionic part of the integral measure which enters in the path integral is not invariant under a chiral transformation [47].

The chiral anomaly can be computed perturbatively, as was shown originally in the case of QED by Adler, Bell and Jackiw [48, 49] after considering the diagram coupling the axial current

$$J_{\mu 5} = \bar{\Psi} \gamma_\mu \gamma_5 \Psi \,, \tag{3.3}$$

[1] Note that this is a non-perturbative effect and as such has been an important subject of study of lattice QCD [44, 45]

[2] This is precisely the SU(2) isospin symmetry observed in the nucleons.

to two photons with an intermediate triangle shaped quark loop. For a non-Abelian gauge theory, the anomaly can be computed in a similar way and at one loop the result is

$$\partial_\mu J_{\mu\,5}(x) = -\frac{1}{16\pi^2}\ \mathrm{Tr}\, F_{\mu\nu}\ {}^*F_{\mu\nu} = 2\, q(x)\,, \tag{3.4}$$

where ${}^*F_{\mu\nu} = \epsilon_{\mu\nu\rho\sigma}F_{\rho\sigma}$, and $q(x)$ is the topological charge density. The Adler-Bardeen theorem [50] then guarantees that the anomaly does not get any corrections at higher loop orders. Note that for convenience, the result in Eq. (3.4) has been written in terms of the rescaled fields $gA_\mu \to A_\mu$ and we will keep this convention throughout this chapter unless stated otherwise.

As shown by 't Hooft [51, 52], the anomaly gets contributions from non equivalent vacuum configurations with different winding number. Moreover, the different configurations (topological sectors) are connected by non-perturbative objects known as instantons; which are finite action solutions to the classical equations of motion in Euclidean space time. Their non-perturbative nature is made evident as instantons have a classical action[3]

$$S_{\rm instanton} = \frac{8\pi^2}{g^2}\,. \tag{3.5}$$

.

In fact, the integrated topological charge Q

$$Q = \int d^4x\, q(x) = \int d^4x\, \partial_\mu K_\mu\,, \tag{3.6}$$

can be written in terms of the local Chern-Simons current K_μ [53], and using Gauss' law it can be cast into a surface integral over the boundary Σ of $\mathbb{R}^4$, which is isomorphic to the three sphere S^3, so that

$$Q = \int d\Sigma \hat{n}_\mu K_\mu\,, \tag{3.7}$$

where $\hat{n}_\mu$ is a normal vector to Σ. This expression shows that Q is a topological quantity that depends on the configuration of the gauge fields in the boundary of the space-time, where the gauge field $A_\mu(x)$ approaches a pure gauge field. The expression in Eq. (3.7) is the winding number of the gauge manifold and in the case of SU(N) it is given by the third homotopy group of S^3, $\pi_3(S^3) = \mathbb{Z}$. In this sense, the vacuum configurations can be classified according to their integer winding number Q.

[3]Note that the transition probability between two instanton vacua is give by $e^{-S_{\rm instanton}}$ and its small g expansion is zero at all orders.

Going back to the computation of the anomaly, a very instructive way to understand its origin is to look at the transformation properties of the measure under a chiral transformation. In the following, we review the discussion presented in Refs. [47, 54]. Let us look at the chiral transformation of the fermion fields

$$\Psi(x) \to e^{i\alpha(x)\gamma_5}\Psi(x)\,, \qquad \bar{\Psi}(x) \to \bar{\Psi}(x)e^{i\alpha(x)\gamma_5}\,. \tag{3.8}$$

Then, under an infinitesimal transformation, and neglecting the change in the integration measure, the fermionic part of the functional integral changes to

$$\mathcal{Z} \to \int d\Psi d\bar{\Psi}\, \exp\left\{-\int d^4x\, \left(\bar{\Psi}(\not{D})\Psi - i\alpha(x)\partial_\mu J_{\mu\,5}\right)\right\}. \tag{3.9}$$

If the Jacobian of the transformation in Eq. (3.8) was equal to 1, Eq. (3.9) would imply the conservation of the axial current as in the classical theory. Therefore, the anomaly must appear from the change in the integration measure $d\bar{\Psi}d\Psi$, which can be evaluated from the Jacobian of the chiral transformation. To do that, one can use a basis $\{\phi_n\}$ of eigenvectors of the hermitian operator $\not{D} = \gamma_\mu D_\mu$ and show that [47]

$$d\bar{\Psi}d\Psi \to \mathcal{J}^{-2}d\bar{\Psi}d\Psi\,, \tag{3.10}$$

with

$$\mathcal{J} = \exp\left\{i\int d^4x\,\alpha(x)\sum_n \phi_n(x)^\dagger\gamma_5\phi_n(x)\right\}. \tag{3.11}$$

The sum in Eq. (3.11) has to be regularized as discussed in Ref. [47], and in more detail in Ref. [54]. We do not go into the details and simply quote the final result of the calculation

$$\mathcal{J} = \exp\left\{-i\int d^4x\,\alpha(x)\left[\frac{1}{16\pi^2}\,\mathrm{Tr}\,F_{\mu\nu}\,{}^*F_{\mu\nu}\right]\right\}. \tag{3.12}$$

Finally, combining Eqs. (3.12), (3.10) and (3.9), and taking the variation with respect to $\alpha(x)$ allows us to obtain the chiral anomaly from Eq. (3.4).

A remarkable property connected to the results presented above is that of the Atiyah-Singer index theorem [55]. Naively, using the fact that $\left\{\gamma_5, \not{D}\right\} = 0$, one can argue that in passing from (3.11) to Eq. (3.12), the only non-zero contribution comes from the zero-modes of $\not{D}$. The famous result then connects the number of zero modes with right (n_L) and left (n_R) chirality to the integral of the topological charge density, i.e., the integrated topological charge Q

$$n_L - n_R = -\frac{1}{32\pi^2}\int d^4x\;\mathrm{Tr}\,F_{\mu\nu}\,{}^*F_{\mu\nu} = Q\,. \tag{3.13}$$

3.2 The Witten-Veneziano solution

The presence of the chiral anomaly shows that indeed the $\mathrm{U(1)_A}$ symmetry is explicitly violated, thus it is not expected for the η' meson to be massless even in the chiral limit. This statement however is not completely satisfactory as it does not explain the way in which the mass emerges as a consequence of the anomaly. Ideally, we would like to be able to turn off the anomaly and treat the η' as another Goldstone mode, then, by turning the anomaly back on, it should be possible to show how the η' meson acquires its mass.

It was not until 1979, when Witten [56] and Veneziano [57] proposed a mechanism which allows precisely to do that. The basis of their analysis was to consider the large N limit of QCD where the anomaly is in fact not present[4]. To see that, simply rescale the gauge fields $A_\mu \to gA_\mu$ in Eq. (3.4) to show that the anomaly is proportional to λ/N, so it vanishes in the 't Hooft limit and the η' meson becomes the ninth Goldstone boson in the chiral limit.

In the original paper from Witten, he motivated the necessity of a messon whose mass squared is proportional to $1/N$. The existence of this meson solved an apparent paradox in the large N limit, which arises from the fact that the topological susceptibility in the pure gauge theory χ_{YM} has a finite O(1) value, while from chiral perturbation theory, $\chi = 0$ [59, 60] in the full theory with massless quarks. From simple large N counting arguments, this would not be possible as quark loop effects are suppressed by a power of $1/N$ in the planar limit, so they could not cancel the O(1) value from the pure gauge theory. In Ref. [56], arguments are presented which explain how setting $m^2_{\eta'} \propto 1/N$ solves this paradox. In Ref. [57], the author reaches the same conclusion through the study of the expansion of QCD on the small parameter $u = N_{\mathrm{f}}/N$ and looking at the chiral Ward identities. Both results in the end relate the mass of the η' meson to χ_{YM}, which is by itself an interesting statement as both quantities are defined in different theories, and possibly make allusion to the observation that in the large N limit, QCD becomes effectively quenched.

In the following we briefly *sketch some of the main arguments* leading to the derivation of the Witten-Veneziano relation as presented in Refs. [61, 62]. Let us start from the two point function $\langle q(x)q(0)\rangle$ of the topological charge density defined in Eq. (3.4). After fixing the necessary counterterms to make its Fourier transform finite [62], consider

$$\chi(p) = \int d^4x e^{ipx} \langle q(x)q(0)\rangle + CT(p)\,, \tag{3.14}$$

where $CT(p)$ is a polynomial in p of degree 4 which vanishes at $p = 0$ [61, 62]. Using the Källén-Lehmann representation, $\chi(p)$ is given in terms of a three times

[4]Notice that one could already suspect the large N limit to be a good way to proceed from the fact that in such limit one has effectively a nonet of pseudoscalar mesons [58].

subtracted dispersion relation as

$$\chi(p) = a_1 + a_2 p^2 + a_3 (p^2)^2 + \left(p^2\right)^3 \int_{m^2}^{\infty} \frac{\rho(t)}{t^3\left(t + p^2\right)}\,, \tag{3.15}$$

where the integral goes from m^2 as one does not expect the presence of a massless pseudoscalar with the quantum number of $q(x)$.

Following Witten and Veneziano, the main assumption to be made is that the dominant contribution to the dispersion relation in Eq. (3.15) comes from the η' meson, so that it can be extracted, before any subtraction, to give

$$\chi(p) = b_1 + b_2 p^2 + b_3 (p^2)^2 - \frac{R^2_{\eta'}}{p^2 + m^2_{\eta'}} + \left(p^2\right)^3 \int_{m^2}^{\infty} \frac{\sigma(t)}{t^3\left(t + p^2\right)}\,, \tag{3.16}$$

where $-R^2_{\eta'}$ is the residue from the η' pole. Now take the $p \to 0$ limit of Eq. (3.16) in the chiral limit. As mentioned earlier, in the chiral limit, the left hand side vanishes, which implies that

$$b_1 = \frac{R^2_{\eta'}}{m^2_{\eta'}}\,. \tag{3.17}$$

The coefficient b_1 can be given an explicit physical meaning by taking the $N_{\rm f}/N \to 0$ limit of Eq. (3.16) at fixed p^2 and later taking the limit $p \to 0$. As already mentioned, in the $N_{\rm f}/N \to 0$ limit, quark loop effects are suppressed, so taking this limit corresponds to quenching on the left hand side. On the right hand side, $R^2_{\eta'}$ is $\mathrm{O}(1/N)$ due to the large N counting rules[5], so that after setting $p = 0$, one has that $b_1 = \chi_{\rm YM}$. Inserting this into Eq. (3.17) results in the formula

$$\chi_{\rm YM} = \frac{R^2_{\eta'}}{m^2_{\eta'}} + \mathrm{O}(N_{\rm f}/N)\,, \tag{3.18}$$

which relates the topological susceptibility in the pure gauge theory to the mass of the η' meson. Notice that b_1 is $\mathrm{O}(1)$, which implies that $m^2_{\eta'}$ is $\mathrm{O}(1/N)$ [63]. All is left is to evaluate $R^2_{\eta'}$, which can be done by using the anomaly Eq. (3.4)

$$R^2_{\eta'} = \frac{|\,\langle 0|\,\partial_\mu J^{\mu\,5}\,|\eta'\rangle\,|^2}{4N_{\rm f}^2}\,, \tag{3.19}$$

[5]Notice that using the chiral anomaly equation, $R^2_{\eta'}$ is proportional to the squared matrix element of the divergence of the chiral axial current, which gives a factor of λ/N^2, while the diagram itself is of $\mathrm{O}(N)$.

and the fact that $\langle 0|\, \partial_\mu J^{\mu\,5}\, |\eta'\rangle = p^\mu \langle 0|\, J^{\mu\,5}\, |\eta'\rangle = m_{\eta'}^2 \sqrt{2N_{\rm f}} f_{\eta'}$, where the $\sqrt{N_{\rm f}}$ factor is chosen as to have an $N_{\rm f}$ independent definition of $f_{\eta'}$ [61]. The famous Witten-Veneziano relation can be written after replacing $f_{\eta'}$ by f_π [58, 64] to the leading order in the $1/N$ expansion

$$\chi_{\rm YM} = \frac{m_{\eta'}^2 f_\pi^2}{2N_{\rm f}} + {\rm O}(N_{\rm f}/N) + {\rm O}(m_q)\,, \tag{3.20}$$

where m_q is the quark mass.

Going beyond in the chiral expansion, one can compute the higher order corrections to Eq. (3.20) by performing a power counting scheme in momenta p, quark masses m_q and $1/N$ [64, 65], which leads to

$$\lim_{N\to\infty} \chi_{\rm YM} = \lim_{N\to\infty} \frac{f_0^2}{2N_{\rm f}} \left(m_{\eta'}^2 + m_\eta^2 - 2m_K^2 \right) + {\rm O}(m_q^2) \tag{3.21}$$

where we have written the relation in more general terms by not identifying the singlet decay constant with f_π as in Eq. (3.20).

In principle, one would like to test the different assumptions made to obtain the Witten-Veneziano relation. In this sense, one of the ingredients is the computation of the topological susceptibility $\chi_{\rm YM}$ in the large N limit of the pure gauge theory. Due to its non-perturbative nature, it cannot be computed through perturbative methods and has to be assessed with a non-perturbative approach as the one from lattice QCD, which is presented in the next chapter.

4. SU(N) on the lattice

In this chapter, we introduce the basic concepts needed to understand the lattice formulation of SU(N) gauge theories on the lattice. We also discuss the ideas which are useful for our particular study, such as open boundary conditions and the Yang-Mills gradient flow.

4.1 The lattice formulation

As mentioned in Sec. 1, many interesting phenomena are governed by the properties of the strong interaction and occur at energy scales where the expansion parameter α is large, which makes it impossible to use perturbation theory. In this non-perturbative regime, lattice QCD is perhaps the only practical way to perform calculations.

The original idea was first described by Wilson in Ref. [1]. One can summarize the main concepts of the lattice formulation as: 1) the continuation of the path integral formulation to Euclidean space-time via a Wick rotation of the time coordinate, 2) the discretization of the space time to a lattice with a countable set of points, and 3) the preservation of exact gauge invariance. The lattice spacing is conventionally denoted by a, while the lattice extent is denoted by $L^3 \times T$. Notice that for convenience one of the directions has been labelled as T, although in the Euclidean metric, all the directions are on equal grounds. Traditionally, periodic boundary conditions are used in all four directions, but several different proposals can be more advantageous on different circumstances. In particular, in Sec. 4.4 we present one particular choice which is to use open boundary conditions in the time direction.

Working with this setup, every point in the lattice can be denoted by a set of four integers (n_0, n_1, n_2, n_3), such that any point on the lattice can be expressed simply as a product of these numbers times the lattice spacing a. One of the main advantages of the lattice formulation is that it provides a mathematically well defined definition of the path integral, which is now an integral over a countable set of variables, and if the lattice size is finite (i.e. L and T are finite), the integral is performed over a countable and finite set of variables. This property, in particular, makes it possible

to put the system in a computer. The basic idea is then to compute observables at a finite lattice spacing and then take the limit $a \to 0$ in order to recover the physics of the continuum theory.

In addition to making the path integral well defined, the discreteness of space-time imposes a natural momentum cut-off π/a, such that a acts as a regulator for the theory. Notice however, that this is different to the standard momentum cut-off in the continuum, as the lattice regulator preserves gauge invariance. Moreover, the perturbative structure of the lattice formulation is different to the one of the dimensional regularized continuum theory, as new Feynman diagrams come out, which are related to the lattice regularization and are not present in dimensional regularization. One can argue that although the lattice formulation provides a way to impose a gauge invariant regulator for the theory, it breaks some of the basic symmetries of the continuum model, such as translation invariance or rotational symmetry, but they are recovered once the continuum limit is taken. The main advantage of the lattice formulation is that it allows to study the theory without making an explicit reference to perturbation theory, thus it is ideal to explore non-perturbative effects which are otherwise not accessible.

Unlike the continuum version, the basic quantity in the lattice is the parallel transporter between two adjacent sites, which is denoted by

$$U_\mu(x) = e^{aA_\mu(x)} \quad \in \mathrm{SU}(N)\,, \tag{4.1}$$

and is commonly referred to as the gauge link. Similarly, one can define $U^\dagger_\mu(x) = U(x + a\mu)_{-\mu}$ as the link with the opposite orientation. When referring to the set of all gauge links on the lattice, the term gauge configuration is commonly used, and we will use it throughout this text.

In this thesis we are interested only in the pure gauge theory, so we limit our discussion to that case and do not discuss fermions on the lattice here. In the pure gauge theory, the basic gauge invariant operators are built out of traces of products of closed paths of gauge links, known as Wilson loops. The simplest of them is the plaquette $U_{\mu\nu}(x)$, defined as

$$U_{\mu\nu}(x) = U_\mu(x)U_\nu(x + a\mu)U^\dagger_\mu(x + a\nu)U^\dagger_\nu(x)\,. \tag{4.2}$$

Using the plaqutte, the lattice gauge action is given by

$$\tilde{S}_G\,[U] = \frac{1}{g^2}\sum_{x,\mu,\nu} \mathrm{Tr}\left\{1 - U_{\mu\nu}(x)\right\}\,, \tag{4.3}$$

where the sum is performed over oriented plaquettes. Notice that the Lie algebra valued field $A_\mu(x)$ in Eq. (4.1) is strictly defined for the countable set of points on the lattice. If instead, we assume that it can be written as a classical smooth field

and expand $\tilde{S}_G$ in powers of the lattice spacing a, the classical continuum limit of the lattice gauge action agrees with its well known continuum counterpart[1]

$$S_G = -\frac{1}{2g^2}\int d^4x \,\mathrm{Tr}\, F_{\mu\nu}F_{\mu\nu}\,. \tag{4.4}$$

It is also convenient to define the inverse lattice coupling

$$\beta = \frac{2N}{g^2}\,. \tag{4.5}$$

Once the action has been defined, the expectation value of observables is given by the path integral

$$\langle\mathcal{O}\rangle = \frac{1}{\mathcal{Z}}\int d[U]\mathcal{O}\, e^{-S_G[U]}\,, \quad \mathcal{Z} = \int d[U]e^{-S_G[U]}\,, \tag{4.6}$$

where $d[U] = \Pi_{x,\mu}dU_\mu(x)$ is defined in terms of the SU(N) invariant Haar measure $dU_\mu(x)$. $\mathcal{Z}$ is called the partition function in analogy to the one in statistical physics. Notice that because we are working on Euclidean space-time; the exponential factor is real and so it resembles the Boltzmann factor in a statistical ensemble average. The resemblance suggests that one can borrow the widely developed techniques from statistical physics to compute expectation values on the lattice. In particular, one can use importance sampling and Monte-Carlo techniques to efficiently compute $\langle\mathcal{O}\rangle$ in Eq. 4.6.

4.2 Simulation algorithms

The way in which Eq. 4.6 is made manifest in the day to day calculations of lattice QCD practitioners, is through Monte-Carlo simulations. In simple terms, a sequence of gauge configurations $U^{(i)}$ is generated, such that

$$\langle\mathcal{O}\rangle = \lim_{n\to\infty}\frac{1}{n}\sum_{i=1}^{n}\mathcal{O}(U^{(i)}) \equiv \bar{\mathcal{O}}\,. \tag{4.7}$$

The sequence is taken from a Markov chain generated by a stochastic process, with a given transition probability $W(U \to U')$. The transition probability must be constructed so that it satisfies the following properties

1. Stability: $\sum_U e^{-S_G[U]}W(U\to U') = e^{-S_G[U']}$
2. Ergodicity: $\forall\, U, U'\,, \exists\, n < \infty\,, \text{s.t.}\, W^n(U\to U') > 0\,.$

[1]Note that from now on, we will use this convention in contrast to the one in used in Eq. (2.1).

Clearly, when performing a simulation, one is limited by a finite amount of resources, and the summation in Eq. 4.7 has to be truncated for a large but finite value of n. In this sense, a more illuminating way to express the idea behind importance sampling is to write

$$\hat{\mathcal{O}} = \frac{1}{n}\sum_{i=1}^{n} \mathcal{O}(U^{(i)}) = \bar{\mathcal{O}} + \mathrm{O}\left(\frac{1}{\sqrt{n}}\right) , \tag{4.8}$$

which states that one can define an estimator $\hat{\mathcal{O}}$ for $\bar{\mathcal{O}}$, whose error decreases as the number of measurements n grows. We will make this statement more precise in the following.

4.2.1 Autocorrelation times

In principle, the chain of configurations generated through the Monte-Carlo process are not all independent. This is evident from the fact that $U^{(i)}$ is generated from $U^{(i-1)}$ through $W(U^{(i-1)} \to U^{(i)})$. Moreover, Eq. (4.8) is valid when the set of configurations $U^{(i)}$ is distributed according to the stationary probability density $P(U) = e^{-S_G[U]}/\mathcal{Z}$. Let us discuss this issue first.

Assume the Markov chain starts from a given configuration $U^{(1)}$, then, the probability distribution of the k-th configuration is given by $P_k(U) = W^{k-1}U^{(1)}$. It can be shown that $P_k(U)$ approaches the stationary $P(U)$ as

$$P(U) = \lim_{k\to\infty} \left(P_k(U) + \mathrm{O}(e^{-k/\tau_{\mathrm{exp}}}) \right) , \tag{4.9}$$

where τ_{exp} is the exponential autocorrelation time. Eq. 4.9 tells us that a given configuration $U^{(i)}$ obeys the right stationary probability density if $i \gg \tau_{\mathrm{exp}}$. Thus, in a simulation, it is customary to start measuring only after the previous condition has been fulfilled. The time before an actual measurement is performed is known as thermalization time and it has to be taken into consideration when planning any Monte-Carlo simulation.

Concerning the degree of independence of each configuration in the Markov chain, it is convenient to define the autocorrelation function $\Gamma(k)$ as

$$\Gamma_{\mathcal{O}}(k) = \left\langle \mathcal{O}(U^{(i)})\mathcal{O}(U^{(i+k)}) \right\rangle - \left\langle \mathcal{O}(U^{(i)}) \right\rangle \left\langle \mathcal{O}(U^{(i+k)}) \right\rangle , \tag{4.10}$$

which for $i \gg \tau_{\mathrm{exp}}$ is independent of i. The average $\langle\cdot\rangle$ is taken over an ensemble of chains with independent random numbers and initial states. The autocorrelation function basically estimates the correlation between any two measurements separated by a distance k in the Markov chain. Using the autocorrelation function one can give an explicit formula for the error $\sigma_{\mathcal{O}}$ in the estimator $\hat{\mathcal{O}}$

$$\sigma^2_{\mathcal{O}} = \left\langle (\hat{\mathcal{O}} - \bar{\mathcal{O}})^2 \right\rangle = \frac{2\tau_{\rm int}(\mathcal{O})}{n}\Gamma_{\mathcal{O}}(0) + \mathrm{O}(n^{-2})\,, \tag{4.11}$$

where $\tau_{\rm int}$ is the integrated autocorrelation time defined as

$$\tau_{\rm int}(\mathcal{O}) = \frac{1}{2\Gamma_{\mathcal{O}}(0)} \sum_{k=-\infty}^{k=\infty} \Gamma_{\mathcal{O}}(k)\,. \tag{4.12}$$

This quantity encodes the autocorrelation in the Markov chain, and its effect in Eq. (4.11) is to reduce the number of independent measurements from n to $n/2\tau_{\rm int}$. Notice that for independent configurations $\tau_{\rm int} \to 1/2$. Unlike $\tau_{\rm exp}$, which depends only on the update algorithm, $\tau_{\rm int}$ depends also on the particular observable which is being considered, but it is never larger than $\tau_{\rm exp}$. The formulas in Eqs. (4.11) and (4.12) can be generalized to more complicated functions of several observables $f(\{\mathcal{O}_\alpha\})$, and for the details, the reader is invited to look at a more complete derivation of the error formula as the one in Ref. [66]. Basically, for the estimator F of the function f one has

$$\sigma^2_F = \frac{2\tau_{\rm int,F}}{n} v_F\,, \tag{4.13}$$

where

$$\tau_{\rm int,F} = \frac{1}{2v_F} \sum_{k=-\infty}^{\infty} \sum_{\alpha\beta} \frac{\partial f}{\partial \mathcal{O}_\alpha} \frac{\partial f}{\partial \mathcal{O}_\beta} \Gamma_{\alpha\beta}(k)\,, \quad v_F = \sum_{\alpha\beta} \frac{\partial f}{\partial \mathcal{O}_\alpha} \frac{\partial f}{\partial \mathcal{O}_\beta} \Gamma(0)\,, \tag{4.14}$$

is given in terms of the correlation function

$$\Gamma_{\alpha\beta}(k) = \left\langle \left(\mathcal{O}^{(i)}_\alpha - \bar{\mathcal{O}}_\alpha\right) \left(\mathcal{O}^{(i+k)}_\beta - \bar{\mathcal{O}}_\beta\right) \right\rangle\,, \tag{4.15}$$

and the derivatives of the function f evaluated at the true value of the observable $\mathcal{O}_\alpha$. In practice, the autocorrelation function cannot be summed up to arbitrarily large values of k, and the derivatives are computed numerically. Throughout this work, we compute the errors using the method described in Ref. [66].

In the following, we briefly describe some of the most frequently used algorithms to generate the transition probability $W(U \to U')$.

4.2.2 The hybrid overrelaxation algorithm

In the case of the pure gauge theory, most algorithms make use of the locality of the action in Eq. (4.3). A full update of the gauge configuration is then a composition of elementary link updates visited in a particular order. One of the most efficient algorithms is a combination of heatbath and overrelaxation updates, which takes the name of hybrid overrelaxation.

Heatbath algorithm

In the heatbath algorithm [67], each gauge link $U_\mu(x)$ is replaced by $U'_\mu(x)$ chosen at random from the entire group with a probability density given by

$$p(U'_\mu(x))dU'_\mu(x) = dU'_\mu(x)e^{-S_G(U'_\mu(x))} \propto dU'_\mu(x)\exp\left\{\frac{\beta}{N}\mathrm{Re}\,\mathrm{Tr}\left[U'_\mu(x)\Sigma_\mu(x)\right]\right\}, \tag{4.16}$$

where $S_G(U'_\mu(x))$ is the gauge action depending only on the link $U'_\mu(x)$, while the rest remain fixed. The staple $\Sigma_\mu(x)$ is made from the sum of products of gauge links adjacent to $U'_\mu(x)$. A full lattice update consists in a sweep over all gauge links updated one at a time. Although the idea is formally simple, the actual implementation is very challenging for $N > 2$. Considering this, when performing a heatbath update in SU(N), one generally uses a method known as the Cabibbo-Marinari method [68], which updates SU(2) subgroups of SU(N) sequentially.

In the case of SU(2) there are very efficient ways to draw the gauge link $U'_\mu(x)$ with the right probability distribution [69, 70]. Basically, the probability distribution in Eq. (4.16) can be rewritten as

$$p(U')dU' \propto dU'\exp\left\{\frac{\beta}{2}\zeta\,\mathrm{Tr}\,U'\omega\right\}, \tag{4.17}$$

where $\zeta = \sqrt{\det\Sigma}$ and $\omega = \Sigma/\zeta$, and we have omitted the x and μ dependence of the variables for simplicity[2]. Considering that $A = U'\omega \in \mathrm{SU}(2)$ can be expressed as $A = a_0\mathbf{1} + i\mathbf{a}\cdot\sigma$, where σ are the Pauli matrices and $a = (a_0, \mathbf{a})$ is a set of 4 real numbers, the problem reduces to generating a_0 with probability density

$$p(a_0)da_0 = \left(1 - a_0^2\right)^{1/2} e^{\alpha a_0}da_0\,, \tag{4.18}$$

and a_i uniformly distributed on a two-sphere of radius $(1 - a_0^2)^{1/2}$. The parameter $\alpha = \frac{\beta}{2}\zeta$ encodes the dependence on the inverse lattice coupling β and the staple Σ. Once A has been generated, the gauge link U' can be reconstructed by right multiplication with $w^\dagger$.

As mentioned previously, the case of SU(N) relies on the SU(2) updates through the Cabibbo-Marinari method. Briefly, one defines a subset F of SU(N) such that $A^{(i,j)} \in F$ is labelled by the two indices $i \neq j\,, (i,j) \in [1,N]^2$, and

$$A^{(i,j)}_{kl} = \begin{cases} \delta_{kl} & \text{for} \quad k,l \neq i,j \\ a_{kl} & \text{otherwise}\,, \end{cases} \tag{4.19}$$

[2]Notice that ω defined in this way is in SU(2), and also that $\det\Sigma > 0$.

where the submatrix $a_{kl} \in \mathrm{SU}(2)$. In addition, we require that no subset of $\mathrm{SU}(N)$, except $\mathrm{SU}(N)$ itself, is invariant under left multiplication by F. The minimal subset F which satisfies this property has $N-1$ elements, however, it is more efficient to choose F with $N(N-1)/2$ elements given by $F = \left\{A^{(i,j)}\right\}_{i<j}$ [71]. Then, the update proceeds by choosing $A \in F$ with probability density proportional to $\exp\left(\mathrm{Re}\,\mathrm{Tr}\, AU_\mu(x)\Sigma_\mu(x)\right)$. Due to the way in which A has been defined in Eq. (4.19), one can show that the problem reduces to generating the submatrix $a_{kl} \in \mathrm{SU}(2)$, so one can use the efficient algorithms for the SU(2) gauge theory. The new link is then given by $U'_\mu(x) = AU_\mu(x)$, and the process is repeated for all $A \in F$.

Overrelaxation algorithm

Unlike the heatbath update, an overrelaxation update does not perform a random walk, and is known to explore the space of field configurations faster [72, 71]. The idea is the following: for each link, suppose there is a way to find the element $U^0_\mu(x)$ which minimizes the local action $S_G(U_\mu(x))$, then, the overrelaxation update consists in choosing the new element as the link which is in the opposite direction of the original $U_\mu(x)$ with respect to the minimum [73, 74]

$$U'_\mu(x) = U^0_\mu(x) U_\mu(x)^\dagger U^0_\mu(x)\,. \tag{4.20}$$

For SU(2), this is achieved by picking $U^0_\mu(x) = \sqrt{\det\left[\Sigma_\mu(x)\right]}\,\Sigma^{-1}_\mu(x)$, which allows to write Eq. (4.20) in a more convenient way as

$$U'_\mu(x) = \frac{2\,\Sigma^\dagger_\mu(x) U_\mu(x)^\dagger \Sigma^\dagger_\mu(x)}{\mathrm{Tr}\left(\Sigma_\mu(x)\Sigma^\dagger_\mu(x)\right)}\,. \tag{4.21}$$

This algorithm can easily be shown to be microcanonical, so it is common to perform several overrelaxation updates followed by one heatbath update to guarantee ergodicity.

As with the heatbath update, it is convenient to use a Cabibbo-Marinari strategy to update $\mathrm{SU}(N)$ matrices. We must also point out that a full $\mathrm{SU}(N)$ overrelaxation update without considering the SU(2) subgroups can be done [75], and promising results have been seen also for reduced models [71].

4.2.3 Critical slowing down

Lattice simulations are naturally limited by the computational resources available, and the situation only gets worse when approaching the continuum limit. At a fixed physical volume, the increase in the number of points in the lattice is proportional to a^{-4}, but this is not the only difficulty when approaching the continuum. The algorithms that we have presented before suffer from a problem known as "critical

slowing down". Basically, it means that simulations become ever more costly as a critical point is approached, as is the case of the continuum limit of lattice gauge theories.

In particular, topological observables such as the topological charge Q have been observed to suffer from a very severe case of slowing down, as their autocorrelation times scale as a^{-z}, with $z \approx 5$ as reported in Ref. [76]. Notice however that it is not clear what happens at even smaller lattice spacings those considered in Ref. [76], where the situation is only expected to get worse. Furthermore, for the relevant case of SU(N) gauge theories, with $N > 3$, the problem is more severe, and as reported in Ref. [77], the scaling is consistent with an exponential growth in the rank of the gauge group N. The rapid increase in autocorrelations poses a big obstacle to approach lattice spacings much smaller than $a \approx 0.05\,\text{fm}$ in the case of full QCD, and up to $a \approx 0.08\,\text{fm}$ in the case of pure SU(N) Yang-mills gauge theories.

Qualitatively, the severe case of critical slowing down may be due to the appearance of large action barriers that separate the different topological sectors, which increase dramatically as one approaches the continuum. Indeed, in the classical continuum Yang-Mills theory, the different topological sectors are separated by barriers of infinite action. Numerically, the suppression of field configurations which are in between the sectors has been observed for both pure Yang-Mills theory, as well as for the theory including fermions [78, 79].

One way to alleviate the problem of the growth of autocorrelations is to use open boundary conditions [80], but before we describe them, let us first introduce the Yang-Mills gradient flow.

4.3 The Yang-Mills gradient flow

A very interesting recent development in gauge theories has been the introduction of the so called Yang-Mills gradient flow, or the Wilson flow as commonly referred to in the lattice community. The idea did not originate on the lattice, but it was brought up to this context by the authors in Refs. [78, 81]. The flow is based on the idea of introducing an additional dimension represented by a parameter t (the flow time) in which the gauge fields evolve according to the equation

$$\frac{dB_\mu(x,t)}{dt} = D_\nu G_{\nu\mu}(x,t)\,, \tag{4.22}$$

subject to the boundary conditions $B_\mu(x, t = 0) = A_\mu(x)$, where $A_\mu(x)$ is the gauge field in the original four dimensional theory using the normalization from Eq. (4.4). $G_{\mu\nu}$ is the field strength tensor defined using the flowed fields $B_\mu(x,t)$. The flow equation brings the action in the direction of the steepest descent, so it effectively acts as a way to smooth the gauge fields by removing ultraviolet fluctuations.

A convenient way to see this, is to rescale the gauge fields $A_\mu(x) \to gA_\mu(x)$ and expand $B_\mu(x,t)$ in powers of the bare coupling. In perturbation theory, it is convenient to introduce the gauge parameter λ such that Eq. (4.22) is modified by the term $\lambda D_\mu \partial_\nu B_\nu$ [78]. Then, replacing the expansion of $B_\mu(x,t)$

$$B_\mu(x,t) = \sum_{k=1}^{\infty} g^k B_{\mu,k}(x,t)\,, \qquad B_{\mu,k}(x,t=0) = \delta_{1k} A_\mu(x)\,, \tag{4.23}$$

in the modified equation, and choosing $\lambda = 1$, one obtains a set of equations organized in powers of g. To first order one gets

$$B_{\mu,1}(x,t) = \int d^D y K_t(x-y) A_\mu(y)\,, \qquad K_t(z) = \frac{e^{-z^2/4t}}{(4\pi t)^{D/2}} \tag{4.24}$$

where D is the dimensionality of the space-time. Eq. (4.24) explicitly shows that the effect of the flow is that of averaging over a spherical region in space-time with a mean square radius of $\sqrt{8t}$ in four space-time dimensions [78].

A remarkable property of the flow is the fact that correlators of fields constructed at positive flow time are automatically finite at all orders in perturbation theory [82]. In this sense, the flow provides a way to define renormalized quantities, which is particularly useful in the lattice where it has been extensively used in the recent years (see for example the recent reviews [83, 84]).

Along these lines, the Yang-Mills energy density[3]

$$\left\langle e^t(x) \right\rangle = -\frac{1}{2} \left\langle \mathrm{Tr}\, G^t_{\mu\nu}(x) G^t_{\mu\nu}(x) \right\rangle \tag{4.25}$$

has received much attention, as it can be used to define a renormalized coupling depending on the scale given by the flow radius $\sqrt{8t}$, and it can therefore be used to fix the scale in a lattice simulation. In the lattice, the discretized Yang-Mills gradient flow equation is

$$a^2 \dot{V}^t_\mu(x) = -g^2 \left\{ \partial_{x,\mu} S(V) \right\} V^t_\mu(x), \qquad V^{t=0}_\mu(x) = U_\mu(x)\,, \tag{4.26}$$

where we denote by V^t the gauge links at positive flow time. In the simplest case, the action on the right hand side is chosen to be the Wilson action.

[3] Notice that from now on when discussing observables at positive flow time, we use a notation where the time dependence is written as a superscript; hence, $e^t(x) \equiv e(x,t)$.

4.3.1 The scale t_0 for SU(N) Yang-Mills gauge theory

As we have mentioned previously, the lattice provides a framework to regularize a field theory by means of the cut-off imposed by the inverse lattice spacing $1/a$. The continuum limit $a \to 0$ corresponds then to the renormalization program, where one removes the cut-off while keeping some physical quantity fixed.

Quantities computed in the lattice are expressed in units of the cut-off, i.e. in units of the lattice spacing a. Looking for example at a mass $\tilde{m} = ma$; where m is a physical dimensionful quantity, the continuum limit $a \to 0$ is taken such that m is kept fixed. This means that $\xi = 1/\tilde{m}$ is a correlation length which diverges as we approach the continuum. In this sense, the continuum limit corresponds to a critical point of the lattice theory.

In the case of the pure Yang-Mills lattice theory at fixed N, the only free parameter is the bare coupling g^2, or equivalently the 't Hooft coupling λ. This parameter has to be tuned to approach the critical point in a well defined manner[4]. Similarly as in the continuum theory, one can define the lattice β function as

$$\beta_{\text{Lat}}(g) = -a\frac{\partial g}{\partial a}\,. \tag{4.27}$$

Taking the results from Refs. [85, 86] one can use the three loop expression of β_{Lat} and integrate Eq. (4.27) to obtain

$$a\Lambda_L \approx \left(\frac{48\pi^2}{11\lambda}\right)^{51/121} \exp\left(-\frac{24\pi^2}{11\lambda}\right)(1 + C_1(N)\lambda)\ , \tag{4.28}$$

which shows the relation between the lattice spacing a and the 't Hooft coupling λ. $C_1(N)$ encodes the N dependence of a, and goes to a finite value in the large N limit. Λ_L appears as an integration constant and is the lattice analogue to Λ_{QCD} in the continuum, which provides the natural scale of the theory. As mentioned before, the continuum limit is taken when $a \to 0$, which corresponds to $\lambda \to 0$.

Several quantities can be used to fix the renormalization procedure and certainly using the ratio of two physical masses is one possible option. In principle, one can use any renormalized coupling for the same matter, and so let us choose the dimensionless quantity defined as $\langle t^2 e^t \rangle$ where $\langle e^t \rangle$ is defined as in Eq. (4.25). By fixing this quantity one fixes a scale, and as pointed out in Ref. [78], a sensible choice in SU(3) is to use the condition[5]

$$\langle t^2 e^t \rangle\,|_{t=t_0} = 0.3\,. \tag{4.29}$$

[4]Notice again that this corresponds to a cut-off dependence of the bare parameter in the renormalization procedure.

[5]This is not the only condition that one can use, see Refs. [87, 88].

To generalize this to the gauge group SU(N), let us look at the perturbative expansion of $\langle e^t \rangle$ at small t

$$\langle t^2 e^t \rangle = \frac{3}{128\pi^2} \frac{N^2-1}{N} \lambda(q) \left[1 + c_1 \lambda(q) + \mathrm{O}(\lambda_t^2)\right] \tag{4.30}$$

where $\lambda(q) = N g^2_{\overline{\mathrm{MS}}}(q)$ is the renormalized 't Hooft coupling at the scale $q = (8t)^{-1/2}$, and the constant $c_1 = \frac{1}{16\pi^2}(\frac{11}{3}\gamma_E + \frac{52}{9} - 3\ln 3)$ is N independent. This allows us to define a reference scale which is constant at leading order in the $1/N$ expansion. As we have introduced in Ref. [89], this is achieved by choosing

$$\langle t^2 e^t \rangle |_{t_0} = 0.1125(N^2-1)/N\,, \tag{4.31}$$

where the N dependence is motivated by Eq. (4.30) and the prefactor is chosen to attain the canonical value of 0.3 in SU(3)[6]. Once the scale has been fixed, it can be used to express any observable computed in the lattice, such as the topological susceptibility χ_{YM}, which in dimensionless units is written as $t_0^2 \chi_{\mathrm{YM}}$.

This is our scale of choice in this work, as it can be defined entirely depending on pure glue operators. Besides, it has been shown to have small statistical uncertainties, and can therefore be computed with a relatively low computational effort. All of which are desirable characteristics of a good scale in the lattice [88].

4.4 Open boundary conditions

A solution for the problem of topology freezing was proposed in Ref. [80], which consists in changing the lattice geometry so that the different topological sectors become connected. Basically, the proposal consists in adding Dirichlet boundary conditions for one of the directions, while the others, as usual, obey periodic boundary conditions. In the continuum, the boundary conditions are given by

$$F_{0k}(x)|_{x_0=0} = F_{0k}(x)|_{x_0=T} = 0\,, \qquad k = 1,2,3, \tag{4.32}$$

where $F_{\mu\nu}$ is the field strength tensor. This choice preserves gauge invariance so it does not restrict the gauge degrees of freedom of the system. Moreover, by imposing these conditions, it can be proved that all fields $A_\mu(x)$ are continuously connected to the classical vacuum configuration $A_\mu(x) = 0$, and therefore the field space is connected.

On a lattice of time extent $T + a$ and spatial dimensions L^3, open boundary conditions can be imposed in an straightforward way. Eq. (4.32) translates to adding a weight $\omega_{\mu\nu}(x)$ to the lattice gauge action, such that it is equal to 1 for all the

[6] A recent analysis of the N dependence of t_0 has been presented in Ref. [90], by computing the ratio of the scales $\sqrt{t_0}/r_1$ at different values of N.

plaquettes which are fully contained in the time interval $[0, T]$, 1/2 for the spatial plaquettes at $x_0 = \{0, T\}$, and 0 otherwise

$$S_G[U] = \frac{1}{g^2} \sum_{x,\mu,\nu} \omega_{\mu\nu}(x) \operatorname{Tr}\left\{1 - U_{\mu\nu}(x)\right\} . \tag{4.33}$$

Concerning renormalization, it is not affected by the open boundary conditions [80]. However, due to the presence of the boundaries, a state $|\gamma\rangle$ with the same quantum numbers as the vacuum appears when considering the spectral representation of the partition function. Let us denote with $\mathbb{T}$ the positive definite transfer matrix associated to the Hamiltonian formulation of the Wilson lattice theory; thus, the partition function $\mathcal{Z}$ can be written in the transfer matrix formalism as $\mathcal{Z} = \langle\gamma| \mathbb{T}^{\frac{T}{a}} |\gamma\rangle$. Then, for an observable $\mathcal{O}(x_0)$ with $x_0 \in [0, T]$ we can write

$$\langle \mathcal{O}(x_0) \rangle_{\text{OBC}} = \frac{1}{\mathcal{Z}} \langle\gamma| \mathbb{T}^{\frac{T-x_0}{a}} \mathcal{O}(x_0) \mathbb{T}^{\frac{x_0}{a}} |\gamma\rangle . \tag{4.34}$$

Now, writing $|\gamma\rangle = \sum_n a_n |n\rangle$, where $|n\rangle$ are eigenstates of the Hamiltonian with quantum numbers of the vacuum, and eigenvalues E_n (such that $E_n < E_{n+1}$), we have

$$\begin{aligned} \langle \mathcal{O}(x_0) \rangle_{\text{OBC}} &= \frac{1}{\mathcal{Z}} \sum_{n,m} a_n^* a_m \langle n| \mathbb{T}^{\frac{T-x_0}{a}} \mathcal{O}(x_0) \mathbb{T}^{\frac{x_0}{a}} |m\rangle \\ &= \frac{1}{\mathcal{Z}} \sum_{n,m} a_n^* a_m e^{-E_n(T-x_0)} e^{-E_m x_0} \langle n| \mathcal{O}(x_0) |m\rangle . \end{aligned} \tag{4.35}$$

It is clear that for large x_0 and $T - x_0$, the sum is dominated by the contribution from the state $|0\rangle$, while the next excited state has a decaying exponential contribution depending on the energy difference $\Delta E_1 = E_1 - E_0$

$$\langle \mathcal{O}(x_0) \rangle_{\text{OBC}} = \frac{|a_0|^2 e^{-E_0 T}}{\mathcal{Z}} \langle 0| \mathcal{O}(x_0) |0\rangle + \mathrm{O}\left(e^{-\Delta E_1 (T-x_0)} + e^{-\Delta E_1 x_0}\right) . \tag{4.36}$$

Through a similar analysis, one can show that the leading contribution to the partition function is given by $\mathcal{Z} \to |a_0^2| e^{-E_0 T}$. From here one recovers the standard vacuum expectation value for $\mathcal{O}(x_0)$. In the case of observables computed from the gradient flow, they carry a Gaussian profile footprint with mean square radius $\sqrt{8t}$, so at sufficiently large separations, their modification to the exponential decay in Eq. (4.36) is negligible [79].

The result of Eq. (4.36) is realized explicitly when looking at the x_0 dependence of observables computed in the lattice. As shown in Figure 4.1 the x_0 dependence can be accurately parametrized by a single state which propagates from the boundary. Vacuum expectation values are then extracted from the plateau region where the boundary effects are negligible.

4.4.1 Choosing the plateau region

Throughout the analysis in this work, we use the same prescription to deal with the extraction of vacuum expectation values using OBC, so we describe it here. Basically, we need to define a plateau region $x_0 \in [d, T-d]$ where the effects of the boundaries can be safely neglected. To determine the right value of d, the data is symmetrized in the time direction and fitted to an ansatz of the form $f(x_0) = A + Be^{-mx_0}$, where A, B and m are constants. Then, the criterion to define the plateau is the following

$$|f(d) - A| < \sigma/4\,, \tag{4.37}$$

where σ is the statistical error at the point[7] d. Clearly, by doing so, the influence of the states propagating from the boundary is negligible in comparison to the statistical errors. We give an example of how this looks in Figure 4.1 for two observables on an SU(4) ensemble with $\beta = 11.14$ and $T/a \times (L/a)^3 = 64 \times 16^3$. The observables are computed at flow time $t = t_0$ as defined in Eq. (4.31). The exact x_0-value where the plateau begins also depends on the choice of the fit range. We choose the fit range to begin at the point where $\chi^2/\mathrm{dof} < 2.0$ and then manually check that it is a good choice. This procedure guarantees a good fit to the data and we observe the plateau to be generally stable under a change of the initial point in the fit range by one or two lattice units.

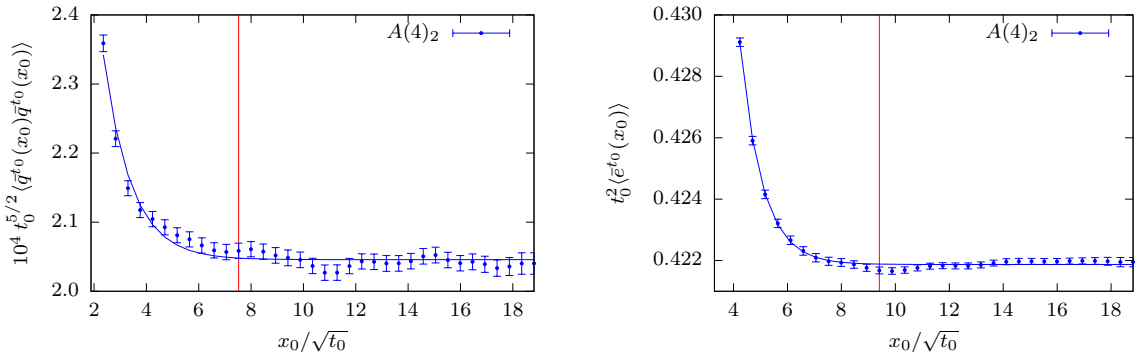

Figure 4.1: Plot of boundary effects. The propagating state from the boundary can be parametrized by a single exponential in the chosen range. The red vertical line shows the value at which boundary effects are considered to be negligible for each observable. The bar above the topological charge density q, and the Yang-Mills energy density e, indicates that they have been averaged over the spatial directions.

[7] Another option is to choose σ as the average statistical error over the plateau region. We have not observed any difference between both choices.

5. Multilevel algorithms

A major problem with lattice computations in the Yang-Mills gauge theory has to do with the so called signal to noise problem that affects the computation of large Wilson loops and correlation functions of hadronic and gluonic correlators [17, 91]. The authors in Ref. [18] devised an elegant solution to this problem, known as the multilevel algorithm, and applied it to the case of large Wilson loops. The basic idea was shortly after extended to correlation functions in Ref. [92].

In this chapter, we describe an algorithm which implements the multilevel paradigm to the case of observables $\mathcal{O}^t(x_0)$ computed at positive flow time. By using it, the decreasing of errors is faster than the standard $1/\sqrt{n}$ scaling of traditional simulations, where n is the number of independent measurements. In the following we introduce the theoretical basis of the multilevel approach for the case of two point functions, and then present our algorithm for the case of flow observables. The main results presented in this section have already been published in Ref. [93].

5.1 The multilevel algorithm

The basic idea behind the multilevel algorithm is to decompose observables in contributions which depend on independent sections of the lattice. Then, if the action and the update procedure are local, each section can be updated independently and the errors reduce faster than $1/\sqrt{n}$. The procedure can be applied to pure gauge simulations where the Wilson action and the commonly used hybrid over-relaxation update are both local.

As we discuss in Chapter 6, a precise computation of the topological susceptibility relies on the evaluation of the $\langle q(x)q(0)\rangle$ correlator at large distances. This is our motivation to study how the multilevel algorithm applies to two point functions, so we discuss them in the following sections.

5.1.1 Factorization of the two point function

Let us consider an SU(N) Yang-Mills gauge theory on the lattice with the standard Wilson action in Eq. (4.3). Then, define three subsets of gauge links L, B and R to

be disjoint such that the gauge action can be written as

$$S_G\left(U_L, U_B, U_R\right) = S_L\left(U_L, U_B\right) + S_B\left(U_B\right) + S_R\left(U_B, U_R\right) \equiv S_L + S_B + S_R\,, \quad (5.1)$$

where $U_{L,B,R}$ are the gauge links in L, B and R respectively. For simplicity (and without loss of generality), take B to be the set of spatial gauge links at the timeslice $x_0 = x_0^B$ as shown in Figure 5.1.

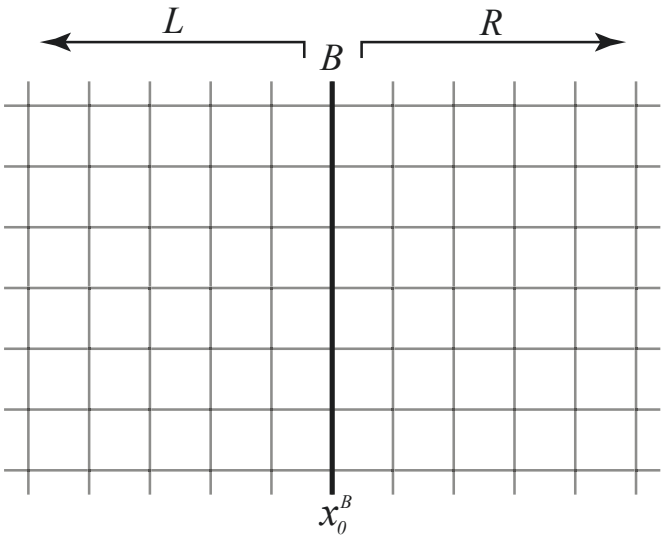

Figure 5.1: Setup for the multilevel formalism. The lattice is split into two sub-volumes L and R which are separated by the boundary B at the timeslice $x_0 = x_0^B$. Figure from Ref. [93].

Consider now the correlation function $\left\langle \mathcal{O}(x)\mathcal{O}'(y)\right\rangle$, where $\mathcal{O}(x)$ is a gluonic observable constructed only from the gauge links $U_L \in L$, and similarly for $\mathcal{O}'(y)$ which is given only in terms of gauge links $U_R \in R$

$$\left\langle \mathcal{O}(x)\mathcal{O}'(y)\right\rangle = \frac{\int\, dU\, \mathcal{O}(x)\mathcal{O}'(y)e^{-S_G}}{\int\, dU\, e^{-S_G}} = \frac{\int\, dU_B dU_L dU_R\, \mathcal{O}(x)\mathcal{O}'(y)e^{-S_B-S_L-S_R}}{\int\, dU\, e^{-S_G}} \quad (5.2)$$

$$= \frac{\int\, dU_B \left\{dU_L\, \mathcal{O}(x)e^{-S_L}\right\}\left\{dU_R\, \mathcal{O}'(y)e^{-S_R}\right\} e^{-S_B}}{\int\, dU\, e^{-S_G}}\,. \quad (5.3)$$

Then we define

$$\left[\mathcal{A}\right]_{L,R}\left(U_B\right) = \frac{1}{Z_{L,R}} \int\, dU_{L,R} \mathcal{A} e^{-S_{L,R}}\,, \quad (5.4)$$

where $Z_{L,R} = \int dU_{L,R} e^{-S_{L,R}}$ is such that $[1]_{L,R} = 1$. Using this,

$$\begin{aligned} \left\langle \mathcal{O}(x)\mathcal{O}'(y) \right\rangle &= \frac{\int dU_B \left[\mathcal{O}(x)\right]_L \left[\mathcal{O}'(y)\right]_R Z_L Z_R e^{-S_B}}{\int dU\, e^{-S_G}} \\ &= \int dU_B p(B) \left[\mathcal{O}(x)\right]_L \left[\mathcal{O}'(y)\right]_R , \end{aligned} \tag{5.5}$$

where

$$p(B) = \frac{Z_L Z_R\, e^{-S_B}}{Z} = \frac{\int dU_L dU_R\, e^{-S_G}}{\int dU_B dU_L dU_R\, e^{-S_G}} = \frac{e^{-S_B} \int dU_L dU_R e^{-S_L - S_R}}{\int dU_B dU_L dU_R e^{-S_B - S_L - S_R}} . \tag{5.6}$$

Eq. (5.5) shows that one can compute the correlation function $\left\langle \mathcal{O}(x)\mathcal{O}'(y) \right\rangle$ in two steps. First, compute $[\mathcal{O}]_L$ and $[\mathcal{O}']_R$ independently in their respective subvolume for a fixed B, and then integrate over all the boundary configurations U_B. The way this works in practice is by updating the links in L and R independently while keeping B fixed, and later calculate the expectation value over different U_B field configurations.

5.1.2 Scaling of errors

Let us now put this in the context of our Monte-Carlo simulations. First, generate n_0 configurations updating the whole lattice. These will be used to perform the integral over U_B. Then, using the locality of the action, the links in L and R can be updated independently to generate a total of n_1 configurations each. Naively, we have performed $n_0 \times n_1$ updates of the full lattice, so for a general observable we expect the error to be reduced as $1/\sqrt{n_0 n_1}$. We want to show that for connected correlators $\langle \mathcal{O}(x)\mathcal{O}(y) \rangle_C$, the leading contribution to the error actually scales as $1/\left(\sqrt{n_0} n_1\right)$.

Let us start from the observable

$$A = \mathcal{O}(x)\mathcal{O}(y) , \tag{5.7}$$

where $\mathcal{O}(x)$ depends on the links $U_L \in L$ and $\mathcal{O}(y)$ depends on $U_R \in R$. To simplify the notation let us drop the explicit coordinate dependence, and to differentiate between source and sink, let us denote $\mathcal{O} \equiv \mathcal{O}(x)$ and $\mathcal{O}' \equiv \mathcal{O}(y)$.

In our Monte-Carlo simulation, an estimator for the real expectation value $\langle A \rangle$ is given by

$$\hat{A} = \frac{1}{n_0} \sum_{i=1}^{n_0} \frac{1}{n_1^2} \sum_{j=1}^{n_1} \sum_{k=1}^{n_1} \mathcal{O}^{ij} \mathcal{O}'^{ik} . \tag{5.8}$$

Let us now study how the errors in this estimator scale with n_0 and n_1. To do that, let us assume that a very large number of Monte-Carlo simulations are performed with identical algorithms [66]. Each of these simulations is called a replica and consists on a Monte-Carlo chain generated from an independent random seed. Each individual measurement then has 4 indices, and one measurement of $\mathcal{O}$ is represented as $\mathcal{O}^{(i,r)(j,p)}$, where r and q are the replica indices which are related to the averages over U_B and U_L respectively. Notice that the case of $\mathcal{O}'$ is exactly equivalent after exchanging L by R. Let us now average over the replicas, performing first the average over U_L or U_R, and only later taking the average over the U_B fields. For the operator $\mathcal{O}$, we can take the average over an infinite number of replicas on the left section of the lattice for a fixed value of (i,r) [1]

$$\left[\mathcal{O}^{(i,r)}\right]_L^{\text{rep}} \equiv \lim_{P\to\infty} \frac{1}{P}\sum_{p=1}^{P} \mathcal{O}^{(i,r)(j,p)} = \left[\mathcal{O}^{(i,r)}\right]_L , \tag{5.9}$$

where the replica average agrees with $\left[\mathcal{O}^{(i,r)}\right]_L$ defined in Eq. (5.4), provided that we have taken the limit $P \to \infty$. Once the average over U_L has been performed, we can proceed similarly by summing over the index r

$$\langle \mathcal{O} \rangle^{\text{rep}} \equiv \lim_{R\to\infty} \frac{1}{R}\sum_{r=1}^{R} \left[\mathcal{O}^{(i,r)}\right]_L^{\text{rep}} = \langle \mathcal{O} \rangle \ . \tag{5.10}$$

Similarly, if we apply the replica average to the estimator $\hat{A}$, it is easy to see that $\left\langle \hat{A} \right\rangle^{\text{rep}}$ is equal to the vacuum expectation value $\langle A \rangle$. For convenience, in the remainder of this section, we will use either $\bar{\mathcal{O}}$ or $\langle \mathcal{O} \rangle$ to represent the real vacuum expectation value of an observable.

Neglecting correlations, the error σ_A^2 on the estimator $\hat{A}$ can be computed by

$$\sigma_A^2 \equiv \left\langle \left(\hat{A} - \bar{A}\right)^2 \right\rangle^{\text{rep}} = \lim_{R\to\infty} \lim_{P\to\infty} \lim_{S\to\infty} \frac{1}{RPS} \sum_{r=1}^{R}\sum_{p=1}^{P}\sum_{s=1}^{S} \left(\hat{A}^{(r,p,s)} - \bar{A}\right)^2 , \tag{5.11}$$

where the index r labels the replicas over U_B, p corresponds to the replicas over U_L, and s to those over U_R.

For simplicity, the analysis described in the following is done under the assumption that there is no autocorrelations between the measurements. This applies not only to the average over different replicas but to the averages inside each replica. Inserting $\hat{A}$ from Eq. (5.8) into Eq. (5.11) one obtains

[1] The presence of the indices (i,r) indicates explicitly that this average depends on the links in B.

$$\sigma_A^2 = \frac{1}{n_0^2 n_1^4} \sum_{i=1}^{n_0} \sum_{j,k=1}^{n_1} \sum_{l,m=1}^{n_1} \left\langle \mathcal{O}^{ij} \mathcal{O}'^{ik} \mathcal{O}^{il} \mathcal{O}'^{im} - \bar{A}^2 \right\rangle . \tag{5.12}$$

Organizing the terms in Eq. (5.12) in a convenient way one has

$$\sigma_A^2 = \frac{1}{n_0^2 n_1^4} \sum_{i,j,k,l,m} \left\langle \left\{ \mathcal{O}^{ij} \mathcal{O}^{il} \left[\delta^{jl} + \left(1 - \delta^{jl} \right) \right] \right\} \left\{ \mathcal{O}'^{ik} \mathcal{O}'^{im} \left[\delta^{km} + \left(1 - \delta^{km} \right) \right] \right\} - \bar{A}^2 \right\rangle , \tag{5.13}$$

where we are abusing the notation and we do not write limits in the sums over i, j, k, l, m as they have not changed with respect to Eq. (5.12). We can simplify this expression by noticing that

$$\left\langle \mathcal{O}^{ij} \mathcal{O}^{il} \mathcal{O}'^{ik} \mathcal{O}'^{im} \right\rangle = \left\langle \left[\mathcal{O}^{ij} \mathcal{O}^{il} \right]_L \left[\mathcal{O}'^{ik} \mathcal{O}'^{im} \right]_R \right\rangle . \tag{5.14}$$

Each factor can be evaluated independently, so let us evaluate the first one explicitly

$$\left[\mathcal{O}^{ij} \mathcal{O}^{il} \right]_L = \delta^{jl} \left[\left(\mathcal{O}^i \right)^2 \right]_L + \left(1 - \delta^{jl} \right) \left(\left[\mathcal{O}^i \right]_L \right)^2 = \delta^{jl} \Delta_L \left(\mathcal{O}^i \right) + \left(\left[\mathcal{O}^i \right]_L \right)^2 , \tag{5.15}$$

where $\Delta_L \left(\mathcal{O}^i \right) = \left[\left(\mathcal{O}^i \right)^2 \right]_L - \left(\left[\mathcal{O}^i \right]_L \right)^2$ can be related to a variance term defined on L for a fixed B. A similar expression is obtained for the second factor, so that when put together back in Eq. (5.13) one has

$$\sigma_A^2 = \frac{1}{n_0^2 n_1^4} \sum_{i,j,k,l,m} \left\langle \left(\delta^{jl} \Delta_L \left(\mathcal{O}^i \right) + \left(\left[\mathcal{O}^i \right]_L \right)^2 \right) \left(\delta^{km} \Delta_R \left(\mathcal{O}'^i \right) + \left(\left[\mathcal{O}'^i \right]_R \right)^2 \right) - \bar{A}^2 \right\rangle \tag{5.16}$$

Finally, after performing all the sums

$$\begin{aligned} \sigma_A^2 = \frac{1}{n_0 n_1^2} \left\langle \Delta_L \left(\mathcal{O} \right) \Delta_R \left(\mathcal{O}' \right) \right\rangle + \frac{1}{n_0} \left(\left\langle \left(\left[\mathcal{O} \right]_L \right)^2 \left(\left[\mathcal{O}' \right]_R \right)^2 \right\rangle - \bar{A}^2 \right) + \\ + \frac{1}{n_0 n_1} \left(\left\langle \Delta_L \left(\mathcal{O} \right) \left(\left[\mathcal{O}' \right]_R \right)^2 + \Delta_R \left(\mathcal{O}' \right) \left(\left[\mathcal{O} \right]_L \right)^2 \right\rangle \right) , \end{aligned} \tag{5.17}$$

From Eq. (5.17) we can analyse what is the leading contribution to the scaling of the error in the estimator. As we have mentioned, in the ideal case, the error σ_A of the multilevel algorithm is expected to scale as $1/\left(\sqrt{n_0} n_1 \right)$. This is the case of the first term, so the rest of terms should produce subleading contributions.

The argument of how this suppression actually occurs is given in Appendix B. Basically, if source and sink are placed sufficiently far away from the boundary B, $[\mathcal{O}]_L$ decays faster than the contribution from $\Delta_L(\mathcal{O})$ (and similarly for the terms which depends on R). Let us note that when $\mathcal{O}$ does not couple to the vacuum, both the second and the third term in Eq. (5.17) are suppressed exponentially with the mass of the lightest state compatible with the symmetries of the operator. However, if the operator couples to the vacuum, only the second term is suppressed, and the term proportional to $1/\sqrt{n_1 n_0}$ decays exponentially only if one considers the case of the connected correlator

$$\langle C \rangle = \langle \mathcal{O}(x_0)\mathcal{O}(y_0) \rangle - \langle \mathcal{O}(x_0) \rangle \langle \mathcal{O}(y_0) \rangle = \langle A \rangle - \langle \mathcal{O} \rangle \langle \mathcal{O}' \rangle \,. \tag{5.18}$$

Same as done before, we want to compute the error for the estimator σ_C^2

$$\begin{aligned}\sigma_C^2 &= \left\langle \left(\hat{A} - \hat{\mathcal{O}}\hat{\mathcal{O}}' - \left(\bar{A} - \bar{\mathcal{O}}\bar{\mathcal{O}}' \right) \right)^2 \right\rangle^{\text{rep}} \\ &= \left\langle \left(\left(\hat{A} - \bar{A} \right) - \bar{\mathcal{O}}' \left(\hat{\mathcal{O}} - \bar{\mathcal{O}} \right) - \bar{\mathcal{O}} \left(\hat{\mathcal{O}}' - \bar{\mathcal{O}}' \right) - \left(\hat{\mathcal{O}} - \bar{\mathcal{O}} \right) \left(\hat{\mathcal{O}}' - \bar{\mathcal{O}}' \right) \right)^2 \right\rangle^{\text{rep}} .\end{aligned} \tag{5.19}$$

Clearly, when evaluating σ_C^2, the already calculated term σ_A^2 appears again. From the remaining terms, those which include more than 2 products of estimators are suppressed by at least one extra power of $1/n_0$. The leading terms that need to be evaluated are

$$\left\langle \left(\hat{\mathcal{O}} - \bar{\mathcal{O}} \right)^2 \right\rangle^{\text{rep}} , \quad \left\langle \left(\hat{A} - \bar{A} \right) \left(\hat{\mathcal{O}} - \bar{\mathcal{O}} \right) \right\rangle^{\text{rep}} , \quad \left\langle \left(\hat{\mathcal{O}} - \bar{\mathcal{O}} \right) \left(\hat{\mathcal{O}}' - \bar{\mathcal{O}}' \right) \right\rangle^{\text{rep}} ,$$

plus those terms which are symmetric on the interchange of $\mathcal{O}$ and $\mathcal{O}'$. Writing this explicitly we have

$$\begin{aligned}\sigma_c^2 \approx \sigma_A^2 &- 2\bar{\mathcal{O}}' \left\langle \left(\hat{A} - \bar{A} \right) \left(\hat{\mathcal{O}} - \bar{\mathcal{O}} \right) \right\rangle^{\text{rep}} - 2\bar{\mathcal{O}} \left\langle \left(\hat{A} - \bar{A} \right) \left(\hat{\mathcal{O}}' - \bar{\mathcal{O}}' \right) \right\rangle^{\text{rep}} + \\ &2\bar{\mathcal{O}}\bar{\mathcal{O}}' \left\langle \left(\hat{\mathcal{O}} - \bar{\mathcal{O}} \right) \left(\hat{\mathcal{O}}' - \bar{\mathcal{O}}' \right) \right\rangle^{\text{rep}} + \bar{\mathcal{O}}'^2 \left\langle \left(\hat{\mathcal{O}} - \bar{\mathcal{O}} \right)^2 \right\rangle^{\text{rep}} + \bar{\mathcal{O}}^2 \left\langle \left(\hat{\mathcal{O}}' - \bar{\mathcal{O}}' \right)^2 \right\rangle^{\text{rep}} ,\end{aligned} \tag{5.20}$$

plus terms of $\mathrm{O}(1/n_0^2)$.

After evaluating all the terms (see Appendix B), one can show that only the first term in Eq. (5.17) gives the leading contribution to the error. The final formula for the error of the connected correlator is then

$$\sigma_C^2 \approx \frac{1}{n_0 n_1^2} \left\langle \Delta_L \left(\mathcal{O}\right) \Delta_R \left(\mathcal{O}'\right) \right\rangle_B + e^{-\Delta E_1 |x_0^B - x_0^M|} \left(\frac{c_1}{n_0 n_1} + \frac{c_2}{n_0} \right) , \tag{5.21}$$

where x_0^M is either x_0 or y_0, whichever is the closest to x_0^B, and $c_1\,, c_2$ are constants.

5.1.3 Modified flow observables

Now that we have presented the theoretical grounds to understand how the multilevel algorithm improves on the error scaling, let us explain how we combine it with observables computed at positive flow time. The fundamental problem with flow observables is that they are not local, so any observable defined in L or R has a non-trivial dependence on gauge links from the complementary domain. However, given that the smoothing of the flow is exponentially suppressed at large distances, we propose a slightly modified version of the flow equations such that the modified flow gauge links $\tilde{V}^t$ are compatible with factorization, and Eq. (5.5) can be applied.

If the Wilson action is also used in the definition of the flow, we propose the following modified flow equation

$$\begin{aligned} &\dot{\tilde{V}}_\mu^t(x) = -g_0^2 \left\{ \partial_{x,\mu} S(\tilde{V}^t) \right\} \tilde{V}_\mu^t(x), \quad \tilde{V}_\mu^{t=0}(x) = U_\mu(x), \quad \text{if } U_\mu(x) \in L \cup R\,, \\ &\tilde{V}_\mu^t(x) = U_\mu(x), \qquad\qquad\qquad\qquad\qquad\qquad\qquad\quad \text{if } U_\mu(x) \in B. \end{aligned} \tag{5.22}$$

The modified version integrates the gauge links with the standard flow equations while the links at B are kept fixed. We can use this to define new observables $\widetilde{\mathcal{O}}^t(x)$ in either L or R which do not get a contribution from the opposite domain. Then, one can use the multilevel approach to obtain a better scaling of the errors for the connected two point correlation function.

5.1.4 Modified two point correlation function

With the modified flow observables, we turn back to our original problem which is to compute two point correlation functions of observables at positive flow time. Let us use the notation as in Ref. [93] so that for a general observable $\mathcal{O}^t(x)$ at positive flow time t we define

$$C_{\mathcal{O}}^t(x_0, y_0) = \left\langle \mathcal{O}^t(x_0) \mathcal{O}^t(y_0) \right\rangle_C = \left\langle \mathcal{O}^t(x_0) \mathcal{O}^t(y_0) \right\rangle - \left\langle \mathcal{O}^t(x_0) \right\rangle \left\langle \mathcal{O}^t(y_0) \right\rangle , \tag{5.23}$$

as the connected correlator which we want to evaluate. One can in principle replace the observable $\mathcal{O}^t(x_0)$ by $\widetilde{\mathcal{O}}^t(x_0)$, and keeping x_0 far from the boundary in units of the flow radius $\sqrt{8t}$, the errors should be negligible. In our approach we do not

simply neglect this error, but rather include it as a correction to the estimator as we explain in the following.

First, define the correction term as

$$\Delta^t_{\mathcal{O}}(x_0, y_0) = C^t_{\mathcal{O}}(x_0, y_0) - \widetilde{C}^t_{\mathcal{O}}(x_0, y_0)\,. \tag{5.24}$$

We then compute an estimator for the correction term in the first n_0 updates of the full lattice. For source and sink located far away from the boundary, our data shows that the statistical fluctuations in the correction term are very small compared to the statistical error of the correlator itself, so, given that we get a good estimate of the correction, we can afterwards perform the n_1 updates in L and R while maintaining the correction term correct up to the statistical error.

Our proposal is to define an estimator $\widehat{C}^t_{\mathcal{O}}(x_0, y_0)$ for $C^t_{\mathcal{O}}(x_0, y_0)$ as

$$\widehat{C}^t_{\mathcal{O}}(x_0, y_0) = \frac{1}{n_0}\sum_{i=1}^{n_0}\left\{\left[\widetilde{\mathcal{O}}^t(x_0)\right]^i_L\left[\widetilde{\mathcal{O}}^t(y_0)\right]^i_R + \Delta^{i\,t}_{\mathcal{O}}(x_0, y_0)\right\} \tag{5.25}$$

$$\left[\widetilde{\mathcal{O}}^t(z)\right]_{L,R} = \frac{1}{n_1}\sum_{j=1}^{n_1}\widetilde{\mathcal{O}}^{j\,t}(z)\,, \qquad z = x_0, y_0\,.$$

The presence of the correction term which is only evaluated on the n_0 initial configurations would suggest a $1/\sqrt{n_0}$ scaling, but as we will show, the errors in the correction term are exponentially suppressed, so the leading contribution comes from the first term in the sum. Clearly, if n_1 is large, at some point the contribution from the correction term becomes relevant. In practice, this happens only at very small separations. Notice that we have written explicitly the indices i and j in Eq. (5.25), but to simplify the notation, we will drop them in the rest of this chapter. Whether the quantities have an index running up to n_0 or n_1 should be clear from the context.

5.2 Results

In this section we present our numerical results for the multilevel algorithm from Eq. (5.25). All the computations were performed at the ZIB computer centre in Berlin, with the resources granted by the HLRN (North-German supercomputing alliance) as part of the project bep00053.

The particular observables we are interested in are the Yang-Mills energy density $e^t(x)$ and the topological charge density $q^t(x)$. In particular, the second quantity is used to define the topological susceptibility on the lattice through

$$\chi^t_{\text{YM}} = \frac{1}{V}\int dxdy\,\left\langle q^t(x)q^t(y)\right\rangle\,, \tag{5.26}$$

β	$(T/a) \times (L/a)^3$	t_0/a^2	$a\,[\mathrm{fm}]$	n_0
6.11	80×20^3	4.5776(15)	0.078	384

Table 5.1: Lattice parameters. We report the lattice bare coupling β, the lattice dimensions L and T, the scale parameter t_0 defined in [78], the lattice spacing a has been computed using the $r_0 = 0.5\,\mathrm{fm}$ scale from [96], and the number of generated configurations n_0.

where the topological charge density is defined at a positive flow time t. The computation of the correlator is severely affected by the signal to noise-problem and when performing the sum up to large distances, one can either model the large distance behaviour of $\langle q(x)q(y)\rangle$ [94] or neglect the tail if it is below the statistical uncertainty [79]. In our case, the subject of Chapter 6 is precisely the computation of χ_{YM}, so we will show there how the signal to noise problem affects the statistical errors on the topological susceptibility. Other than the computation of the topological susceptibility, the two-point function of the smoothed topological charge and the energy density have been used to extract glueball masses [95], so in that case it is also highly beneficial to find a way to improve in the error scaling of the two point function of these observables.

5.2.1 Assessment of the correction term $\Delta^t_{\mathcal{O}}$

Before we compute the estimator for the two point correlation function, we must make sure that the error from measuring the correction term only on the first n_0 updates is small. We look at the two observables

$$C^t_q(x_0, r) = \left\langle \bar{q}^t(x_0)\bar{q}^t(x_0 + r)\right\rangle_C, \qquad \bar{q}^t(x_0) = a^3 \sum_{\vec{x}} q^t(\vec{x}, x_0) \tag{5.27}$$
$$C^t_e(x_0, r) = \left\langle \bar{e}^t(x_0)\bar{e}^t(x_0 + r)\right\rangle_C, \qquad \bar{e}^t(x_0) = a^3 \sum_{\vec{x}} e^t(\vec{x}, x_0),$$

which have been summed over the three spatial coordinates to project the operators to the zero momentum sector. We performed some initial tests with 96 configurations of an SU(4) ensemble at $\beta = 11.14$ and a lattice of dimensions $(T/a) \times (L/a)^3 = 80 \times 20^3$ but for the final results we decided to work with an SU(3) ensemble to demonstrate our method in a more standard scenario. The parameters for the ensemble used in the final analysis are shown in Table 5.1.

We use the 384 configurations to understand the x_0 and r dependence of the statistical error of the correction term $\sigma(\Delta)$. Unless we explicitly state it to be different, our results are presented at the flow time $t = t_0$, so when it is not necessary we drop the superscript t from our observables. Let us consider first the symmetrical

case, where $x_0 = (T - r)/2$, so that r is the only relevant parameter. In Figure 5.2 we show the r dependence of the errors of Δ and those of the correlator itself. As a reference, the vertical line indicates the value at which the errors in the correction are below 5% of those of the correlator. Notice that at large separations, i.e., $|x-y| \gg 1$, the errors in the correction term are exponentially suppressed with respect to those of the correlator which remain constant. This already suggests that far away from the boundary, it is safe to use a small number of updates to measure Δ, and as the error is so small, the estimator can be used with confidence after $\widetilde{\mathcal{O}}(x_0)$ and $\widetilde{\mathcal{O}}(x_0 + r)$ have been updated n_1 times.

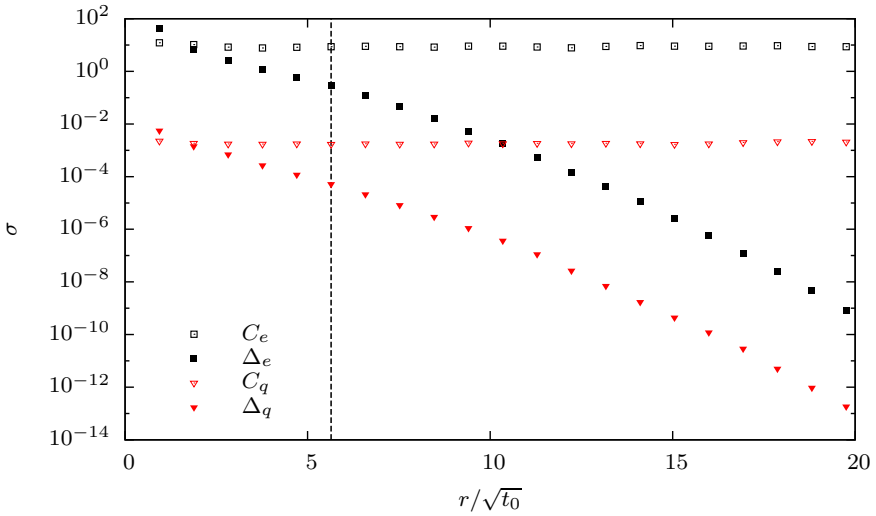

Figure 5.2: Plot of the errors σ of the correction term $\Delta_{\mathcal{O}}$ and the correlator $C_{\mathcal{O}}$ as a function of the distance to the boundary r. Figure from [93].

Next we look at the x_0 dependence of the errors. In Figure 5.3 we show the errors of Δ for two values of r where the position of the source (and sink respectively) is changed. We observe the errors to monotonically decrease up to the symmetric point where they are the smallest, as expected.

From both Figures 5.2 and 5.3 it is clear that sufficiently far away from the boundary B, the error in the estimator of the correction term is much smaller than the error in the correlator, and as suggested by the data, it decays exponentially with the distance. In practice, this means that we can perform a very large number of n_1 updates in L and R before the error of Δ becomes statistically significant. With this in mind, let us now compute the correlator and study the scaling of its errors.

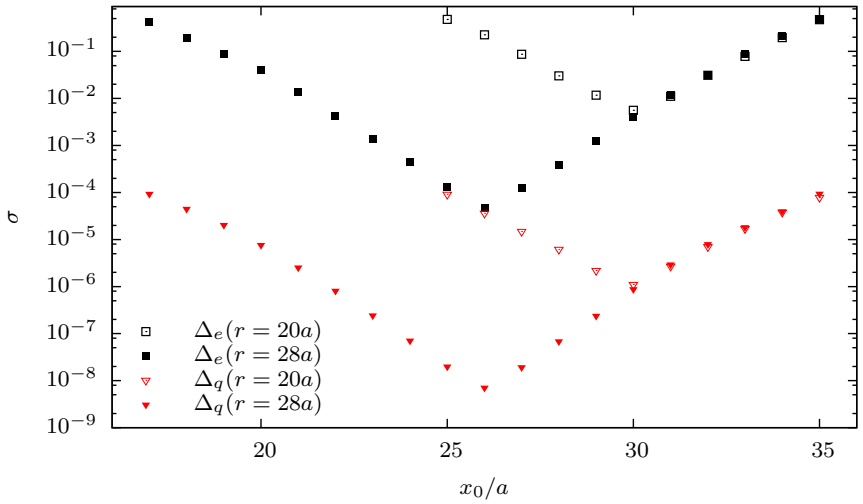

Figure 5.3: Statistical error $\sigma(\Delta)$ as a function of x_0 for two values of the distance r between source and sink. The errors are the smallest at the symmetrical point when both source and sink are the farthest from the boundary. Figure from [93].

5.2.2 Error scaling in the two-point function

After we have an understanding of the magnitude of the correction term Δ, we now turn to the computation of $\left[\widetilde{\mathcal{O}}^t(x_0)\right]_L \left[\widetilde{\mathcal{O}}^t(y_0)\right]_R$ in Eq. (5.25). For each of the $n_0 = 384$ initial configurations, we perform $n_1 = 40$ updates independently in L and R while keeping B fixed. The measurements are performed with a separation of 60 updates, where one update is composed of 8 over-relaxation updates followed by one heat-bath update. In both cases, we use the Cabibbo-Marinari strategy and update the three SU(2) subgroups of each SU(3) matrix.

Autocorrelation times

A valid question concerning the n_1 multilevel updates is whether keeping B frozen through the simulation has an effect on the integrated autocorrelation times τ_{int} of the observables. In principle, this could have an effect on the cost of the simulation, but as we plot in Figure 5.4, our data shows that τ_{int} increases at most by a factor of 1.5 when the observables approach the boundary B. Given that we investigate the autocorrelation in terms of n_1, we should be more explicit about the way it is calculated. Given that the original n_0 updates are completely decorrelated, for each of them we can compute the autocorrelation function as a function of n_1 and then average over the n_0 configurations

$$\tilde{\Gamma}(t) = \frac{1}{n_0} \sum_{i=1}^{n_0} \Gamma^i(t)\,. \tag{5.28}$$

Then, the integrated autocorrelation time is defined in the usual way (Eq. (4.12)) using the averaged autocorrelation function $\tilde{\Gamma}(t)$.

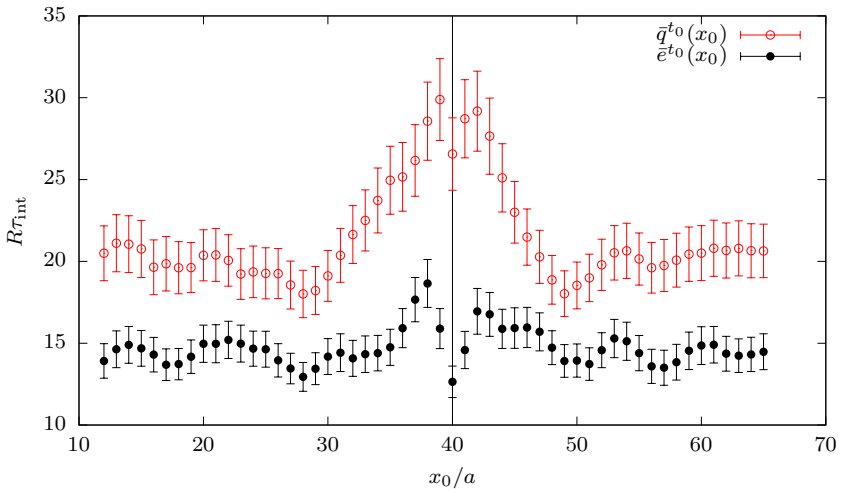

Figure 5.4: Integrated autocorrelation time $\tau_{\rm int}$ in unit of updates for both $\bar{e}$ (black filled points) and $\bar{q}$ (red open points) as a function of x_0. For both observables we do not observe an uncontrolled growth of the autocorrelation even in the vicinity of the boundary B. The meaning of the normalization constant R is explained as part of Appendix A, but for now, it does not affect our discussion.

Dependence of the error on the nested n_1 updates

Once we have shown that autocorrelations are under control, we can look at the scaling of errors with respect to the n_1 updates. Let us first comment on the fact that although n_1 can be taken very large, one must remember that the ideal scaling $1/\sqrt{n_0 n_1}$ is simply the leading term, and as shown in Eq. (5.21), it is only valid up to corrections of $\mathrm{O}(e^{-\Delta E_1 |x_0^B - x_0^M|})$. In addition, using the correction term Δ introduces another correction to the leading scaling of the error. This correction, as seen previously, is also exponentially suppressed and in this case, the relevant scale is the flow radius $\sqrt{8t}$. Therefore, at large distances from the boundary B, the leading behaviour of the error scaling is valid up to very large values of n_1, but the exact meaning of "very large n_1" must be checked.

To test the validity of the ideal scaling law, we have looked at the correlators $\widehat{C}_e$ and $\widehat{C}_q$ at different values of the source to sink separation r. In particular, for $r = 14a \approx 6.6\sqrt{t_0}$ and $r = 28a \approx 13.2\sqrt{t_0}$ we plot our results in Figure 5.5. In

all cases, except that of $\widehat{C}_e$ at the smaller separation, our data shows an scaling compatible with the ideal $1/n_1$ law. For the one particular case where it does not work, the leading approximation is no longer valid and effectively we can use only up to $n_1 \approx 6$ nested updates to benefit from the accelerated error reduction. This also shows that for a given n_0 and r, the region where the ideal $1/n_1$ scaling law is valid is observable dependent and has to be studied on a case by case basis. In our case, we find that for separations $r \geq 16a \approx 7.5\sqrt{t_0}$ the ideal scaling up to $n_1 = 40$ is valid for our two observables.

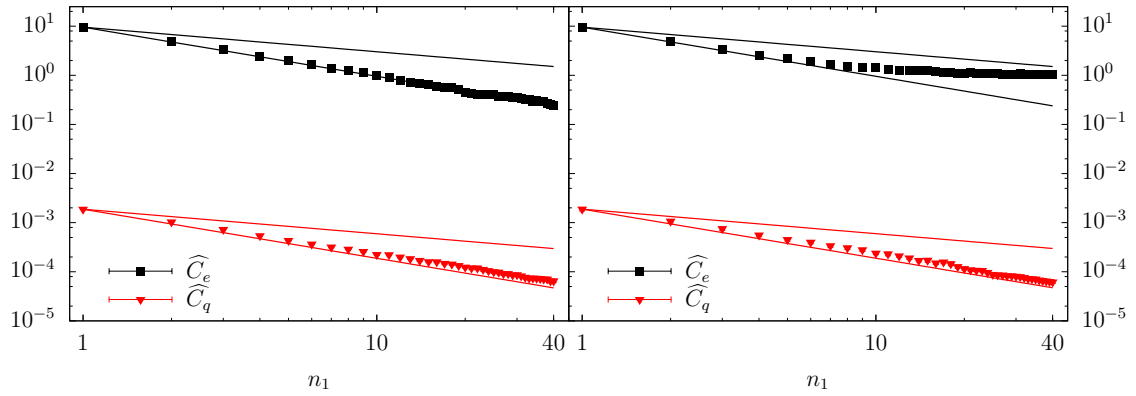

Figure 5.5: Scaling of the error of $\widehat{C}_{\mathcal{O}}$ as a function of n_1. On the left for a source to sink separation $r = 28a$ and on the right for $r = 14a$. The solid line corresponds to an scaling law $1/n_1$, while the dotted line corresponds to the standard $1/\sqrt{n_1}$. For the larger separation, we observe a scaling compatible with the ideal formula, while for the shorter separation, $\widehat{C}_e$ is already saturated at $n_1 \approx 6$, which shows that the ideal scaling is no longer dominant. Figure from [93].

The two point-correlation function

We are now in a position to perform a real computation of the two point correlation function. In order to study the performance of our algorithm we now use the full lattice (minus the region excluded to avoid open boundary effects) to average the $\widehat{C}_{\mathcal{O}}$ correlator as in a standard computation. In the standard case, one would compute the correlator at all possible values of x_0 and then average over the plateau region in the centre of the lattice. In our case, due to the presence of the boundary at x_0^B we proceed differently.

The first condition to consider is that close to the boundary, the error of the correction term is not smaller than the one of the correlator itself. In this case, it will dominate the total error, which renders performing the n_1 nested updates non-beneficial. Moreover, close to the boundary, as we have shown in Figure 5.5, the n_1 dependence of the error plateaus for small values of n_1 so we have no gain from all

the $n_1 = 40$ updates. Considering this, we have observed that a sensible choice is to exclude from the averaging those cases on which source or sink are located at a distance $d \leq r_B$ from the boundary B. In our case, working at $t = t_0$, we find a good choice to be $r_B = 6a$. Notice that this is compatible with the flow radius $\sqrt{8t_0} \approx 6a$. We also looked at a value of $t = t_0/10$ and found $r_B = 3a$ to be a good choice. Working at this small value of the flow parameter could be interesting for example when attempting to obtain glueball masses from the correlator.

Let us discuss what the choice of r_B means. First, for $r < 2r_B$, the correlator $\widehat{C}_{\mathcal{O}}(x_0, r)$ is only computed in either L or R, which means that it would not benefit from the ideal scaling law as both source and sink belong to the same sub-domain. In fact, considering that we cannot average over the whole plateau region, the final error is larger than the one expected from the standard algorithm. For intermediate values of r, one has cases in which $x_0 \in L$ and $x_0 + r \in R$, as well as cases in which both belong to only one of the domains. In the latter case, the error scales as $1/\sqrt{n_0 n_1}$ so we find it beneficial to also exclude them from the averaging. Similar as for small distances, this means that we loose because of volume averaging with respect to the standard algorithm, but the better scaling law $1/\sqrt{n_0} n_1$ quickly compensates and overturns this effect. Finally, at large distances, we have the pure effect of the multilevel updates, so the ideal scaling is observed.

These different regimes can be observed in Figure 5.6 where we show the ratio of the errors of the standard algorithm with $n_0 = 384$ and those obtained with our multilevel scheme using $n_0 \times n_1 = 384 \times 40$ updates. In the standard case, we would expect the increase in statistics to result in a reduction of errors by a factor of $\sqrt{40} \approx 6.3$. This is shown by the lower horizontal line in the Figure 5.6, and as discussed previously, our data shows that for small distances, the improvement is somewhat lower than the standard one. We observe the same effect at two different values of the flow time $t = t_0$ and $t = t_0/10$. For separations larger than $2r_B$, the multilevel algorithm is already better than the standard one and the performance gradually increases. This again is explained by the fact that at longer distances, the new algorithm suffers less from missing volume averaging. Finally, at large distances, the theoretical ideal scaling is achieved and the error scales as $1/n_1$.

As we mentioned previously, it is important to have a good control over the errors in the long distance region of the C_q correlator. We will discuss more about these effects in the next chapter when we compute the topological susceptibility χ_{YM}, but let us finish this chapter showing the equivalent plot to Figure 5.6, but in this case plotting the C_q correlator directly. At both $t = t_0/10$ and $t = t_0$, it is clear that at long distances, the correlator suffers wild fluctuations, and if one does not use very high precision data, summing the correlator up to the whole extent of the plateau does not yield a better signal but simply increases the errors.

In fact, if we define the topological susceptibility as

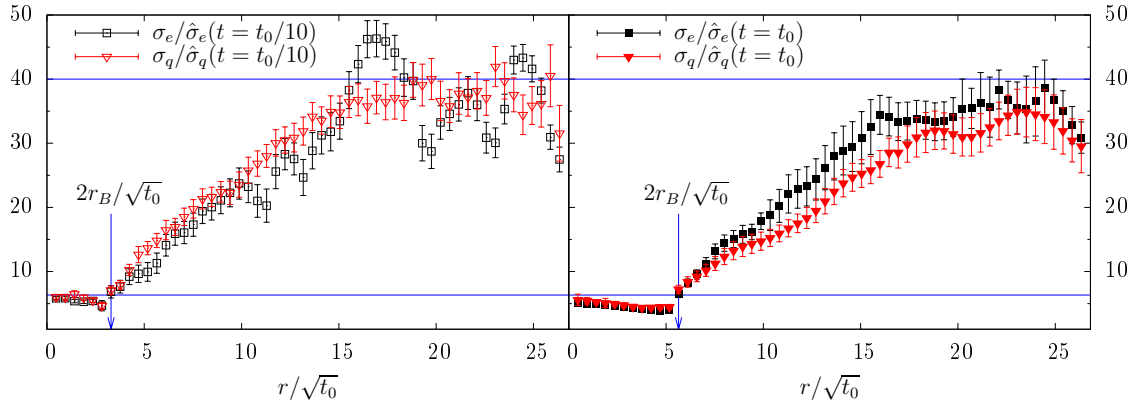

Figure 5.6: Ratio of the errors of the standard algorithm $\sigma_{\mathcal{O}}$ and the improved one $\widehat{\sigma}_{\mathcal{O}}$ as a function of r. On the left for a flow time $t = t_0/10$ and on the right for $t = t_0$. Notice that the error scaling behaves as expected. Figure from [93].

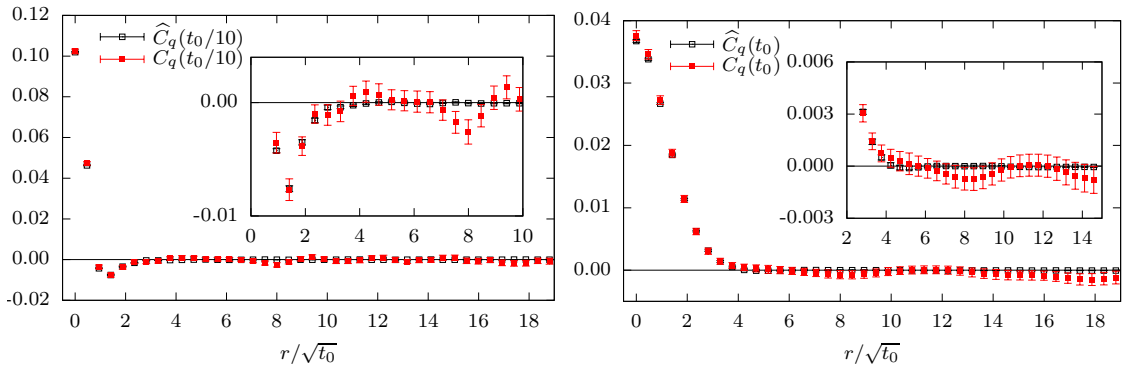

Figure 5.7: Plot of the correlators C_q and $\widehat{C}_q$ as a function of r. On the left for $t = t_0/10$ and on the right for $t = t_0$. The much more precise results in open symbols show that the contribution of the tail of the correlator is negligible compared to the errors from the standard correlator at values of $r \gtrsim 5\sqrt{t_0}$.

$r_{\rm cut}/\sqrt{t_0}$	$r_{\rm cut}$ [fm]	Standard	New
5.1	0.85	6.405(46)	6.347(60)
15.4	2.56	6.507(94)	6.291(61)
25.2	4.19	6.518(164)	6.254(69)

Table 5.2: Results for the topological susceptibility $10^4 t_0^2\,\chi(r_{\rm cut})$ at $t = t_0$ using the standard algorithm and the multilevel algorithm that we propose. The values of $r_{\rm cut}$ in physical units were computed using the r_0 scale from [96]. Table from Ref. [93].

$$\chi(r_{\rm cut}) = \frac{a}{L^3} \sum_{z_0=-r_{\rm cut}}^{r_{\rm cut}} \overline{C}_q(|z_0|)\,, \tag{5.29}$$

where $\overline{C}_q$ is the average over x_0 of $\widehat{C}_q(x_0, r)$, the effect of using different values of $r_{\rm cut}$ is clearly noticeable in Table 5.2. For the ensemble in Table 5.1, using our multilevel algorithm with $n_0 \times n_1 = 384 \times 40 = 15360$ updates and the standard one with the same number $n_0 = 15360$ of updates produces the results show in Table 5.2. Clearly at large distances, our algorithm outperforms the standard one where the result is affected by the statistical fluctuations of the tail of the correlator.

6. The large N limit of the topological susceptibility

As discussed in Chapter 3, computing the large N limit of the topological susceptibility $\chi_{\rm YM}$ in the pure gauge theory has phenomenological implications in the meson spectrum of QCD. Interestingly, from the Witten-Veneziano formula, the value of $\chi_{\rm YM}$ in SU(3) [97] has already a value large enough to explain the mass of the η' meson, which points to a mild N dependence of $\chi_{\rm YM}$. In this chapter we present our results concerning the computation of the large N limit of $\chi_{\rm YM}$ using an unambiguous lattice definition of the topological charge in terms of the Yang-Mills gradient flow and open boundary conditions. The main results of this chapter have been published in Ref. [89] and in the conference proceedings in Ref. [98].

The computation of $\chi_{\rm YM}$ has a long tradition in the lattice, and for the case of the 't Hooft limit in the pure Yang-Mills theory, there are several works in the literature which have computed this quantity with errors on the order of 10%. These results have been obtained in their majority using cooling techniques to define the topological charge in the lattice [99, 77, 100], and due to large autocorrelations, the simulations have been performed at relatively coarse lattice spacings.

Concerning the first point, although in several cases cooling has been shown to produce results numerically compatible to those from the gradient flow [101, 102], it does not rest on the same theoretical grounds as the latter, which has well defined renormalization properties. Another theoretically clean approach is to compute the topological charge by means of the index of the Dirac operator as in Ref. [103]. This approach is very expensive and if put together with the increase in cost proportional to N^3 for SU(N) simulations, makes it unpractical, which is the reason why the authors computed $\chi_{\rm YM}$ at only one lattice spacing at the largest gauge group SU(8).

In relation to the problem of large autocorrelations, we have already discussed the problem of critical slowing down in Chapter 4. As we will show in this chapter, using OBC allows us to sample the field space without incurring in an excessive cost.

6.1 Topology in the lattice

So far we have not made explicit the way in which we compute the topological charge density $q(x)$ on the lattice. To start, the definition of topology is ambiguous in the lattice, and the disconnected sectors emerge only when approaching the continuum [104, 105]. In spite of this, one can use the remnants of the topology from the continuum to classify the configurations into different topological sectors.

6.1.1 Gluonic definition

In principle it is straightforward to define a version of the topological charge density in the lattice

$$q^L(x) = \frac{1}{16\pi^2} \operatorname{Tr} F^L_{\mu\nu}(x)^* F^L_{\mu\nu}(x)\,, \tag{6.1}$$

where $F^L_{\mu\nu}$ is a suitable discretization of the field strength tensor. Such an approach is not guaranteed to produce integer values for the topological charge Q and the convergence depends on the specific discretization used [102]. A convenient choice is to use the Symanzik improved definition

$$F^L_{\mu\nu}(x) = \frac{1}{8a^2}\mathcal{P}\left(Q_{\mu\nu}(x) - Q^\dagger_{\mu\nu}(x)\right), \tag{6.2}$$

where $\mathcal{P}$ projects a $N \times N$ matrix to the $\mathfrak{su}(N)$ algebra and $Q_{\mu\nu}(x)$ is the *clover* term

$$\begin{aligned} Q_{\mu\nu}(x) =& U_\mu(x)U_\nu(x+a\hat{\mu})U^\dagger_\mu(x+a\hat{\nu})U^\dagger_\nu(x) \\ &+ U_\nu(x)U^\dagger_\mu(x-a\hat{\mu}+a\hat{\nu})U^\dagger_\nu(x-a\hat{\mu})U_\mu(x-a\hat{\mu}) \\ &+ U^\dagger_\mu(x-a\hat{\mu})U^\dagger_\nu(x-a\hat{\mu}-a\hat{\nu})U_\mu(x-a\hat{\mu}-a\hat{\nu})U_\nu(x-a\hat{\nu}) \\ &+ U^\dagger_\nu(x-a\hat{\nu})U_\mu(x-a\hat{\nu})U_\mu(x+a\hat{\mu}-a\hat{\nu})U^\dagger_\mu(x)\,. \end{aligned} \tag{6.3}$$

The topological charge density $q_L(x)$ defined in this way requires a multiplicative renormalization factor Z_q, which takes values largely different from 1 unless the short distance fluctuations are removed from the observable [106]. This issue becomes even more relevant when computing the topological susceptibility $\chi_L = \int d^4x \, \langle q_L(0) q_L(x)\rangle$. Notice that for this particular observable, one must deal with non-trivial contact terms as $x \to 0$. This can be understood from the fact that q is odd under time reversal, so due to reflection positivity $\langle q(0)q(x)\rangle < 0$ for $|x| > 0$ [107, 108]. On the other hand, χ is non-negative, so a positive contact term has to be added at $|x| = 0$ to cancel the negative contribution from the space-time integral.

In most of the large N computations of χ_{YM} on the lattice, the ultraviolet fluctuations are removed by cooling [109], which in simple terms replaces each link by

the one that minimizes the local action. A cooling step consists in a sweep of the full lattice, which is then iterated several times as the gauge configuration is driven towards a classical minimum of the action. This procedure removes the undesired ultraviolet fluctuations but does not provide a well defined strategy to take the continuum limit, and is motivated by the fact that in the continuum theory, continuous deformations of the gauge fields should not have an effect on the global topology.

6.1.2 The fermionic definition of the topological charge

In Sec. 3.1 we presented the connection between topology and the index of the Dirac operator through the Atiyah-Singer index theorem. Although all our simulations are in the pure gauge theory, we mention the definition of the topological susceptibility through Ginsparg-Wilson fermions for completeness, as it is theoretically solid and well grounded.

When dealing with a discretized version of fermions, one is inevitably led to the Nielsen-Ninomiya theorem [110], which in its relevant portion tells us that one must deal with a formulation which either produces unphysical fermion modes (doublers) or breaks chiral symmetry explicitly $\{\gamma_5, D\} \neq 0$, where D is the Dirac operator in the lattice. An elegant way around this problem was proposed by Ginsparg and Wilson in 1982 [111], where they propose to use a discretization of the Dirac operator such that[1]

$$\{\gamma_5, D\} = aD\gamma_5 D\,, \tag{6.4}$$

which reproduces the right relation in the continuum. A solution for D was first described in Ref. [112], which is known as the overlap operator, and can be written in terms of the Wilson Dirac operator D_W as

$$D = 1 + \gamma_5 \frac{H}{\sqrt{H^2}}\,, \quad H = \gamma_5 D_W\,. \tag{6.5}$$

An interesting property of the overlap operator is the fact that it leads to a non-standard realization of chiral symmetry on the lattice [113]

$$\delta\Psi(x) = \gamma_5 \left(1 - \frac{1}{2}aD\right)\Psi(x)\,, \qquad \delta\bar{\Psi}(x) = \bar{\Psi}(x)\left(1 - \frac{1}{2}aD\right)\gamma_5\,, \tag{6.6}$$

and in fact, when looking at the transformation properties of the integral measure $\delta\left[d\bar{\Psi}d\Psi\right] = 2N_{\mathrm{f}}Q\left[d\bar{\Psi}d\Psi\right]$, it produces the correct chiral anomaly.

[1] Actually, the original condition reads $\gamma_5 D + D\gamma_5 = aD2R\gamma_5 D$, where R is a local operator, but for simplicity we have decided to present directly the condition obtained from Neuberger's construction [112].

With this formulation, one can define both the topological charge and the topological charge density

$$q_{GW}(x) = \frac{a}{2}\,\mathrm{Tr}\left(\gamma_5 D(x,x)\right)\,, \qquad Q_{GW} = \frac{a}{2}\,\widetilde{\mathrm{Tr}}\left(\gamma_5 D\right)\,, \tag{6.7}$$

where $\widetilde{\mathrm{Tr}}$ runs over spin, colour and lattice indices, while Tr is taken over spinor and colour indices only. Once D has been defined, Eq. (6.7) provides an unambiguous definition of the topological charge in the lattice, and by construction Q is an integer given by the index of the Dirac operator. Although computations of the topological susceptibility using this formalism are theoretically solid and have been performed up to very high accuracy in the literature [114], they are very costly, specially because of the inverse square root that has to be computed in Eq. (6.5).

6.1.3 The gradient flow definition

As mentioned in Sec. 4.3, the flow provides a smoothing of the gauge fields, so that at positive flow time, the topological susceptibility

$$\chi^t = \int d^4x \left\langle q^t(x) q^t(0)\right\rangle\,, \tag{6.8}$$

does not suffer from short distance singularities and it is in fact independent of t in the continuum. Remarkably, this implies that one can use the naive discretization of the field strength tensor as in Eqs. (6.1), (6.2) at positive flow time t to obtain a quantity whose continuum limit coincides with the definition using GW fermions, which satisfies the chiral Ward identities when fermions are included.

As discussed in Ref. [97], one can show that

$$\lim_{a\to 0} a^4 \sum_x \left\langle q^t_{GW}(x) q^t_{\mathrm{GW}}(0)\right\rangle = \lim_{a\to 0} a^4 \sum_x \left\langle q^{t=0}_{\mathrm{GW}}(x) q^{t=0}_{\mathrm{GW}}(0)\right\rangle\,, \tag{6.9}$$

where q^t_{GW} is the Ginsparg-Wilson topological density computed from the gauge links V^t at positive flow time. This means that the continuum limit of the GW definition of χ_{GW} at positive flow time is the same as that of χ_{GW} at $t = 0$; the latter satisfying the chiral Ward identities. Then, consider the gluonic definition of $q(x)$ at positive flow time in the lattice $q^t_L(x)$, and notice that it shares the same asymptotic behaviour in the classical continuum limit as q^t_{GW} [115]. This implies that χ^t_{YM} computed through the naive discretization of the field strength tensor has the same continuum limit as χ^t_{GW}, which according to Eq. (6.9) is equivalent to the one of the standard definition using GW fermions at $t = 0$. In this sense, the gradient flow provides a theoretically sound definition of χ_{YM}, and by using the gluonic definition, it can be readily computed in the pure Yang-Mills gauge theory.

Open boundary conditions

The definition in Eq. (6.8) is usually re-written in the lattice with periodic boundary conditions as

$$\chi^t_{\rm YM} = \frac{\langle Q^2 \rangle}{V} \,. \tag{6.10}$$

In the case of OBC, we cannot do the same, as translation invariance is lost in the time direction. Instead, we define $q^t(\vec{x}, x_0)$ as in Eq. (6.1) using the clover discretization of the field strength tensor, and then define the topological susceptibility as in Eq. (5.29). Let us write down that formula in a more transparent way as

$$\chi^t_{\rm YM}(r_{\rm cut}) = \bar{P}^t(0) + 2a \sum_{r=a}^{r_{\rm cut}} \bar{P}^t(r) \,, \tag{6.11}$$

where

$$\bar{P}^t(r) = \frac{a}{(T-2d-r)L^3} \sum_{x_0=d}^{T-a-d-r} \left\langle \bar{q}^t(x_0) \bar{q}^t(x_0+r) \right\rangle \qquad \bar{q}^t(x_0) = a^3 \sum_{\vec{x}} q(x_0, \vec{x}) \,, \tag{6.12}$$

and d is the distance from the open boundaries which is determined as explained in Sec. 4.4.1. Rigorously, one needs to find a correct value of d at each value of r, but in practice we find that the stronger bound, i.e. the largest d, is dictated by the case $r = 0$, so we use that value of d for all values of r.

6.2 Simulations

The simulations used for the computation of the large N limit of $\chi_{\rm YM}$ were performed at the ZIB computer centre with resources granted by the North-German supercomputing alliance (HLRN), on PAX at DESY Zeuthen and through a collaboration, at Fermi and Galileo at CINECA and on Wilson at Milano-Bicocca. All the ensembles were specifically generated for this project by the authors in Ref. [89]. In all cases, the configurations were generated with the hybrid over-relaxation algorithm, with a ratio of over-relaxation sweeps to heatbath sweeps equal to $N_{\rm or}$. We define an update to be a combination of $N_{\rm or}$ overrelaxation sweeps followed by one heatbath sweep. Whenever we quote values for autocorrelations, or spacing between measurements, we do it in units of updates. Roughly 70% of the configurations were generated using the openSUN code described in Appendix A.

For the large N and continuum limit extrapolations we used 9 ensembles, 3 for each gauge group ($N = 4, 5, 6$). Additionally, for finite volume checks we used 5 additional ensembles. For each ensemble we measure the value of t_0/a^2 and then use the value of $\sqrt{t_0} = 0.166\,\text{fm}$ to express the lattice sizes and the lattice spacing in

#run	N	β	$N_{\rm or}$	T/a	L/a	a[fm]	$N_{\rm meas}$	$N_{\rm upd}$
$A(4)_1$	4	10.92	8	64	16	0.096	22k	40
$A(4)_2$	4	11.14	10	80	20	0.078	41k	80
$A(4)_3$	4	11.35	12	96	24	0.065	21k	160
$A(5)_1$	5	17.32	8	64	16	0.095	15k	120
$A(5)_2$	5	17.67	10	80	20	0.077	27k	240
$A(5)_3$	5	18.01	12	96	24	0.064	14k	480
$A(6)_1$	6	25.15	8	64	16	0.095	30k	250
$A(6)_2$	6	25.68	10	80	20	0.076	17k	500
$A(6)_3$	6	26.15	12	96	24	0.063	16k	450
$B(4)_1$	4	10.92	6	12	64	0.096	5k	40
$D(4)_1$	4	10.92	12	24	96	0.096	10k	45
$B(5)_1$	5	17.32	6	12	64	0.095	7k	120
$C(5)_1$	5	17.32	10	20	80	0.095	5k	120
$D(5)_1$	5	17.32	12	24	96	0.095	7k	180

Table 6.1: Parameters of the simulation. For each of the three gauge groups SU(N) we give the inverse lattice coupling β, the ratio of overrelaxations per heatbath $N_{\rm or}$, the dimensions of the lattice, the approximate lattice spacing using $\sqrt{t_0} = 0.166\,$fm followed by the number $N_{\rm meas}$ of measurements and their separation in units of updates $N_{\rm upd}$ of the lattice.

physical units. Clearly, for $N \neq 3$, we do not have a physical world to fix the scale, so whatever choice we make is somewhat artificial. In our case the physical value of t_0 was motivated by the SU(3) result $\sqrt{8t_0}/r_0 = 0.941(7)$ [97] and the convenient choice for the Sommer scale $r_0 = 0.5\,$fm [116]. The size of the boxes has been chosen such that $L \approx 1.5\,$fm, which is a safe choice in terms of finite size effects as we show in Sec. 6.3.2. The main parameters of the simulations are shown in Table 6.1.

The β values were tuned from preliminary runs as shown in Appendix C, and chosen so to approximately match the values of t_0/a^2 on the different N ensembles. We also performed two extra simulations at the coarsest lattice spacing in SU(5) with $L/a = 16$ and $T = 2L, 3L$. At lower than target statistics (approximately 8000 measurements), we compared the relative cost to obtain the same target error from simulations at the different values of T/L, using the definition in Eq. (6.11). At two different values of $r_{\rm cut} = 5\sqrt{t_0}$ and $r_{\rm cut} = 10\sqrt{t_0}$ the ratio of the cost $[T = 2L : T = 3L : T = 4L]$ obtained was $[1.10 : 1 : 1.06]$ and [N.A : 1 : 1.03] respectively. For the case of $r_{\rm cut} = 10\sqrt{t_0}$ we do not have data at $T = 2L$ as the plateau region is not large enough to measure it. From these results, it is clear that the extra effort of simulating a larger lattice is compensated by the statistical gains in the computation of $\chi^t_{\rm YM}(r_{\rm cut})$ from averaging over a longer plateau region, so the production runs in Table 6.1 were all performed at $T = 4L$.

The observables are defined using the standard Wilson discretization for the gradient flow. The integration of the flow equations is performed using a third order Runge-Kutta integrator as described in Ref. [78], with a step size $\epsilon = 0.02a^2$, and are saved with a resolution of $0.04a^2$ in the flow time t. In order to interpolate to any given value of t/a^2 we use a quadratic polynomial, although with the resolution of the data, a linear interpolation gives consistent results. For the dimensionless quantity $t^2\chi^t_{\mathrm{YM}}|_{t=t_0}$, the errors in the interpolation have been propagated to the final observable using the UWerr routine described in Ref. [66].

6.3 Analysis

In this section we describe how we deal with the systematics involved in the computation of χ^t_{YM} for the ensembles in Table 6.1. The results are presented at $t = t_0$ unless stated otherwise. The distance d from the boundary has been chosen as described in Sec. 4.4.1, so we simply quote the result here. For $\bar{e}^{t_0}$ and $\bar{P}^{t_0}$ we find a good choice to be $d = 9.5\sqrt{t_0}$ and $d = 7.5\sqrt{t_0}$ respectively.

6.3.1 Signal to noise problem

When considering the definition in Eq. (6.11) one must make a choice concerning the parameter r_{cut} which marks the limit in the summation of the topological charge density correlator. In principle, one could sum up to the maximum distance allowed by the size of the plateau, but in practice this produces undesired effects in the error. As discussed in Ref. [94], one possible way is to model the large distance behaviour of the tail of the correlator with a phenomenological model which takes into account the exponential behaviour of the correlator. While this reduces the statistical error, it adds a systematic effect in the calculation. In this sense, if the estimation of the tail is well below the statistical uncertainty, it was argued in Ref. [79] that a more convenient choice is to cut the sum at a sufficiently large value of r_{cut}. We follow the latter line of thought.

One way to choose r_{cut} is to estimate the contribution from the tail of the correlator by fitting an exponential to the mass of the lightest pseudo scalar particle of the theory [79]. In our case, when dealing with the pure gauge theory, the large mass of approximately 2.6 GeV [117] of the pseudoscalar glueball 0^{-+} makes it impossible to identify the exponential decay of the correlator.

As we have mentioned, $\langle q(0)q(r)\rangle$ is negative at $r > 0$ and gets a positive contribution from the contact term at $x = 0$. Due to the smoothing at positive flow time, the correlation function is positive for small r and only becomes negative for $r \gtrsim \sqrt{8t}$. At small values of t this is noticeable, but at $t = t_0$, the smoothing of the flow hides this behaviour (see Figure 5.7). In Figure 6.1 we show the r_{cut} dependence of χ_{YM}, where it becomes clear that the signal receives no contribution from

the long tail of the correlator, and summing up more time slices simply increases the error. The red vertical line shows the value at which we cut the sum following the procedure described in the following.

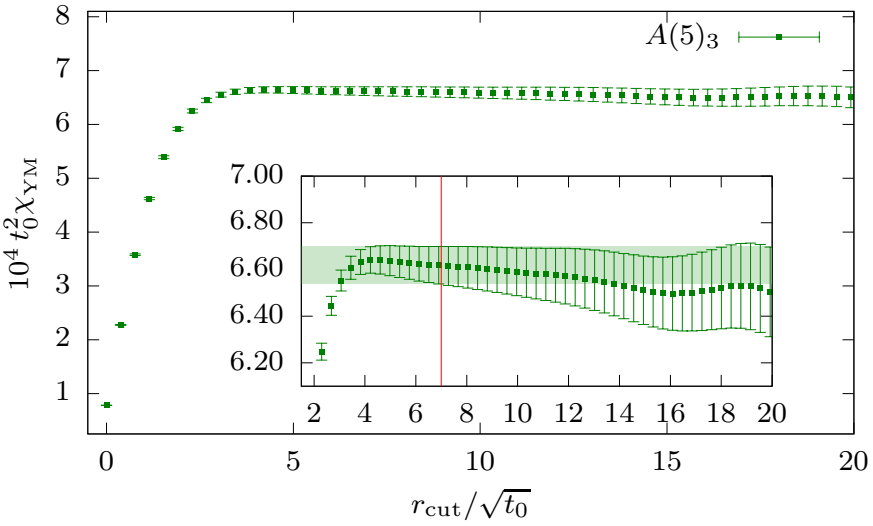

Figure 6.1: Plot of the $r_{\rm cut}$ dependence of $\chi_{\rm YM}$ for the ensemble $A(5)_3$. The band shows the value of $\chi_{\rm YM}$ if the sum is stopped at $r_{\rm cut} = 7.0\sqrt{t_0}$.

Our strategy is to use the algorithm introduced in Chapter 5. Ideally we would like to apply it to all the ensembles in order to have a good estimation of the correlation function at large values of r. However, most of the ensembles in Table 6.1 were already generated by the time our multilevel algorithm was formulated. Our strategy was then to use an SU(3) ensemble with the same parameters as in Table 5.1, generated with the multilevel updates as described in the previous chapter and with a total of $n_0 \times n_1 = 184 \times 280 = 201600$ measurements. Notice that this represents an order of magnitude larger than the ones used for our SU(N) study, and has the added advantage of the faster error scaling from the use of the multilevel algorithm. We compare it to an ensemble with the same parameters but with $n_0 = 15600$ measurements and no multilevel type updates, which is equivalent in statistics to the ensembles in Table 6.1.

Figure 6.2 shows a comparison of the correlator as a function of r. The red open points are computed using the standard algorithm while the black filled points correspond to the improved algorithm. Our strategy is to use this data to determine the right value of $r_{\rm cut}$. In order to do that, we first define

$$\chi^{\rm imp}_{\rm YM,tail}(r) = 2 \sum_{\Delta=r+1}^{\Delta_{max}} \bar{P}(\Delta)\,, \tag{6.13}$$

as the sum of the contributions to $\chi^t_{\rm YM}$ from values of $\Delta > r$. Δ_{max} is the maximum distance up to which the correlator can be summed up in our finite size lattice, i.e. $T - 2d$. The superscript "imp" has been written to explicitly show that it is to be computed with the high precision data from the improved multilevel algorithm.

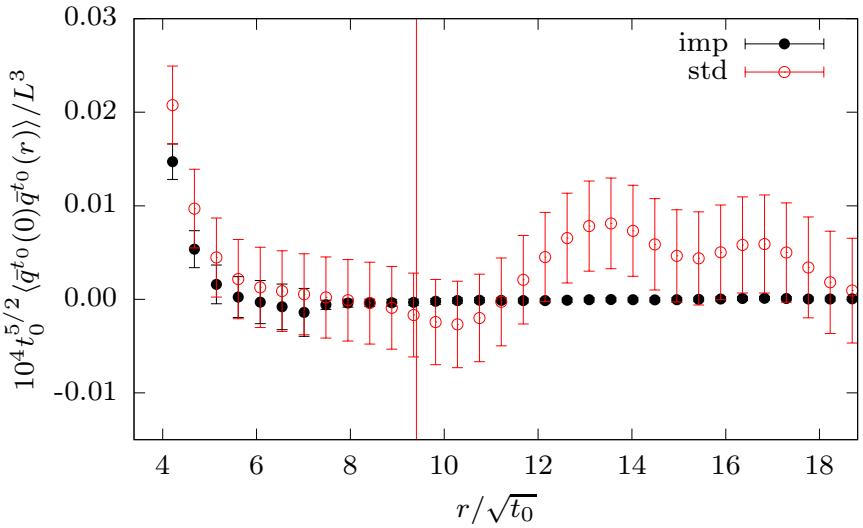

Figure 6.2: Plot of $\langle \bar{q}(0) q(\bar{r}) \rangle$. The red points correspond to data computed using the standard algorithm and around 15k measurements, while the black points correspond to the observable computed using the multilevel algorithm and $n_0 \times n_1 \approx 200$k measurements. Notice that the real advantage of the multilevel is only visible at $r/\sqrt{t_0} > 7.0$. Figure from Ref. [98].

We then look at the condition

$$F(N)\chi^{\rm imp}_{\rm YM,tail}(r)|_{r=r_{\rm cut}} < 0.25\,\sigma^{\rm std,SU(N)}(r)|_{r=r_{\rm cut}}, \qquad F(N) = \frac{\chi^{\rm std,SU(N)}(r)}{\chi^{\rm std,SU(3)}(r)}, \quad (6.14)$$

where $\sigma^{\rm std,SU(N)}$ is the statistical error computed for $\chi_{\rm YM}$ for each of the SU(N) ensembles, and $\chi^{\rm std,SU(N)}$ is also computed using the standard algorithm. The strategy is basically to attach the tail determined from the multilevel algorithm in SU(3) to the SU(N) ensembles in Table 6.1 and compare it to the statistical error. The factor $F(N)$ is used to account for N dependence of the observable, but in practice, for r such that the condition in Eq. (6.14) is satisfied, the result does not depend on $F(N)$.

As long as the error in the estimation of the tail itself is small compared to σ, imposing Eq. (6.14) guarantees a small systematic error compared to the statistical one. In fact, the values of $r_{\rm cut}$ obtained for the SU(N) ensembles are all below $6\sqrt{t_0}$. However, as can be seen in Figure 6.2, for $r/\sqrt{t_0} < 7.0$, we are still in the region where

the multilevel updates do not yet yield the maximum theoretical improvement, and the errors are only a factor 2 smaller than those of the standard algorithm. Because of this, only when $r/\sqrt{t_0} \geq 7.0$, we consider the criterion to be significant. Past this point, the errors rapidly become of $\mathrm{O}(10^{-1})$ smaller than those of the standard algorithm. Considering this, $r_{\mathrm{cut}} = 7.0\sqrt{t_0}$ is a safe choice as it satisfies Eq. (6.14) and is evaluated up to a very high precision compared to the standard correlator.

6.3.2 Finite volume checks

Notice that the A ensembles in Table 6.1 are of a physical size of approximately 1.5 fm, so they are larger than those reported in Ref. [97], where the authors have an order of magnitude more statistics than in our case, and even there, no sizeable finite size effects are observed. In order to not only rely on SU(3) data, we simulate lattices of spatial dimension ranging from $L \approx 1.1\,\mathrm{fm}$, up to $L \approx 2.3\,\mathrm{fm}$ (ensembles B and C in Table 6.1) at the coarsest lattice spacing. Our results are shown in Table 6.2 and in Figure 6.3. Compared to the values computed in the largest lattices at $L/a = 24$, the data at $L/a = 16$ is consistent with an statistical fluctuation and we observe no systematic trend even at the smallest lattices.

#run	$B(4)_1$	$A(4)_1$	$D(4)_1$	$B(5)_1$	$A(5)_1$	$C(5)_1$	$D(5)_1$
$10^4 t_0^2 \chi_{\mathrm{YM}}$	6.26(11)	6.61(6)	6.45(7)	6.50(13)	6.47(7)	6.30(13)	6.47(7)

Table 6.2: Check of finite volume effects. We compare the results at various values of L/a (see Table 6.1).

6.3.3 Autocorrelations

Previous determinations of the large N limit of χ_{YM} have been restricted to smaller values of β [118, 77] due to the large values of autocorrelations. Although we did not perform a detailed comparison between PBC and OBC, the values for the autocorrelations reported in Ref. [89] show that already at the coarsest lattice spacings there is an improvement using OBC compared to PBC. Moreover, when monitoring the history of the topological charge

$$Q_{\mathrm{OBC}} = a^4 \sum_{x_0=d}^{T-a-d} \sum_{\vec{x}} q(\vec{x}, x_0)\,, \tag{6.15}$$

we observe no signs of topology freezing (see Figure 6.4).

In units of measurements, τ_{int} for χ_{YM} in the A ensembles from Table 6.1 is around 1, except for $A(6)_3$ where $\tau_{\mathrm{int}} \approx 0.6$. Such small values are not ideal for a precise determination of τ_{int}, but nonetheless we make use of these results to have an

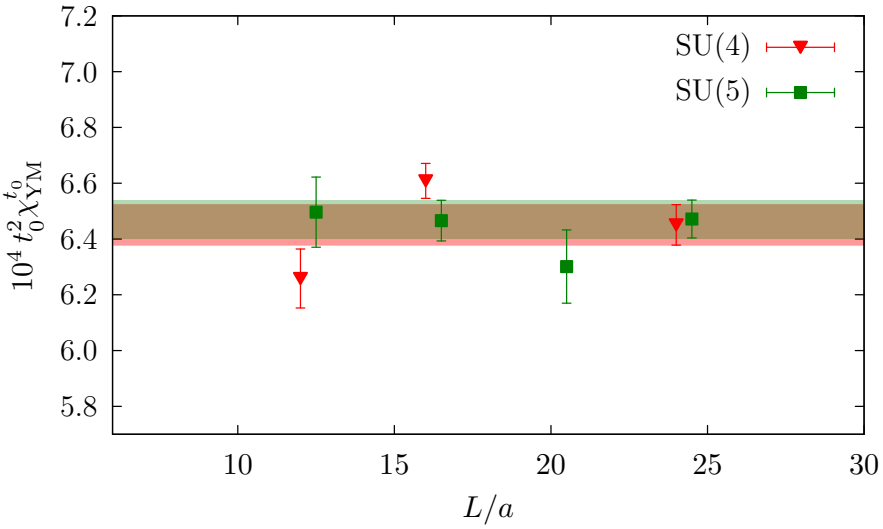

Figure 6.3: Plot of $t_0^2 \chi_{\rm YM}^{t_0}$ as a function of L/a, the data corresponds to the one reported in Table 6.2. The bands show the value at the largest lattices $L/a = 24$ and have been added to better display the absence of significant statistical deviations.

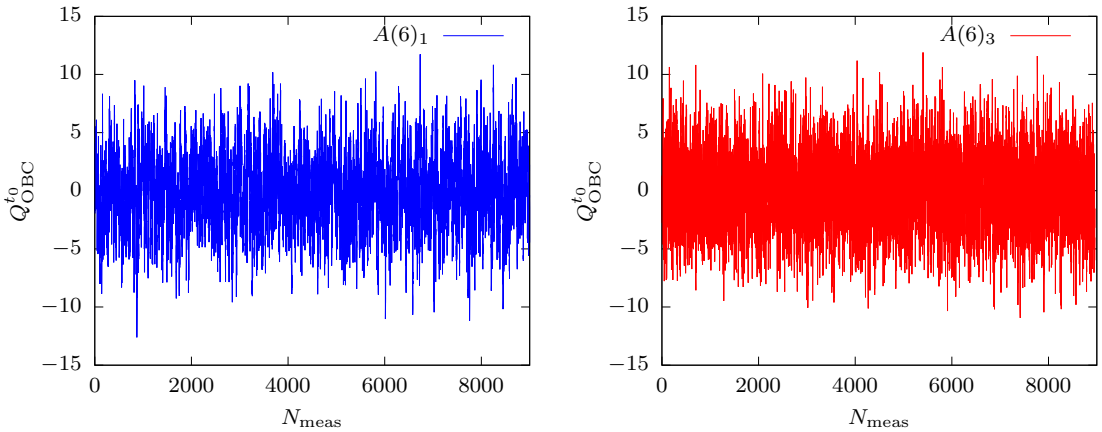

Figure 6.4: History of the topological charge for the coarsest and finest SU(6) ensembles.

exploratory understanding of the scaling of autocorrelations[2]. The measured values are presented in Table 6.3 in units of updates. In Figure 6.5 we plot the results together with a linear fit to t_0/a^2. Only in the case of SU(6) we obtain a good value of $\chi^2/\text{dof} = 1.1$ while in the case of SU(4) and SU(5) the results are 6.8 and 3.9 respectively. Clearly more data is needed in order to have any conclusion regarding the N and a dependence of the autocorrelations. However, we do not observe a behaviour as severe as the one reported in Ref. [77]. The advantages of OBC have also been studied in Ref. [119], where the authors find that small instantons concentrate near the open boundaries. When looking at the integrated autocorrelation time of the timeslice summed topological charge density, our data shows that it grows linearly from the boundaries and reaches a plateau value, which is consistent with the one obtained with PBC in the bulk.

$A(4)_1$	$A(4)_2$	$A(4)_3$	$A(5)_1$	$A(5)_2$	$A(5)_3$	$A(6)_1$	$A(6)_2$	$A(6)_3$
15(1)	44(2)	102(7)	58(4)	170(10)	256(20)	112(6)	266(19)	402(24)

Table 6.3: Values of $R\tau_{\text{int}}\left(\chi_{\text{YM}}\right)$ for the SU(N) ensembles used in this study. For an explanation of the normalization factor R, see Appendix A.

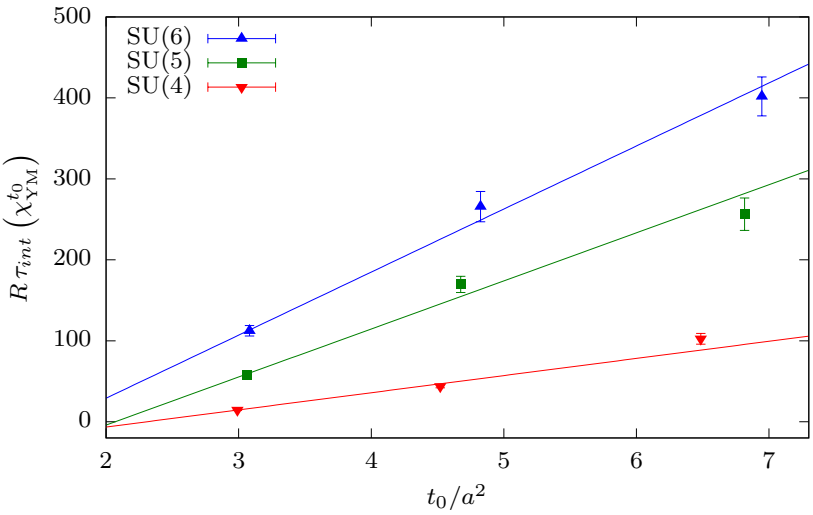

Figure 6.5: Plot of $R\tau_{\text{int}}$ as a function of t_0/a^2 for the data in Table 6.3.

[2]Dedicated runs should be performed to properly study the scaling of τ_{int}. In our case, the cost would not be justified.

6.4 Results

Using the strategy described before, we computed $t_0^2\chi_{\rm YM}$ for the nine ensembles to be used for the large N and continuum extrapolations. The results are presented in Table 6.4. We use them to extrapolate to the continuum and large N limits. Let us first discuss our results concerning the reference scale t_0 defined in Eq. (4.31).

ensemble	t_0/a^2	$10^4\, t_0^2\chi_{\rm YM}$	$t_0^{1/2}\chi_{\rm YM}^{1/4}$
$A(4)_1$	2.9900(7)	6.61(6)	0.1603(5)
$A(4)_2$	4.5207(8)	6.54(6)	0.1599(3)
$A(4)_3$	6.4849(16)	6.68(7)	0.1607(4)
$A(5)_1$	3.0636(7)	6.47(7)	0.1595(5)
$A(5)_2$	4.6751(8)	6.73(7)	0.1611(4)
$A(5)_3$	6.8151(17)	6.62(8)	0.1604(5)
$A(6)_1$	3.0824(4)	6.57(6)	0.1601(4)
$A(6)_2$	4.8239(9)	6.81(8)	0.1615(5)
$A(6)_3$	6.9463(13)	6.80(7)	0.1615(4)

Table 6.4: Results for t_0, $t_0^2\chi_{\rm YM}$ and its fourth root. As presented in Ref. [89].

6.4.1 The reference scale t_0

As shown in Table 6.4, our results for t_0/a^2 are measured in a below per-mille level, so this presents an excellent scenario to check for N scaling. In the left panel of Figure 6.6 we plot the quantity $\frac{N}{N^2-1}\left\langle t^2e^t\right\rangle$ as a function of t/t_0 for $N = 4$, 5, 6 at the finest and coarsest lattice spacings. In the range of t considered, one cannot distinguish any significant difference between the results for the different gauge groups. Comparing the data at different lattice spacings however, does reflect a difference which is clearly visible at small t, which shows that the cut-off effects are much more important in that region.

Going back to the N dependence, in order to have a quantitative assessment, we define the scale t_c as

$$\left\langle t^2e^t\right\rangle|_{t=t_c} = c\left(\frac{N^2-1}{N}\right), \tag{6.16}$$

where c is a numerical constant.

The choice of c is rather arbitrary as we use it only to compare the values of t_0/t_c for the different gauge groups. We find the choice $c = 0.08$ to be a reasonable one, considering that by using such value, $\left\langle t^2e^t\right\rangle$ is still in the region where it grows

linearly in t [78]. The observable t_0/t_c can be computed up to very high accuracy and the errors are $O(10^{-4})$. We plot this quantity as a function of $1/N^2$ in the right panel of Figure 6.6, and we find an excellent fit to a linear function with values of $\chi^2/\text{dof} = 0.35$, 2.18, and 1.30 at the three lattice spacings considered in this study. In addition, we take the continuum limit for each gauge group by fitting the data to a linear function in a^2/t_0. The fits produce values of $\chi^2/\text{dof} = 0.84$, 0.55 and 3.41 for SU(4), SU(5) and SU(6) respectively. We then use the continuum extrapolations to take the large N limit of t_0/t_c and obtain a value of 1.29802(19) with $\chi^2/\text{dof} = 0.96$. Due to the very small errors in this observable, our results constitute an excellent verification of the 't Hooft scaling. Moreover, up to SU(4), the results are perfectly compatible with $O(1/N^2)$ corrections.

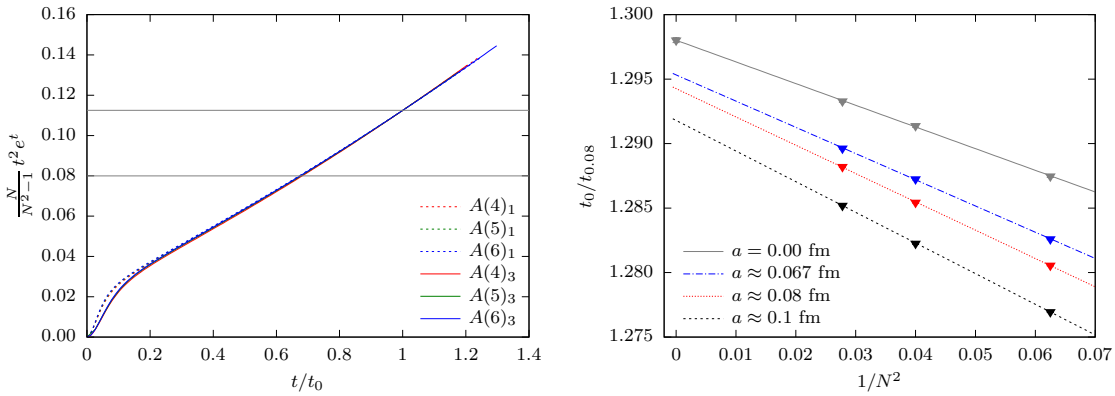

Figure 6.6: *Left:* Plot of $\frac{N}{N^2-1}\left\langle t^2e^t\right\rangle$ as a function of t/t_0 for the finest and coarsest ensembles in Table 6.1. The N dependence is barely visible as the curves overlap. The horizontal lines indicate the values at which we define t_0 and $t_{0.08}$ respectively. *Right:* Plot of $t_0/t_{0.08}$ as a function of $1/N^2$ at three different lattice spacings and in the continuum. We observe an excellent agreement with a $1/N^2$ scaling.

6.4.2 The topological susceptibility

For the computation of the topological susceptibility we use the data from Table 6.4, and additionally we use the SU(3) results at the three finest lattice spacings from Ref. [97].

In order to assess the systematics from the extrapolations we tried different fit functions varying the number of points used for the fit. We considered the following fit functions

- $F_L(1/N) = c_0 + c_1\frac{1}{N^2}$,
- $F_{G_1}(1/N, a) = d_0 + d_1\frac{1}{N^2} + d_2\frac{a^2}{t_0}$,

- $F_{G_2}(1/N, a) = e_0 + e_1 \frac{1}{N^2} + e_2 \frac{a^2}{t_0} + e_3 \frac{a^2}{t_0 N^2}$,

where the constant parameter corresponds to the value of $t_0^2 \chi_{\text{YM}}$ in the continuum and large N limits.

With them, we try different strategies: the simplest one, LF3, is to perform the continuum limit fits group by group and later use F_L to obtain the large N limit. Another option is to perform a global fit using either F_{G_1} or F_{G_2}. Depending on the points used for the global fit we use the following notation, GF3 when using all three points for $N \geq 3$ and F_{G_1}, or GFF3 when using F_{G_2} for the fit. When disregarding the coarsest points for $N \geq 4$ and using F_{G_1} we denote the fit by GF2. If only the two finest points for all $N \geq 3$ groups are fitted with F_{G_1} we call it GF22. An advantage of using this last strategy is that we limit the assumption on the region of validity of the leading order Symanzik expansion (we do not use the coarsest points to extract the final result). Similarly, we can constrain the systematics from the large N extrapolation using F_{G_1} by excluding the SU(3) points from the determination of d_0 and d_1, and only using them to fit the coefficient d_2. In this case, we denote the fits by NGF3 when we use all three points for all gauge groups, and NGF22 or NGF2 depending whether 2 or 3 points for $N = 3$ are used, together with two points for $N \geq 4$.

The results from these fits are shown in Table 6.5. Clearly all the results are compatible as can be seen also in Figure 6.8. We also looked at the ratio $\chi^t_{\text{YM}}/\chi^{t_0}_{\text{YM}}$ as it can be captured with very high accuracy, and plot it in Figure 6.7. From this quantity, we observe no N dependence on the cut-off effects, which also points to the compatibility of the large N extrapolation using either F_{G_1} of F_{G_2}. In the end, to balance systematic and statistical uncertainties, we quote for the final value the one obtained from the fit strategy NGF22. This constrains both the validity of the leading order Symmanzik expansion, as well as the large N expansion, which results on a larger statistical error as compared to NGF3 or GF3 for example.

	$10^4\, t_0^2 \chi^t(0,0)$	χ^2/dof
LF3	7.02(13)	1.37
GF3	7.06(7)	1.55
GFF3	7.02(13)	1.72
GF2	7.09(7)	1.00
GF22	6.98(11)	0.90
NGF2	7.13(10)	1.13
NGF3	7.01(9)	1.63
NGF22	7.03(13)	0.94

Table 6.5: Summary of continuum and large N limit fit results including the values of χ^2/dof.

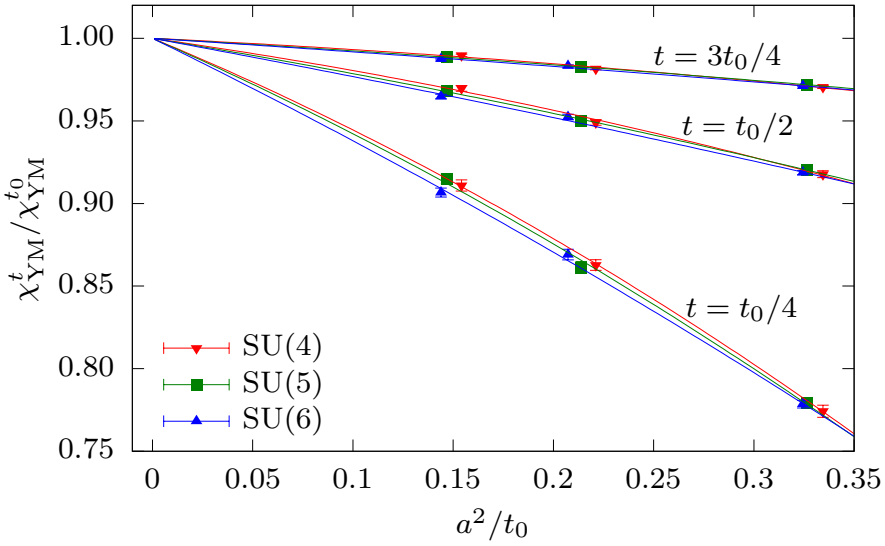

Figure 6.7: Plot of $\chi^t_{\rm YM}/\chi^{t_0}_{\rm YM}$ as a function of a^2/t_0. Even at this high precision we do not observable a significant difference in cut-off effects for different SU(N) groups. Figure from Ref. [98].

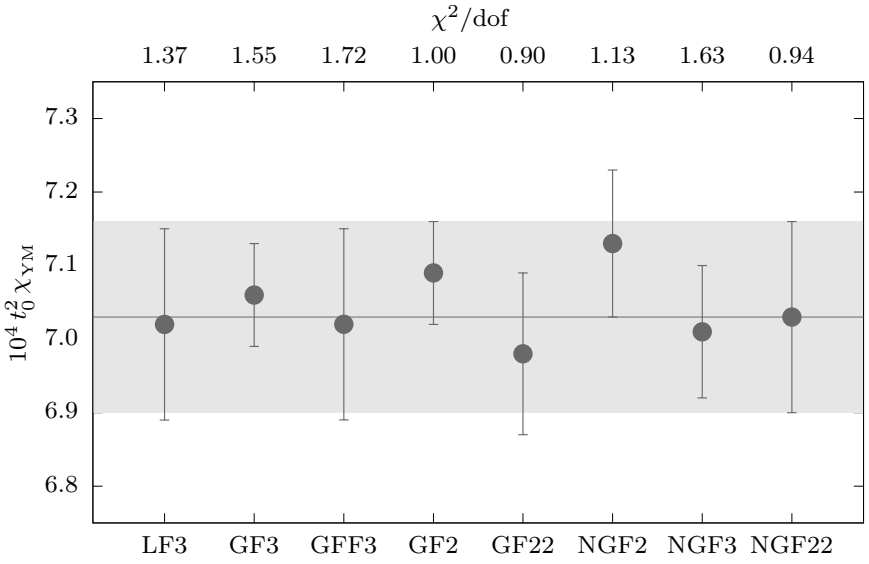

Figure 6.8: Summary of the results for several fits employed. The band shows the result from NGF22, which is clearly compatible with the rest of fits performed.

The final result we quote in the large N and continuum limit is then given by $t_0^2\chi_{\rm YM} = 7.03(13)\times 10^{-4}$. This accounts for a 2% error, which undoubtedly represents a new quality in the verification of Witten-Veneziano relation. The rest of parameters from the fit are $d_1 = -6(2)\times 10^{-4}$ and $d_2 = -0.5(6)\times 10^{-4}$. From here, we obtain $t_0^2\chi_{\rm YM} = 6.68(12)\times 10^{-4}$, $t_0^2\chi_{\rm YM} = 6.81(11)\times 10^{-4}$, and $t_0^2\chi_{\rm YM} = 6.87(11)\times 10^{-4}$ for the continuum limits of the SU(N) gauge theories with $N = 4, 5, 6$ respectively. The results from Table 6.4 and the fit NGF22 are shown in the left panel of Figure 6.9, while on the right panel we show the continuum limit values as a function of $1/N^2$. In the case of SU(3) we include in the plot the continuum limit value from Ref. [97].

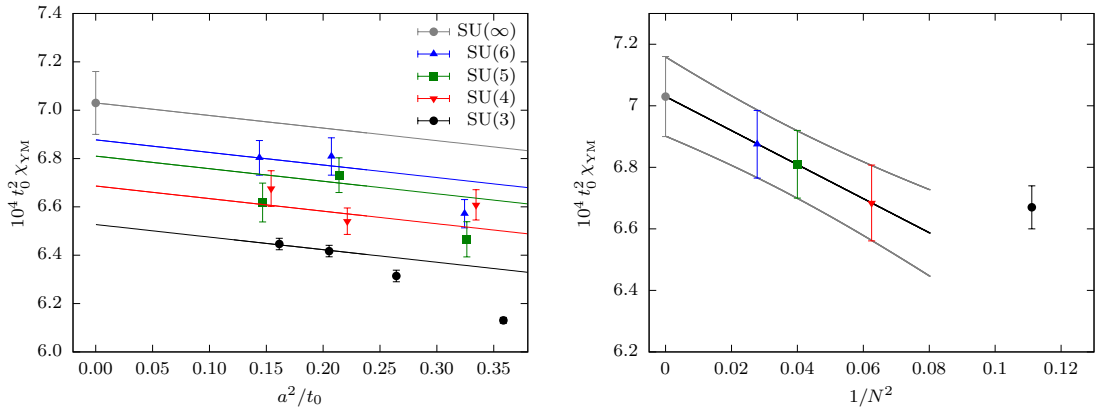

Figure 6.9: *Left*: results for the ensembles in Table 6.4 and the large N and continuum extrapolation using the global fit strategy NGF22. The SU(3) results are taken from Ref. [97]. *Right*: the continuum limit values from the left panel are presented as a function of $1/N^2$.

7. Factorization in the large N limit

In this chapter we look into the property of factorization discussed in Sec. 2.2. The observables that we use are Wilson loops, which in four dimensional space-time are defined as

$$W_C = \mathrm{Tr}\, P \left\{ \exp\left(i \oint_C A_\mu(x)\, dx^\mu \right) \right\} , \tag{7.1}$$

where C is a closed curve in space-time, and P denotes the path ordering operator. Including the trace operator Tr in the definition of W makes this observable gauge invariant[1]. Our goal is to verify Eq. (2.7), which applied to the Wilson loop operator means that

$$\langle W_{C_1} \dots W_{C_k} \rangle = \langle W_{C_1} \rangle \dots \langle W_{C_k} \rangle + \mathrm{O}(1/N^2) \,. \tag{7.2}$$

In order to take the continuum limit of Eq. (7.2), the loops must be properly renormalized. In perturbation theory, the exponential in Eq. (7.1) can be expanded to study the divergences of the Wilson loop. For smooth non-intersecting loops without cusps in 4d, the authors in Ref. [120] showed that besides logarithmic divergences which can be removed by the gauge coupling renormalization, there is an additional linearly divergent term proportional to the length of the path C, and is thus referred as the "perimeter divergence". The renormalization of this term can be interpreted as a mass renormalization of a heavy test quark related to the static quark potential [120]. In the case of a loop with cusps, or "corners", there are additional logarithmic divergences which depend on the angle λ of the cusp [120, 121, 122]. The existence of the perimeter and corner divergences, makes taking the continuum limit of the Wilson loops a non-trivial task.

Using the Wilson flow, the smoothed Wilson loop observables defined at positive flow time [81] are free from the perimeter and corner divergences. This is explicitly shown in Ref. [123] by doing a perturbative expansion of the loops at positive flow time t. Such favourable properties of the smooth Wilson loops have been used in the literature to extract the string tension [124, 123], as well as to study the large N phase transition in the eigenvalue spectrum of the Wilson loop matrices [125]. In

[1] Notice that it is not uncommon in the literature to define W without Tr.

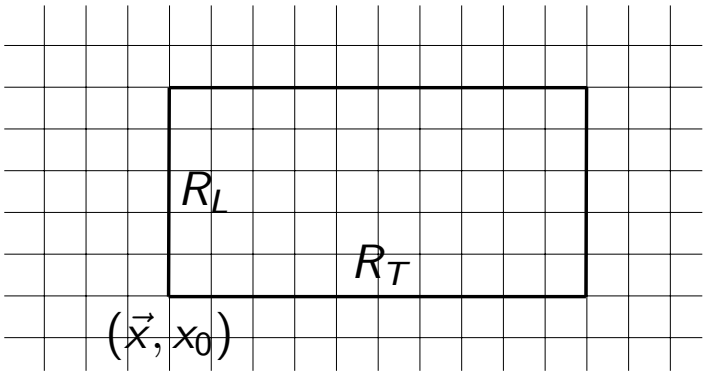

Figure 7.1: Graphical representation of a rectangular Wilson loop $W(\vec{x}, x_0, R_L, R_T)$ on the lattice.

particular, when extracting the string tension, the smooth Wilson loops have been computed at very small values of t.

For our purpose, the limit of small t is not required, as we use the smooth loops as a way to test factorization for well defined renormalizable observables, regardless of their connection to the un-smoothed operators. In the rest of this chapter, we describe our numerical results for factorization of smooth Wilson loop operators. As already discussed in Sec. 2.2, factorization plays a crucial role in the idea of volume reduction [16], which by itself is a promising advance in the goal of solving large N QCD.

7.1 Observables

The observables we consider are Wilson loops on the lattice. For a rectangular path of sizes $R_L \times R_T$, where R_L is in one of the spatial directions, while R_T is in the temporal direction, we define the Wilson loop observable as

$$W(\vec{x}, x_0, R_L, R_T) = \frac{1}{N} Re \text{ Tr } U(\vec{x}, x_0, R_L \times R_T) \ , \tag{7.3}$$

where the normalization is chosen with the objective to have a finite large N limit. An explicit representation of a Wilson loop is shown in Figure 7.1. In addition, we also measure $W^2(\vec{x}, x_0, R_L, R_T)$ given simply by taking the square of the right hand side of Eq. (7.3). The measurements are performed for values of R_L up to $L/2$, and similarly, for R_T up to $T/2$.

Our goal is to verify factorization, so after averaging W and W^2 over the space-time volume as discussed in the next section, we look at

$$G_W = \frac{\langle W^2 \rangle - \langle W \rangle^2}{\langle W \rangle^2} \,. \tag{7.4}$$

From factorization, we expect the numerator to go as $1/N^2$, while the denominator has a finite value after the normalization has been fixed as in Eq. (7.3), so

$$G_W \propto \frac{1}{N^2} \,. \tag{7.5}$$

The denominator has been chosen to give us a relative measure of "how fast" is the approach of $\langle W^2 \rangle - \langle W \rangle^2$ to its expected value of zero in the large N limit. Notice that from a practical point of view, the vanishing of G_W also implies that the variance of the Wilson loop goes to zero in the large N limit.

Our goal is to check the $1/N^2$ scaling at finite lattice spacing as well as in the continuum. For that, we use the Wilson loops smoothed with the Yang-Mills gradient flow. This produces properly renormalizable observables free from ultraviolet divergences. At finite flow time t, the loops W^t are defined just as in Eq. (7.3) but using the gauge links evolved with the flow.

The ensembles used in this chapter are listed in Table 7.1. All the simulations were performed at the ZIB computer centre in Berlin, with the resources granted by the HLRN (North-German supercomputing alliance). In several cases, the parameters are the same as those of the ensembles in Chapter 6. In those cases, we have used a subset of the configurations generated for the computation of the topological susceptibility[2]. It is worth noting that we have added ensembles at $a \approx 0.05\,\mathrm{fm}$ for $N < 6$, and we have included a point for SU(8).

7.2 Analysis

For the flow time t we choose three values given by $t_c = ct_0$, with $c = \{1/2, 1, 9/4\}$. The measurement of the Wilson loops is then performed at several values of t in the interval $[t_c - \delta, t_c + \delta]$, with a resolution of $\epsilon = 2 - 3 \times 10^{-2}$. The parameter $\delta/t_0 \approx 2 - 3\%$ when $c = 1$ and is scaled linearly for the other values of t_c. The loops are then averaged over the spatial directions and in the plateau region in the time direction

$$W^{ct_0}(R) = \frac{a^4}{(T - 2d)\, L^3} \sum_{x_0 = d}^{T-d-a} \sum_{\vec{x}} W^{ct_0}(\vec{x}, x_0, R, R) \,, \tag{7.6}$$

where d is chosen as described in Sec. 4.4. We perform the open boundary analysis for all loops of sizes $a \leq R \leq L/2$, but for simplicity we choose the largest value

[2]Notice that we did not save all the configurations used in Chapter 6, due to disk space constraints.

#run	N	β	N_{or}	T/a	L/a	a[fm]	N_{meas}	t_0/a^2
$A(3)_2$	3	6.11	12	80	20	0.078	320	4.5776(15)
$A(3)_3$	3	6.24	12	96	24	0.065	280	6.783(23)
$A(3)_4$	3	6.42	12	96	32	0.050	252	11.19(4)
$A(4)_1$	4	10.92	8	64	16	0.096	248	2.9900(7)
$A(4)_2$	4	11.14	10	80	20	0.078	300	4.5207(8)
$A(4)_3$	4	11.35	12	96	24	0.065	312	6.4849(16)
$A(4)_4$	4	11.65	16	96	32	0.050	320	11.55(3)
$A(5)_1$	5	17.32	8	64	16	0.095	320	3.0636(7)
$A(5)_2$	5	17.67	10	80	20	0.077	240	4.6751(8)
$A(5)_3$	5	18.01	12	96	24	0.064	248	6.8151(18)
$A(5)_4$	5	18.21	16	96	32	0.050	320	11.51(3)
$A(6)_1$	6	25.15	8	64	16	0.095	320	3.0824(4)
$A(6)_2$	6	25.68	10	80	20	0.076	264	4.8239(9)
$A(6)_3$	6	26.15	12	96	24	0.063	288	6.9463(13)
$A(8)_2$	4	32.54	10	20	80	0.076	320	4.782(5)

Table 7.1: Parameters of the simulation. For each of the gauge groups SU(N) we give the inverse lattice coupling β, the ratio of overrelaxations per heatbath N_{or}, the dimensions of the lattice, the approximate lattice spacing using $\sqrt{t_0} = 0.166\,\text{fm}$ followed by the number N_{meas} of measurements. In the last column we present the values of t_0/a^2, for the ensembles with parameters already presented in Table 6.4, we copy the results here for completeness.

of d to define W^{ct_0} in Eq. (7.6) for all R. We observe that the largest values of d are obtained for the smaller loops, as they can be measured with a higher precision. Moreover, when doing the same exercise for W^2, we find the values of d to coincide with those of W at a fixed value of c and R.

In order to perform the large N and continuum limits, the size of the loops at different N and t_0 is matched by making the choice $R_c = \sqrt{8ct_0}$ when $t = t_c$. This means that for all the ensembles we need to interpolate in R to reach the desired value of R_c. To assess the systematic error from the interpolation we fit the data to a polynomial in R for the variable[3] $\hat{\omega}(R) = -\log\left(W(R)\right)/R$. Note that being strict, we should write $\omega^t(R)$ to make the t dependence explicit, however, to simplify notation we choose to omit the t dependence and it should be assumed implicitly. For the polynomial fits we use two quadratic and two cubic functions, each having a different fitting range. For example, in the case of the quadratic fits,

[3]We also tested the possibility of fitting the variable $w(R) = -log\left(W(R)\right)$, but we find it to give worse fits.

we choose for the fit the two sets of three points such that $R_1 \leq R_c \leq R_2 < R_3$ and $R_1' < R_2' \leq R_c \leq R_3'$. A similar analysis is done for the two cubic fits. Notice however, that for $c = 9/4$ we only use one cubic fit in addition to the two quadratic fits. This is due to the finite size of the lattices and the fact that the measurements of the loops are only performed up to sizes of $R = L/2$.

The effect of the systematics in the interpolation are displayed in Figure 7.2. We show two different cases, first, when $R_c/a \approx 3.5$ on the left panel, and for $R_c/a \approx 4.9$ on the right. Clearly, when interpolating to 3.5 the errors from the interpolation are much larger and dominate over the statistical errors which are barely visibly in the inset plot. On the contrary, when R_c/a is close to an integer, the systematics are much smaller and are on the same order as the statistical fluctuations.

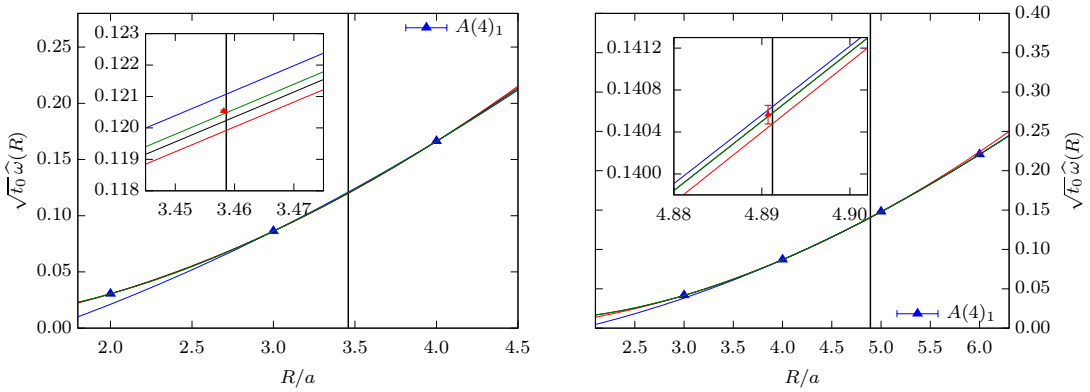

Figure 7.2: Systematic and statistical errors from the interpolation in R for the ensemble $A(4)_1$. On the left for $c = 1/2$, and on the right for $c = 1$. Notice that in the first case, the statistical error is barely visible in comparison to the systematic one, while on the second case, they are of roughly the same size.

Using the results from the different interpolating functions, the central value is determined as

$$W(c) \equiv W^{ct_0}(R_c) = 1/2\left(\max\{W_1, W_2, W_3, W_4\} + \min\{W_1, W_2, W_3, W_4\}\right) , \quad (7.7)$$

where W_i is the result from the $i-$th fit. The systematic error Δ_S is defined as

$$\Delta_S = 1/2\left(\max\{W_1, W_2, W_3, W_4\} - \min\{W_1, W_2, W_3, W_4\}\right) . \quad (7.8)$$

and is combined in quadrature with the statistical one to obtain the final error for each point. Concerning the interpolation to $t = t_c$, it is done with a quadratic function and is performed before all the R interpolation procedure. This part is not critical since the data has been measured over a small interval in t for each value of c.

7.2.1 Finite volume checks

Finite volume checks were performed by using the lattices $B(4)_1$ and $B(5)_1$ which have the same parameters as $A(4)_1$ and $A(5)_1$, but with a lattice spatial extension of $L/a = 24$, which corresponds to approximately 2.4 fm[4]. We only use the bigger lattices to explore whether our results, with the current uncertainty, hold at the infinite volume limit. Notice however, that we can test factorization independently of that, if we keep the physical volume fixed, so we use the data at 2.4 fm only in this section. For both W and W^2 we observe the data at 1.6 fm to be within statistical fluctuations of the data at 2.4 fm. The only sign of a trend is at $c = 9/4$, where the central values of the smaller lattices are below those of the large ones, for both SU(4) and SU(5) (see Figure 7.3).

7.3 Results

7.3.1 Continuum limits

The continuum limit is taken for all the gauge groups except for SU(8), where we have a single data point. For each group, the data is fitted to a polynomial in a^2/t_0 and we find excellent values for χ^2/dof when using a simple linear function. In the case of SU(4) and SU(5), we use the four available points and also perform a quadratic fit. We find the result from the quadratic fit to be consistent with that of the simpler linear fit. In order to reduce the systematics from the assumption of the range of validity of the leading linear term in the Symannzik expansion, we use only the three finest points, which fulfil the condition $a^2/t_0 < 0.25$. This choice enhances the error when compared to the fit using the four points, so we trade systematic by statistical errors. We apply the same condition for SU(6), i.e., we discard the coarsest lattice point when taking the continuum limit. In the case of SU(3), we use all three points as they are all consistent with the choice we have made. In Figure 7.4 we show the continuum limit fits for W and G_W, where we have included the linear fits using only the finest points, or including all of them. In all the cases, they produce compatible results. Interestingly, at $c = 9/4$, the slope of the a^2 corrections for W at $N = 3$ is smaller than the one of the larger N groups, and is in fact compatible with zero. Although we do not show the results for W^2, they are qualitatively similar to those obtained for W, i.e., the slope in a^2/t_0 is negative, and at $c = 9/4$ the SU(3) results have a slope close to zero.

[4]For the temporal extent, we use $T = 4L$.

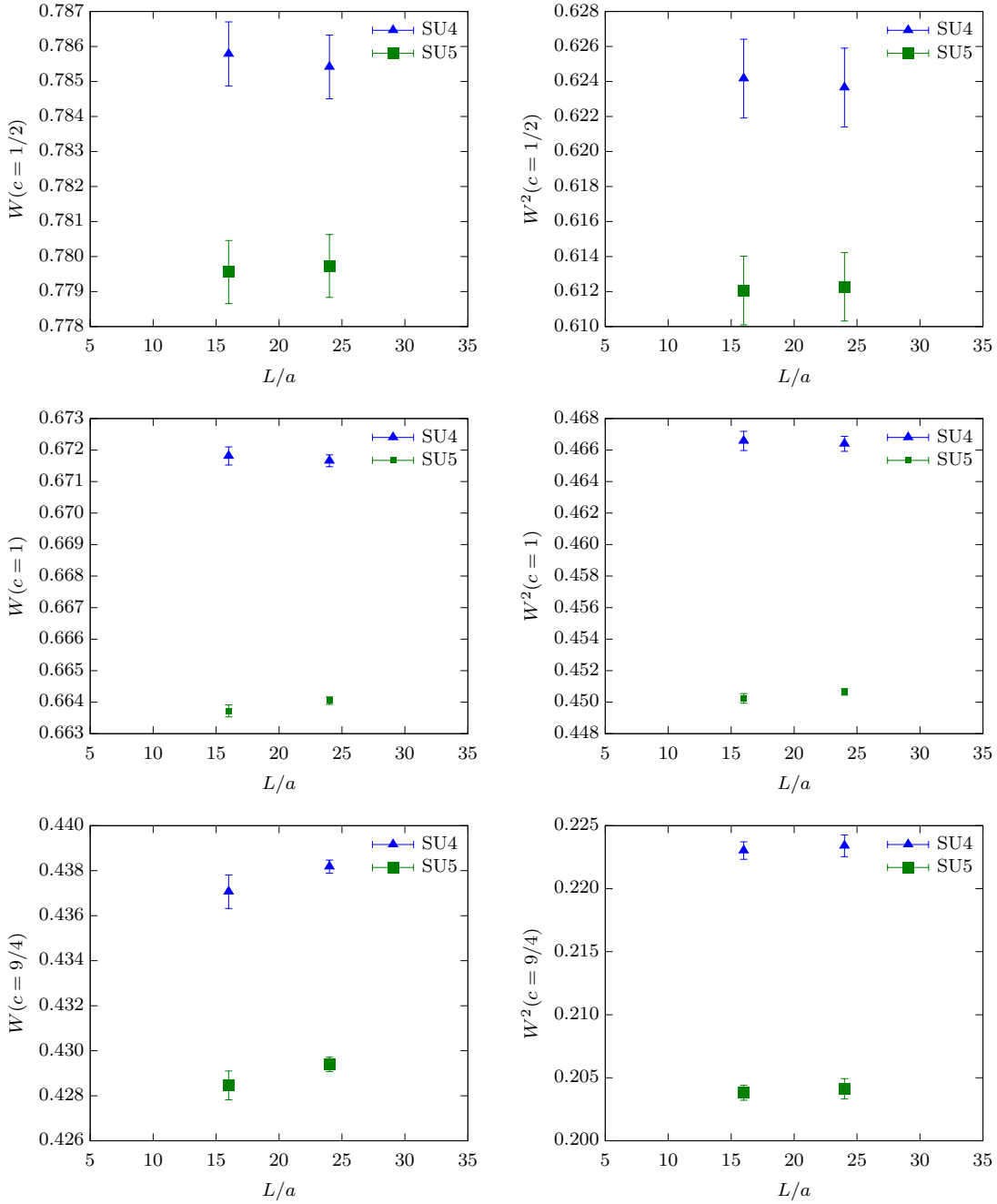

Figure 7.3: Finite volume checks for W and W^2 at the three values of c. We performed simulations at $L/a = 16$ and $L/a = 24$ at the coarsest lattice spacing for SU(4) and SU(5).

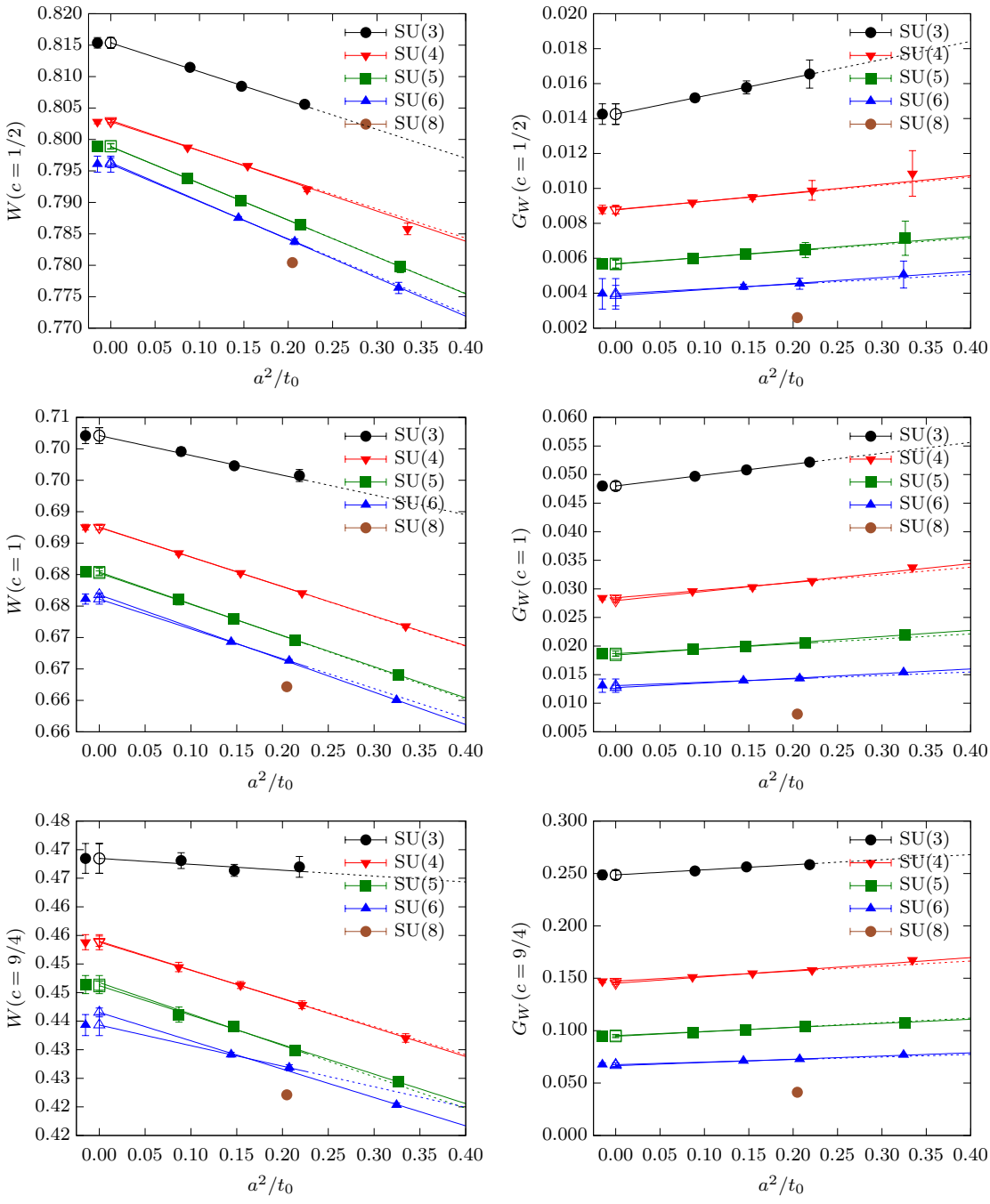

Figure 7.4: Continuum limit extrapolations of W and G_W. The open symbols are the individual continuum limit extrapolations using all or only the finest points. For better legibility, the final results, which correspond to the extrapolations using only the finest points, are plotted again and slightly displaced towards the negative x axis.

	$c = 1/2$	$c = 1$	$c = 9/4$
b_1/b_0	0.10(8)	0.54(10)	1.2(4)
b_2/b_0	1.3(5)	−0.5(7)	−3.3(2.8)
r_3	0.027	0.05	0.10

Table 7.2: Parameters of the large N extrapolation of W in the continuum.

7.3.2 Large N limits

Using the results of the continuum limit extrapolations, we are now in a position to take the large N limit of W and G_W. In addition to this, we also check at a finite lattice spacing, so that we can use the SU(8) data point. In this case, we interpolate to the desired value of a^2/t_0 for the rest of gauge groups. Clearly, by interpolating, the errors are smaller than those of the continuum extrapolations, and including an extra point at $N = 8$ allows us to present stronger evidence for factorization.

The strategy to take the large N limit is to fit the data to a polynomial in $1/N^2$ as predicted by the 't Hooft expansion. Let us first discuss our results for W in the continuum. We present the large N extrapolations in Figure 7.5. We performed a linear fit including only the points at $N > 3$, and a quadratic fit including the SU(3) result. As shown in Figure 7.5, the data for $N > 3$ is perfectly compatible with a linear fit, but the SU(3) point requires an $\mathrm{O}(1/N^4)$ correction. For each c let us use the fitting function

$$F(1/N^2) = b_0 + \frac{b_1}{N^2} + \frac{b_2}{N^4}\,. \tag{7.9}$$

In order to quantify the relevance of each term, we look at b_1/b_0 and b_2/b_0. The results are shown in Table 7.2. With the exception of the results at $c = 1/2$, our data shows that for the observables under consideration (we observe similar results for W^2), the first two parameters in the large N extrapolations are of the same order $\mathrm{O}(1)$. In the case of $c = 1/2$ however, the coefficient in front of the $\mathrm{O}(1/N^2)$ term is an order of magnitude smaller, which is evident in Figure 7.5, where the effects of considering a quadratic function are much more noticeable. It is interesting to also relate the large N limit to $N = 3$ directly, so we also include in Table 7.2 the relative distance $r_3 = (F(1/9) - b_0)/b_0$ between the result in SU(3) and the one at $N = \infty$. Notice that in the worst case, SU(3) is about 10% away from the $N \to \infty$ limit.

Next, we look into G_W in the continuum and proceed in a similar way. Same as for W, the SU(3) point is consistent with the 't Hooft expansion when including $\mathrm{O}(1/N^4)$ corrections. The coefficients of the quadratic fit are shown in Table 7.3. First, notice that b_0 is compatible with zero in all cases, and the large N scaling works excellent, as $\chi^2/\mathrm{dof} < 1$ at the three values of c. Moreover, for our particular observable, we find the parameters b_1 and b_2 to be of the same order of magnitude,

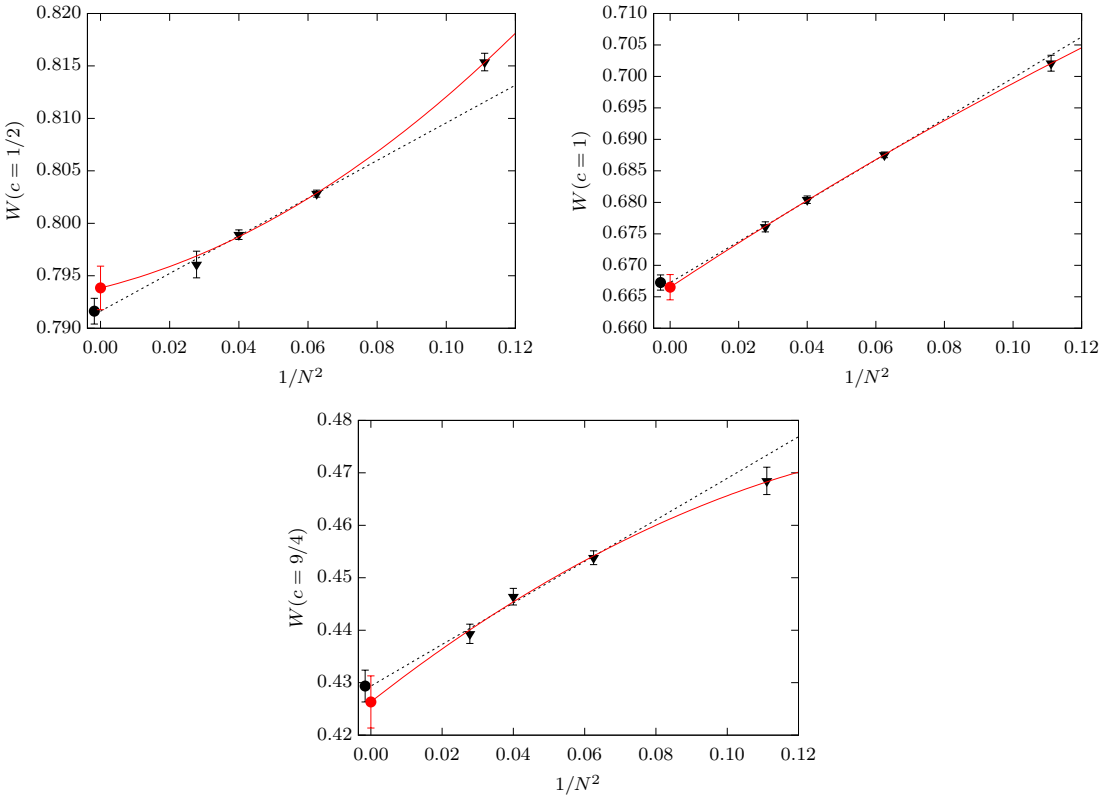

Figure 7.5: Large N extrapolations of W in the continuum. The dotted line is a linear fit to the data for $N > 3$, while the solid one is a quadratic fit which also includes the data at SU(3).

	$c = 1/2$	$c = 1$	$c = 9/4$
b_0	$-0.0007(13)$	$0.0001(19)$	$-0.0008(54)$
b_1	$0.17(4)$	$0.48(6)$	$2.50(19)$
b_2	$-0.35(29)$	$-0.46(40)$	$-2.2(1.5)$

Table 7.3: Parameters of the large N extrapolation of G_W in the continuum.

so the higher order corrections are only suppressed as $1/N^2$ and are not affected by a small or a large coefficient. A plot of G_W and the fits is shown in Figure 7.6 (left). Notice that in the case of $c = 9/4$, our prediction for the large N value of G_W has an error below the percent level, which in comparison to the value of G_W at SU(3), is almost two orders of magnitude smaller. This represents an excellent verification of factorization.

In order to use the data at SU(8) we interpolate the data for the rest of the groups to the value of $t_0/a^2 = 4.782$ and then take the large N limit. Using the fact that we have an extra point, we proceed differently as in the case of the continuum. In order to validate our check of factorization, we exclude the SU(3) point from the fits and perform a linear and quadratic fit to the rest of points. We show the results in Figure 7.6 (right), where it becomes clear that only the quadratic fit predicts correctly the SU(3) result. This is expected from what we have seen in the continuum, however, it is remarkable that it agrees so well when the fit is performed without including SU(3). By using SU(3) as a validation point, we have more confidence on the predictions from the quadratic extrapolating function. Notice that a linear fit to the data also produces reasonable values of χ^2/dof, except in the case of $c = 9/4$, where we obtain a value of $\chi^2/\text{dof} = 7.14$. We present the values of b_0 in Table 7.4 for both the linear (FL), the quadratic (FQ) and the quadratic fit including SU(3) (FQ3). As already mentioned, the SU(3) data point shows that within our errors, the $\mathrm{O}(1/N^4)$ corrections are necessary. On the other end, including the $\mathrm{O}(1/N^4)$ corrections has the consequence that the large N extrapolations agree with the value of zero predicted by factorization.

The conclusions regarding the large N extrapolations are the same as the ones obtained in the continuum, but with an even higher precision. Using again $c = 9/4$ as an example, the value of G_W at SU(3) is roughly the same as in the continuum, but the errors in the extrapolated value are almost at the level of one per mille. To push the tests even further, one could restrict the extrapolations to go to zero when $N \to \infty$ by using the fitting functions

$$F_{Lc}(1/N) = \frac{c_1}{N^2}\,, \tag{7.10}$$

$$F_{Qc}(1/N) = \frac{c_1}{N^2} + \frac{c_2}{N^4}\,, \tag{7.11}$$

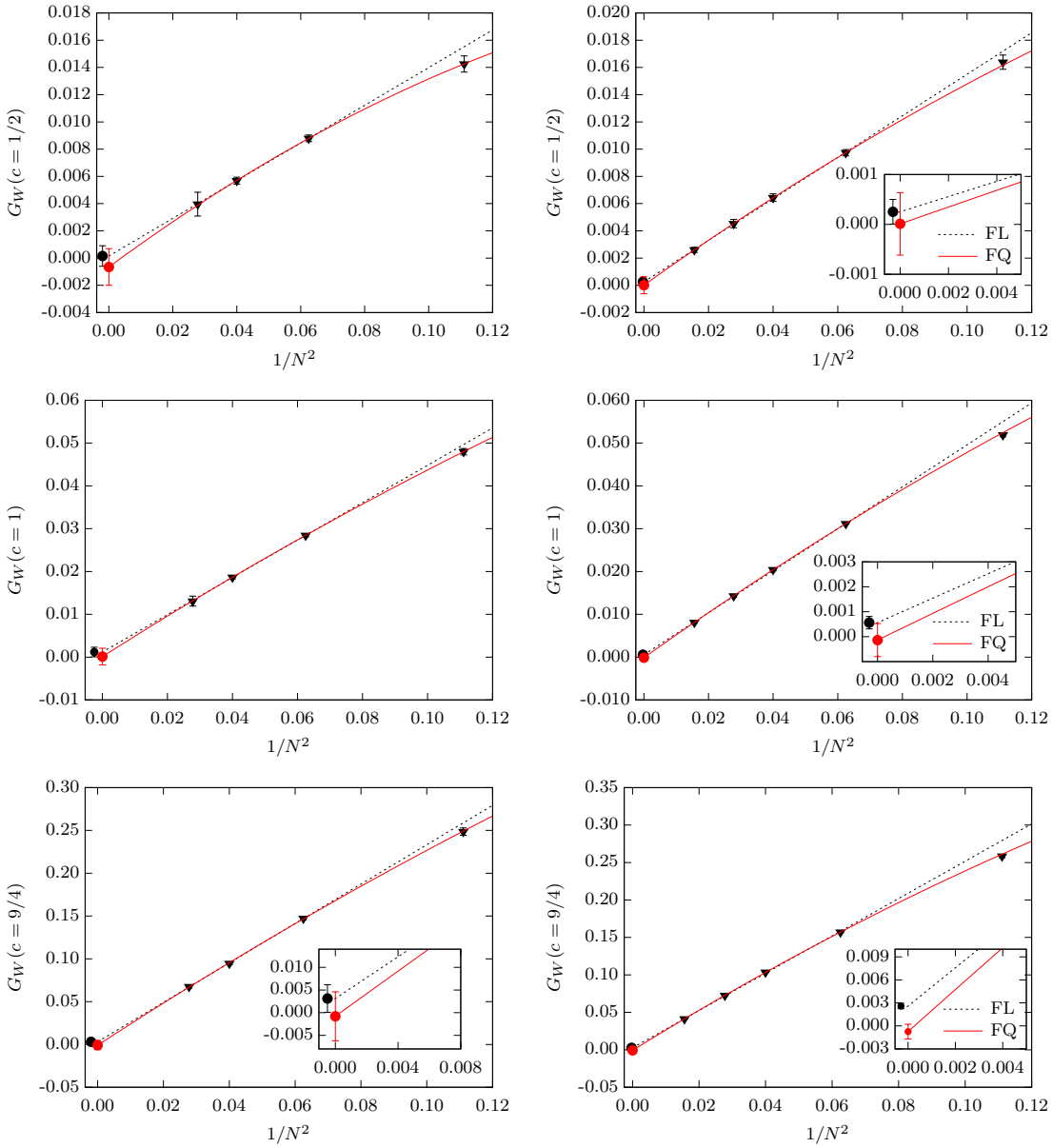

Figure 7.6: Large N extrapolations of G_W, on the left in the continuum, and on the right at a finite lattice spacing corresponding to $t_0/a^2 = 4.782$. The dotted line corresponds to a linear fit to the data excluding SU(3), while the solid one is a quadratic fit to all N in the case of the continuum (plots on the left), and a quadratic fit excluding SU(3) (FQ) for the data at finite lattice spacing (plots on the right). We observe excellent scaling with $1/N^2$ and the large N extrapolation agrees with the expectation from factorization in all the cases. Notice that at finite lattice spacing, FQ predicts a value at $N = 3$ which is perfectly compatible with our data point. The results from the extrapolations using a linear function have been slightly displaced for better legibility.

	$c = 1/2$	$c = 1$	$c = 9/4$
b_0(FL)	0.00025(25)	0.00056(25)	0.0026(4)
b_0(FQ)	0.00001(63)	−0.0001(7)	−0.0007(10)
b_0(FQ3)	0.00006(35)	−0.0003(3)	−0.0011(6)
χ^2/dof(FLc)	0.4	2.1	22.1
χ^2/dof(FQc)	< 0.01	0.03	0.4

Table 7.4: Parameters in the large N extrapolation of G_W at a finite lattice spacing corresponding to $t_0/a^2 = 4.782$. The results agree with the expectation from factorization.

	b_1/b_0	b_2/b_0	r_3
$c = 1/2$	2.6(6)	2.3(4.0)	0.3

Table 7.5: Parameters of the large N extrapolation of $\widetilde{W}$ in the continuum.

and then look at the value of χ^2/dof. Let us denote by FLc and FQc to the fitting strategies when using F_{Lc} or F_{Qc}, and excluding the SU(3) point from the fit. This would show whether the hypothesis of factorization is supported or not by our data. We report the values of χ^2/dof in Table 7.4, and they are all reasonable except for the linear fit FLc at $c = 9/4$. This is not surprising as the linear fit FL produces a value of $\chi^2/\text{dof} \approx 7$.

Finally, we perform an additional test by slightly changing the observable, so we define $\widetilde{W}(c) = W^{ct_0}\left(2\sqrt{8ct_0}\right)$. The only difference with respect to our previous observable is that now the ratio of the size of the loop to the smoothing radius is 2 instead of 1. Considering the finite size of the lattice, we can only compute this observable at $c = 1/2$. The parameters of the large N extrapolation of $\widetilde{W}$ are shown in Table 7.5. Also in this case, the coefficients of the $\mathrm{O}(1/N^2)$ and the $\mathrm{O}(1/N^4)$ terms are of similar O(1), and we observe the $N = 3$ results to be further away from the $N \to \infty$ when compared to the results for $W(c = 1/2)$ (see Table 7.2). The results for $G_{\widetilde{W}}$ in the continuum and at $t_0/a^2 = 4.782$ are shown in Figure 7.7. In this case, we plot the quadratic fit excluding SU(3) (FQ), and the one which includes it (FQ3). Unlike the case of G_W, the fit FQ does not predict correctly the SU(3) point. Nonetheless, both fits produce large N extrapolated values which are in excellent agreement with the prediction from factorization $G_{\widetilde{W}} \to 0$.

To conclude, let us stress once more that the results from this chapter represent to our knowledge the first explicit check of factorization on the lattice. By using the Yang-Mills gradient flow, we are able to test factorization not only at a finite lattice spacing but also in the continuum. In addition, our results give a non-perturbative confirmation of the $1/N^2$ scaling predicted by 't Hooft with great precision.

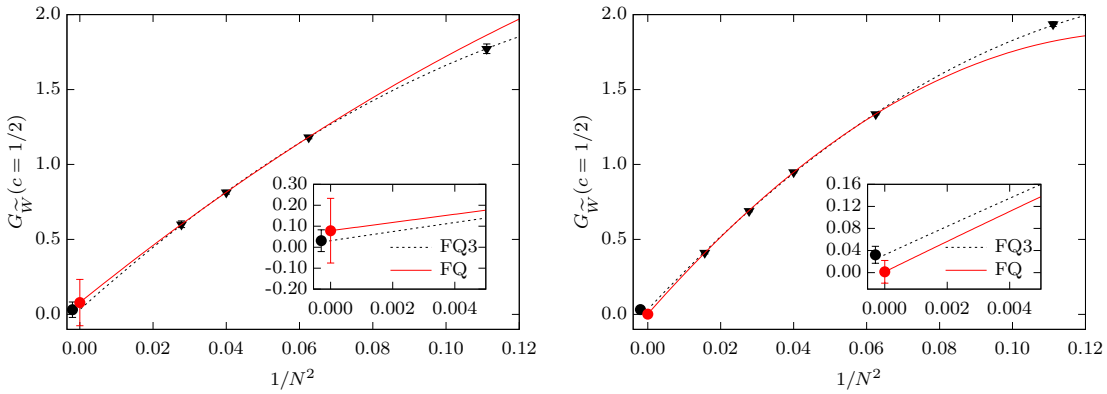

Figure 7.7: Large N extrapolation of $G_{\widetilde{W}}$ at $c = 1/2$. On the left in the continuum and on the right at $t_0/a^2 = 4.782$. The results are perfectly compatible with factorization.

8. Conclusions

In this thesis we have explored two aspects of the large N limit of SU(N) Yang-Mills gauge theories. First, we have looked into the computation of the topological susceptibility χ_{YM}, which has a direct physical consequence in explaining the large mass of the η' meson. Second, we have looked explicitly into the property of factorization. A key ingredient to define renormalizable observables was the use of the Yang-Mills gradient flow, which also provides a convenient definition of a scale t_0. From the algorithmic point of view, we have implemented a multilevel type algorithm suitable to the computation of correlation function of observables at positive flow time t.

Concerning the computation of the dimensionless quantity $t_0^2\chi_{\text{YM}}$, we have used for the first time the Yang-Mills gradient flow and open boundary conditions (OBC) to obtain a prediction of its large N and continuum limit, and obtain a final result with a 2% accuracy. In particular, using OBC allowed us to alleviate the freezing of the topology reported in previous works. In our case, we were able to simulate ensembles at a lattice spacing $a \approx 0.067\,\text{fm}$ up to the gauge group SU(6). By computing the integrated autocorrelation time τ_{int} and by monotoring the history of the charge, we are confident that our simulations are not stuck in any particular topological sector.

As discussed in Chapter 6, one of the main problems with computing χ_{YM} has to do with the severe signal to noise problem that affects the topological charge density correlator $\langle q(0)q(r)\rangle$. This motivated us to implement an algorithm to improve the scaling of errors in correlators computed at positive flow time. Although the algorithm was not applied to our ensembles for $N > 3$, we used the SU(3) data to estimate the tail of the $\langle q(0)q(r)\rangle$ correlator and thus have a good control over the systematics in χ_{YM}. We have also taken into consideration the systematics coming from the use of OBC as well as from the large N and continuum limit fits. Our final result in the continuum and $N \to \infty$ limit is $t_0^2\chi_{\text{YM}} = 7.03(13) \times 10^{-4}$. This particular value is only 5% away from the one for SU(3) reported in the literature [97], and thus shows that the $1/N^2$ corrections are small for this observable.

Notice that in order to express our results in dimensionless units, we used the scale t_0, conveniently generalized for the case of the gauge group SU(N). Our choice for the definition of t_0 cancels the leading N dependence of $\langle t^2 e^t\rangle$ in perturbation theory, and allows for the reliable large N extrapolation of the observables that we

have considered in this work. In the case of the topological susceptibility, if our large N result is to be used to give an explicit physical value for $\chi_{\text{YM}}^{1/4}$ in the usual MeV units, a more thorough study of the large N limit of the t_0 scale is needed.

As mentioned before, we have developed an algorithm to improve over the traditional $1/\sqrt{n}$ scaling of Monte-Carlo simulations, where n is the total number of measurements. Our algorithm is based on the multilevel algorithm and as such, it takes advantage of the locality of the action. In Chapter 5 we have described a way to use the multilevel type updates together with non-local observables smoothed with the Yang-Mills gradient flow. Our numerical results confirm that the errors scale as $1/\left(\sqrt{n_0}n_1\right)$, where $n = n_0 n_1$ is the total number of updates. From the way in which the algorithm is constructed, it is the most efficient when looking at the correlation function $\left\langle \mathcal{O}^t(0)\mathcal{O}^t(r)\right\rangle$ at large values of r in units of the smoothing radius $\sqrt{8t}$. We also studied analytically the scaling of the error for the two point function with respect to n_1, and argue that although the leading term goes down as $1/\left(\sqrt{n_0}n_1\right)$, there are subleading contributions which decay only as $1/\sqrt{n_0 n_1}$ or $1/\sqrt{n_0}$. Although those terms are suppressed for correlators evaluated at large r, our results provide a better theoretical understanding of why is that the case.

In Chapter 7 we presented our results related to the factorization of the product of Wilson loops in the large N limit. Our results present very convincing evidence that this property holds for smoothed Wilson loops at finite lattice spacing and in the continuum. To our knowledge, this represents the first direct verification of factorization on the lattice. By using smooth Wilson loops, we were able to check not only factorization in the continuum, but also the $1/N^2$ scaling predicted by the 't Hooft topological expansion. For some of our observables, we find that corrections of $\mathrm{O}(1/N^2)$ describe very well our data for $N > 3$, while including the result at SU(3) generally requires the addition of a term of $\mathrm{O}(1/N^4)$. In general, we find the coefficients of the $1/N^2$ and the $1/N^4$ terms to be of the same and natural order. Of course, this is observable dependent.

To conclude, let us stress the fact that throughout the numerical computations presented in this thesis, we have found excellent agreement with the large N 't Hooft expansion, which in the case of the pure Yang-Mills theory, tells us that corrections to the $N \to \infty$ limit are organized in powers of $1/N^2$. Generally we find this formula to be valid even up to the physical value of $N = 3$ with small corrections.

A. openSUN

Here we describe the most relevant details related to the algorithm implemented to perform the updates and measurements used throughout this thesis. From now on we refer to it as openSUN, as it is based on the openQCD package [126] and it has been modified to work with the general gauge group SU(N) for the case of the pure Yang-Mills theory. As a derivative of openQCD, the code has been written entirely in C language.

The fundamental modification to openQCD is the inclusion of the parameter NCOL, which corresponds to the number of colours N. It is defined at compilation time, for example, in the case of SU(6) as

```
#define NCOL 6
```

The gauge links are then stored as general complex $N \times N$ matrices, while the elements of the Lie algebra $\mathfrak{su}(N)$ are stored as a real vector of length $N^2 - 1$. The parametrization used for the elements of the Lie algebra is explicitly represented in Eq. (A.4).

Correspondingly, all functions and macros from openQCD have been suitably modified to work with the new data structures. The geometry of the lattice has been left unchanged with respect to openQCD. For the update of the gauge fields, one can either use the hybrid Monte-Carlo (HMC) algorithm or the hybrid over-relaxation algorithm described in Sec. 4.2.2. We start describing the most relevant aspects concerning the implementation of the HMC algorithm.

A.1 openSUN-HMC

A.1.1 The hybrid Monte-Carlo algorithm

The Hybrid Monte-Carlo algorithm (HMC) is predominantly used for the theory including fermions, and although the discussion of fermions in the lattice and the problems associated with their introduction is beyond the scope of this thesis, we briefly describe the HMC as it has been implemented as part of openSUN.

The algorithm makes use of the classical molecular dynamics equations for a system with a Hamiltonian given by

$$H(X,U) = \frac{1}{2}X^2 + S_G(U)\,, \tag{A.1}$$

where $X^2 = \sum_{x,\mu}(X_\mu(x), X_\mu(x))$, and $X_\mu(x) = X^a_\mu(x)T^a$ is an $\mathfrak{su}(N)$ valued field that is artificially added to the theory (see Sec. A.1.2), such that

$$\int d[U]\mathcal{O}(U)e^{-S(U)} \propto \int d[X]d[U]\mathcal{O}(U)e^{-H(X,U)}\,. \tag{A.2}$$

Notice that the expectation value of observables remain the same after the proper normalization. A chain of configurations is then generated by integrating the Hamiltonian equations of motion in a fictitious time t

$$\begin{aligned} \frac{dX_\mu(x)}{dt} &= -F_\mu(x)\,, \qquad F^a_\mu(x) = \frac{\partial S(e^{\lambda^a T^a}U)}{\partial \lambda^a}\Big|_{\lambda=0} \\ \frac{dU_\mu(x)}{dt} &= X_\mu(x)U_\mu(x)\,. \end{aligned} \tag{A.3}$$

The HMC strategy is then the following

1. Generate random momentum X with a probability density proportional to $\exp\{-\frac{1}{2}X^2\}$.
2. Integrate the molecular dynamic equations (A.3) from $t = 0$ to $t = \tau$.
3. Replace $U'_\mu(x) = U_\mu(x)_{t=\tau}$.

In practice, the equations of motion are integrated numerically, and one has to find a way to deal with the integration error introduced by any numerical integration scheme. The integrators must also have the property to be area preserving, so one commonly uses the leap-frog integrator, or the general class of OMF integrators [127]. Notice that if the equations were integrated exactly, the evolution preserves the Hamiltonian H, however, the integration process introduces an error which depends on the type of integrator used. To compensate this, one adds an acceptance-rejection step at the end of the integration. If the Hamiltonian H evaluated at time τ has decreased or remained the same compared to the its value at $t = 0$, the new configuration is immediately accepted. On the contrary, if H has increased, the new configuration is only accepted with probability $e^{-\Delta H}$, where ΔH is the change in the Hamiltonian. If the trajectory is not accepted, the gauge configuration goes back to its original value at $t = 0$.

Clearly, the higher order integrators, such as the 4-th order OMF will have smaller errors at a fixed integration step size ϵ than the simpler leap-frog integrator. In practice, the value of ϵ is tuned to obtain a good acceptance rate, generally above

90%. Concerning the trajectory length τ, it is not a trivial issue and it has to be chosen as to minimize the autocorrelation times, while keeping an stable numerical integration. In general, this parameter has to be scaled proportional to a relevant correlation length. Completion of a full HMC integration step is commonly referred to as one molecular dynamic unit, or MDU.

A.1.2 Implementation

In the case of the HMC, the parallelization is the same as that of openQCD; basically, the lattice is split into sub-blocks which are updated independently by different MPI processes. The communication routines were modified to accommodate the larger SU(N) matrices. For most of the functions, the generalization from SU(3) to SU(N) is straightforward, except for the case of the random momentum generator needed to produce the X field which enters in the Hamiltonian in Eq. (A.1), and the exponential function required to compute the force F in Eq. (A.3). Additionally, the exponential function is used in the evolution of the gradient flow, so it plays a crucial role in our work. Notice that in both cases, the functions we need are defined for elements of the $\mathfrak{su}(N)$ algebra.

Random momenta

The first step in the update of a gauge configuration using the HMC algorithm is the generation of a set of random momenta $X = \{X_\mu(x), X_\mu(x) \in \mathfrak{su}(N)\}$, where x and μ run through all the links of the lattice. X is generated with a probability density given by $\exp\{-\frac{1}{2}X^2\}$, where $X^2 \equiv \sum_{x,\mu}(X_\mu(x), X_\mu(x)) = -2\sum_{x,\mu}\mathrm{Tr}\big(X_\mu(x)^2\big)$ is given in terms of the scalar product of $X_\mu(x)$ with itself[1]. In the end, we need to generate the matrices $X_\mu(x)$ with probability density proportional to $\exp\big(\mathrm{Tr}\big(X_\mu(x)^2\big)\big)$. For simplicity, let us drop the x and μ dependence, and write $W = X_\mu(x)$.

Given that $W \in \mathfrak{su}(N)$, it can be parametrized by a set of N^2-1 real parameters $\{W^0, \cdots, W^{N^2-2}\}$ in the following way

$$W = \begin{pmatrix} iW^0 & W^{N-1}+iW^N & W^{N+1}+iW^{N+2} & \cdots & \cdots \\ & iW^1 & W^{3N-3}+iW^{3N-2} & \cdots & \cdots \\ & & iW^2 & \cdots & \cdots \\ & & & \cdots & \cdots \\ & & & \cdots & \cdots \\ & & & iW^{N-2} & W^{N^2-3}+iW^{N^2-2} \\ & & & & -i\sum_{j=0}^{N-2}W^j \end{pmatrix} \tag{A.4}$$

[1]Note that in our convention $\mathrm{Tr}\left(T^aT^b\right) = -\frac{1}{2}\delta^{ab}$.

where the lower diagonal part is fixed by the condition that W is an anti-hermitian matrix. Then

$$\mathrm{Tr}\left(W^2\right) = -\sum_{i=0}^{N-2}\sum_{j\geq i}^{N-2} 2W^iW^j - \sum_{i=N-1}^{N^2-2} 2\left(W^i\right)^2 , \tag{A.5}$$

from where one can see that for $i \geq N-2$ all the W^i are decoupled from the rest and can be generated from a Gaussian distribution. However, for $i \leq N-1$ one has to diagonalize the quadratic form in order to simplify it and use a convenient Gaussian random number generator.

The problem reduces then to find a matrix V such that $V^TMV = I$, with M given by

$$M = \begin{pmatrix} 2 & 1 & 1 & 1 & \cdots & 1 \\ 1 & 2 & 1 & 1 & \cdots & 1 \\ 1 & 1 & 2 & 1 & \cdots & 1 \\ \vdots & & & & & \\ \vdots & & & & & \\ & & & & & \\ 1 & & & & & 2 \end{pmatrix}_{(N-1)\times(N-1)} \tag{A.6}$$

and I the identity matrix of size $(N-1)\times(N-1)$

Using the new set of coordinates Y^i given by $W^i = V_{ij}Y^j$ the first term in Eq. (A.5) turns into $-\sum_{i=0}^{N-2}\left(Y^i\right)^2$ and one can generate all the Y^i parameters in an independent way using a suitable gaussian random number generator. Finally, one goes back to the original W^i coordinates using the change of basis matrix V. Clearly, this procedure has to be repeated for all matrices $W \in X$.

Because of the simple form of M, the matrix V can be written explicitly for any N and is given by

$$V = \begin{pmatrix} c_1 & -a_1 & -a_2 & -a_3 & \cdots \\ c_1 & a_1 & -a_2 & -a_3 & \cdots \\ c_1 & 0 & 2a_2 & -a_3 & \cdots \\ \vdots & \vdots & 0 & 3a_3 & \cdots \\ c_1 & 0 & 0 & 0 & \end{pmatrix}_{(N-1)\times(N-1)} \tag{A.7}$$

where $c_1 = 1/\sqrt{N(N-1)}$, and the rest of constants are fixed if one imposes the condition that every column must be normalized to unity.

Exponential mapping

The exponential mapping is used for both the HMC integration, as well as for the evolution of observables with the gradient flow. The prescription we use is a generalization of the method presented in the Appendix of Ref. [128].

Given a matrix $W = w_{ij} \in \mathfrak{su}(N)$[2], we want to compute $\exp(\epsilon W)$ for some small parameter ϵ. First, we build a set of $N(N-1)/2$ matrices given by the SU(2) subrotations of SU(N) corresponding to the indexes $(i,j)_{i\neq j}$ in the following way

$$Y_{(i,j)} = \begin{pmatrix} 0 & \cdots & \cdots & \cdots & \cdots & \cdots & 0 \\ \vdots & \vdots & \vdots & & & & \\ 0 & \cdots & y_{ii}^{jj} & \cdots & w_{ij} & 0 & \cdots \\ 0 & \cdots & 0 & \cdots & \cdots & \cdots & 0 \\ 0 & \cdots & w_{ji} & \cdots & -y_{ii}^{jj} & 0 & \cdots \\ 0 & 0 & 0 & \cdots & & & \\ \vdots & \vdots & \vdots & \vdots & & & \end{pmatrix} \tag{A.8}$$

with $y_{ii}^{jj} = \left(w_{ii} - w_{jj}\right)/N$. Note that $Y_{(i,j)}$ defined in this way is still an element of $\mathfrak{su}(N)$. We use the matrices Y to then obtain a new set of $N(N-1)/2$ matrices $U_{i,j}$

$$\begin{aligned} U_{(i,j)} &= \left(I + (1/2)Y_{(i,j)}\right) \times \left(I - (1/2)Y_{(i,j)}\right)^{-1} \qquad \text{for} \quad i = N-1, j = N \\ U_{(i,j)} &= \left(I + (1/4)Y_{(i,j)}\right) \times \left(I - (1/4)Y_{(i,j)}\right)^{-1} \qquad \text{otherwise} \end{aligned} \tag{A.9}$$

Finally one computes $E'(W) = U_{(1,2)} \times U_{(1,3)} \times \cdots \times U_{(N-2,N)} \times U_{(N-1,N)} \times U_{(N-2,N)} \times \cdots \times U_{(1,3)} \times U_{(1,2)}$. It is easy to check that $E'(\epsilon W)$ is unitary and also that $E'(\epsilon W) = \exp(\epsilon W) + O(\epsilon^3)$, so it provides a good approximation for the exponential function with errors $\mathrm{O}(\epsilon^3)$.

The error can be further reduced by using a scaling and squaring approach so that $\exp(\epsilon W) = \exp(\epsilon/2^n W)^{2^n}$, which produces a result with an error $\mathrm{O}\left((\epsilon/2^n)^3\right)$. In our case, for the precision of the observables presented in this thesis, we find a good choice to be $n = 3$. Clearly, larger n would produce better results, but at the expense of a larger computational cost.

[2]Notice that in this case we are not using the parametrization from the previous section.

A.2 openSUN-DDHOR

The implementation of the hybrid over-relaxation algorithm results in a larger departure from the original openQCD code. First, the update is local and is performed using the Cabibbo-Marinari strategy to update the SU(N) matrices. Second, the strategy used for the parallelization is similar to the one used in the DDHMC code [128, 129]. Hence, we have adopted the name openSUN-DDHOR. In addition, we have introduced openMP parallelization in the time direction, which is completely new with respect to openQCD.

A.2.1 Implementation

We show an scheme of the parallelization strategy in Figure A.1. Only the links which are connected to at least one black filled point are updated, while those that connect only to the open points are unchanged during a sweep of the lattice. This defines independent blocks which are updated by different MPI processes. Unlike the DDHMC algorithm, the blocking is only performed in the spatial directions due to the presence of open boundary conditions in the time direction. For a homogenous block of size $B/a \times T/a$, one can compute the ratio R of active links, i.e., those that are updated, to the total number of links in the block

$$R = \frac{(B/a-2)^2\,(B/a+1)}{(B/a)^3}\,. \tag{A.10}$$

In this sense, the smaller the block, the smaller the effort to update the lattice. However, this is compensated by an increase in the integrated autocorrelation time τ_{int}, such that the product $R\tau_{\text{int}}$ remains constant [128]. As shown in Ref. [128] and as we present in the next section, at small B/a this is no longer true and the product $R\tau_{\text{int}}$ becomes larger, so that using smaller blocks becomes unpractical.

Once the update of each block is completed, the lattice is shifted following the procedure described in Ref. [128]. Given that we do not parallelize in the time direction, the shift is only performed in the spatial directions. As depicted in Figure A.1, each of the MPI blocks is subsequently parallelized using openMP in the time direction. We have also made explicit the fact that constructions such as OMP barriers are added to avoid a race condition between two threads updating adjacent gauge links.

To summarize, openSUN-DDHOR is parallelized using both MPI in the spatial directions and openMP in the time direction. This choice was made in order to take advantage of the simple parallelization strategy from the DDHMC algorithm, and adapt it for the case of open boundary conditions. For the update routine, in the current state, roughly 94% of the routine is parallelized with openMP. This limits the efficiency of the openMP parallelization, as per Amdahl's law [130], the

theoretical maximum speed up is around 17. In practice, for the parallelization in the time direction, using multi-threading and up to 12 openMP threads (equivalent to 6 individual cores) we observe an speed up of around 4.7. If multi-threading is disabled, the speed up factor increases to a factor of around 6.9, but the number of cores doubles. To be the most efficient, the majority of our simulations were run with multi-threading enabled and 4 to 6 openMP threads.

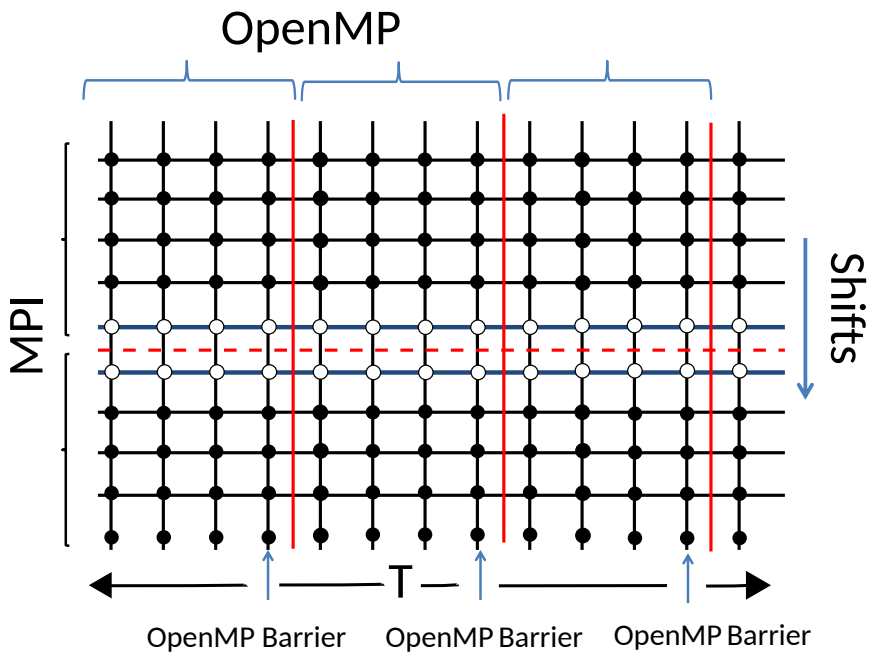

Figure A.1: Parallelization strategy of the lattice in the openSUN-DDHOR algorithm. The lattice is split into independent blocks in the spatial directions, which are parallelized using MPI. The time direction T is parallelized using openMP. In order to update all the links, the lattice is shifted in the time direction after every sweep following the prescription described in Ref. [128].

Effects of the block size and the order of the sweep

To speed up the simulations, in principle one would like to use as many MPI processes as possible. However, in our domain decomposition approach, having too small block sizes affects the integrated autocorrelation times of the observables in a negative way. As part of the tuning of the algorithm we looked at the integrated autocorrelation times[3] of Q and Q^2, on lattices parallelized with three different block sizes in the case of SU(3) and two block sizes for SU(5). The ensembles are listed in Table A.1.

[3]Notice that both Q as well as Q^2 are summed only over the plateau region in the time direction.

The block sizes used for the comparison, $4^3 \times 64$ and $8^3 \times 64$, produce values of $R = 0.17$ and $R = 0.47$ respectively.

In addition, we also want to bring up some attention on the effect of the order of the local sweep on the autocorrelations. As pointed out in Ref. [131], this can have a relevant effect in the autocorrelations. In our experience, it has a small but noticeable effect. To show this, in Table A.1 we have also included the results from sweeping through the local lattice in two distinct ways:

- U1: Go through all odd points (i.e, those for which the sum of their coordinates is an odd integer) looping through all μ directions first. Then go through all even points in a similar way.
- U2: Keep the direction μ as the outermost loop and go through the points in a lexicographical order.

Because of the way the gauge links are allocated in memory in openQCD, the first strategy is faster by around 6%. This only considers the time it takes to update the sub-block. The ensembles in Table A.1 which are labelled with a B at the start, are updated using the strategy U1, while the others are updated following the prescription from U2.

Two conclusions can be extracted from looking at the integrated autocorrelation time τ_{int} of Q and Q^2. First, concerning the effect of the block size, we observe that when going from $B/a = 8$ to $B/a = 4$, the algorithm becomes very inefficient. Whether this has to do with the small value of $R = 0.17$, or is related to the physical size of the block is something that should be further explored. To be safe, in all the production runs listed in the main text, the conditions $B/a \geq 8$ and $B \geq 0.6\,\text{fm}$ where imposed.

The second observation from Table A.1 is that the strategy U2 for updating the links, i.e., a lexicographical sweep keeping the gauge link direction μ as the outermost loop, helps to reduce autocorrelations by a factor of approximately 1.5. In view of this, we use the strategy U2 for the update in the production runs.

A.3 Average plaquette

As has been reported in Refs. [132, 133], there is a first order bulk phase transition that separates the lattice from the continuum theory. It is indeed also present in the large N limit at a value of $b = 0.36$. The transition is observed in the values of the average plaquette u_p, so for completeness we report our findings in this respect. In Table A.2 we show a summary of the results obtained for several gauge groups and several values of β. The values of β were chosen as to match those in Ref. [134]. The gauge configurations were generated using openSUN-HMC with a trajectory length $\tau = 1$, and measurements were separated by 8 MDU. In the case of SU(6) and SU(8)

#run	N	L/a	T/a	Block	β	$R\,\tau_{int}(Q)$	$R\,\tau_{int}(Q^2)$	N_{meas}	N_{upd}
$D1(3)_1$	3	16	64	$4^3 \times 64$	6.13	237(120)	193(91)	14000	4
$D2(3)_1$	3	16	64	$8^3 \times 64$	6.13	48(13)	34(12)	4500	4
$D3(3)_1$	3	16	64	$16^3 \times 64$	6.13	43(12)	27(8)	2500	4
$BD1(5)_1$	5	16	64	$4^3 \times 64$	17.32	561(268)	237(83)	7500	24
$D1(5)_1$	5	16	64	$4^3 \times 64$	17.32	374(133)	181(44)	9900	24
$BD2(5)_1$	5	16	64	$8^3 \times 64$	17.32	198(80)	74(18)	2300	24
$D2(5)_1$	5	16	64	$8^3 \times 64$	17.32	126(45)	68(19)	2300	24

Table A.1: Parameters and computed values of τ_{int} for the ensembles used to study the dependence of autocorrelations on the block size and the order of the sweep. We present the lattice dimensions, the block size, the inverse lattice coupling β, the values of $R\tau_{\text{int}}$ for Q and Q^2, the number of measurements N_{meas} and their separation in unit of updates N_{upd}. In all of the ensembles we chose $N_{\text{or}} = L/2a$. The parallelization was done only with MPI, so that the effect of the order of the sweep could be studied.

we clearly observe a big jump in the value of the plaquette between G6b1 and G6b2, and between G8b4 and G8b5 respectively.

A.4 Measurement routines

In addition to the implementation of the code for the generation of the gauge configurations, we have also implemented several measurement routines as part of openSUN. The main ones are listed below.

- Measurement of the topological charge and the Yang-Mills energy density: the routine is parallelized with MPI and openMP, so that it can be used for online measurements in openSUN-HMC and openSUN-DDHOR.
- Integration of the Yang-Mills gradient flow equations: we have implemented the integrators for both the standard Wilson flow as well as the Zeuthen flow [135]. In the case of the standard Wilson flow the routine is parallelized with MPI and openMP, while the Zeuthen flow only supports MPI parallelization at the current stage.
- Measurement of smooth Wilson loops: we have modified the routine wloop[4] to work for general gauge group SU(N) and to use the Yang-Mills gradient flow integrators. Only in the case of the standard flow the measurement can be performed online with openSUN-DDHOR.

[4] https://github.com/bjoern-leder/wloop

#run	N	β	b	Nsteps	Pacc	N_{meas}	u_p
G2b1	2	2.1768	0.272	16	0.99	1126	0.56081(23)
G2b2	2	2.2400	0.280	16	0.99	1126	0.58278(35)
G3b1	3	5.6500	0.314	20	0.96	1126	0.53734(28)
G3b2	3	5.6750	0.315	20	0.96	1126	0.54346(21)
G4b1	4	10.480	0.328	24	0.95	1126	0.52427(35)
G4b2	4	10.500	0.328	24	0.95	501	0.52936(32)
G6b1	6	24.300	0.338	34	0.94	1126	0.42058(12)
G6b2	6	24.515	0.340	34	0.93	501	0.53248(15)
G6b3	6	25.452	0.354	34	0.93	501	0.56865(9)
G8b1	8	43.625	0.341	36	0.89	1126	0.39114(6)
G8b2	8	43.85	0.343	36	0.90	501	0.39576(10)
G8b3	8	44.00	0.344	36	0.89	501	0.39942(9)
G8b4	8	44.35	0.346	36	0.89	501	0.40856(12)
G8b5	8	44.85	0.350	34	0.87	501	0.54958(9)
G8b6	8	45.70	0.357	36	0.88	501	0.56574(8)

Table A.2: Results for the computation of the average plaquette u_p. For each ensemble we report the inverse lattice coupling β, the inverse 't Hooft coupling b, the number of steps Nsteps in the integration of the HMC equations, the acceptance probability Pacc and the number of measurements N_{meas}. The total number of MDUs can be calculated as $8N_{\text{meas}}$.

B. Multilevel

B.1 Factorized Variance

In this first section we give a simple argument to understand why a multilevel type approach should help at improving the scaling of errors in a Monte-Carlo simulation. In order to show how we can take advantage of the factorized observables as in Eq. (5.5), we look at how the variance of an observable depends on its distance to B. Take B to be the spatial links located at the time slice x_0^B. Then, L and R are all the gauge links which are located to the left or to the right of B respectively. Consider the observable $\mathcal{O}(x)$ constructed from links $U_L \in L$ and let us denote by z the distance between x and the boundary at x_0^B. To simplify the discussion let us keep track of the distance to the boundary, so we write $\mathcal{O}(z)$ instead of $\mathcal{O}(x)$. Then, using Eq. (5.5) one has

$$\langle \mathcal{O}(z) \rangle = \frac{1}{Z} \int dU_B dU_L dU_R e^{-S} \mathcal{O}(z) = \int dU_B \, p(B) \, [\mathcal{O}(z)]_L$$

Now we define

$$\begin{aligned} \sigma_B^2 &\equiv \sigma^2([\mathcal{O}(z)]_L) = \left\langle [\mathcal{O}(z)]_L^2 \right\rangle - \langle [\mathcal{O}(z)]_L \rangle^2 = \left\langle [\mathcal{O}(z)]_L^2 \right\rangle - \langle \mathcal{O}(z) \rangle^2 \, , \\ \sigma_L^2 &\equiv \left\langle \sigma_L^2(\mathcal{O}(x_0)) \right\rangle \equiv \left\langle \left[\mathcal{O}^2(z)\right]_L \right\rangle - \left\langle [\mathcal{O}(z)]_L^2 \right\rangle = \left\langle \mathcal{O}^2(z) \right\rangle - \left\langle [\mathcal{O}(z)]_L^2 \right\rangle \, , \end{aligned} \tag{B.1}$$

where the subscripts L and B are added to denote whether we expect the main contributions to the quantity to come either from the fluctuations in L or B respectively. Notice that in the case of σ_B, we have first averaged over $U_L \in L$ and we are then looking at the variance over B of this average. σ_L on the other hand consists first on the variance over L for a fixed B which is then averaged over the $U_B \in B$ field configurations. Clearly, $\sigma^2(\mathcal{O}(z)) = \sigma_B^2 + \sigma_L^2$.

Let us evaluate the first term in σ_B^2, i.e. $\left\langle [\mathcal{O}(z)]_L^2 \right\rangle$.

$$\begin{aligned}\left\langle [\mathcal{O}(z)]_L^2 \right\rangle &= \int dU_B p(B) \frac{1}{Z_L} \int dU_L e^{-S_L}\, \mathcal{O}(z) \frac{1}{Z'_L} \int dU'_L e^{-S_{L'}}\, \mathcal{O}(z') \\ &= \int dU_B e^{-S_B} \frac{Z_L Z_R}{Z} \frac{1}{Z_L Z'_L} \int dU_L dU'_L e^{-S_L - S_{L'}}\, \mathcal{O}(z)\mathcal{O}(z') \\ &= \frac{1}{Z} \int dU_B dU_L dU_R e^{-S} \mathcal{O}(z)\mathcal{O}(z') = \left\langle \mathcal{O}(z)\mathcal{O}(z') \right\rangle , \end{aligned} \tag{B.2}$$

where z' is defined such that $\mathcal{O}(z')$ is at the same distance from the boundary as $\mathcal{O}(z)$. In the first line we used the fact that $[\mathcal{O}(z)]_L^2$ can be written as the product of two observables integrated over L, so we simply changed the name of the integration variable. From the second to the third line we used the fact that the action is local and symmetric respect to the boundary at x_0^B, and so one has the property $Z'_L = Z_R$.

Finally, considering the definition of z' and using translation invariance, one can rewrite Eq. (B.2) as

$$\left\langle [\mathcal{O}(z)]_L^2 \right\rangle = \langle \mathcal{O}(0)\mathcal{O}(2z) \rangle \approx \langle \mathcal{O}(z) \rangle^2 + O(e^{-2\Delta E_1 z}) \tag{B.3}$$

Then for z large, i.e., for an observable defined at a large distance from the boundary, one has that $\sigma_B^2 \propto O(e^{-2E_1 z})$, while σ_L^2 carries the full variance of the observable up to exponential corrections. This simple result shows that updating the lattice in separate domains has the advantage that up to $\mathrm{O}(e^{-2\Delta E_1 z})$, the variance, and hence the error, do not feel the effects of the boundary B, which allows each sub-domain to be updated independently.

B.2 Details on the multilevel error scaling formula

In this section we look into the different terms in Eq. (5.17) and argue that the leading contribution comes from the one proportional to $1/\left(\sqrt{n_0} n_1\right)$. This is explicitly shown by our numerical results, however, we intend to give some explanation of why this is the case. For reference, let us rewrite the main equation we wish to study here

$$\begin{aligned}\sigma_A^2 = \frac{1}{n_0 n_1^2} \left\langle \Delta_L\left(\mathcal{O}\right) \Delta_R\left(\mathcal{O}'\right) \right\rangle + \frac{1}{n_0} \left(\left\langle [\mathcal{O}]_L^2 \left[\mathcal{O}'\right]_R^2 \right\rangle - \bar{A}^2 \right) + \\ + \frac{1}{n_0 n_1} \left(\left\langle \Delta_L\left(\mathcal{O}\right) \left[\mathcal{O}'\right]_R^2 + \Delta_R\left(\mathcal{O}'\right) \left[\mathcal{O}\right]_L^2 \right\rangle \right) , \end{aligned} \tag{B.4}$$

where $\mathcal{O} = \mathcal{O}(x_0)$ is defined only in terms of links $U_L \in L$ and $\mathcal{O}' = \mathcal{O}(y_0)$ depends only on links $U_R \in R$, and have been summed over the spatial coordinates. For

simplicity, let us assume that the distance from source and sink to the boundary at x_0^B is the same and equal to z_0.

In order to understand the scaling of each term, let us look into $[\mathcal{O}(x_0)]_L$. The expectation value can be computed using the transfer matrix formalism

$$[\mathcal{O}(x_0)]_L = \frac{1}{\mathcal{Z}_L} \langle\gamma|\ \mathbb{T}^{\frac{x_0}{a}} \mathcal{O}(x_0) \mathbb{T}^{\frac{z_0}{a}} |B\rangle\ , \tag{B.5}$$

where on the left the state $|\gamma\rangle$ is due to the use of OBC, and the state $|B\rangle$ on the right corresponds to the boundary term at x_0^B. As discussed in Sec. 4.4, we deal with OBC by performing all measurements in the plateau region in the centre of the lattice. To focus on the effect of the boundary B, let us assume that the effects from the open boundaries can be neglected[1]. Expanding the state $|B\rangle$ in a basis of eigenstates of the Hamiltonian we can write

$$[\mathcal{O}(x_0)]_L = \frac{e^{-E_0 x_0}}{\mathcal{Z}_L} \left(e^{-E_0 z_0} b_0 \langle 0| \mathcal{O}(x_0) |0\rangle + b_1 e^{-E_1 z_0} \langle 0| \mathcal{O}(x_0) |1\rangle + \mathrm{O}(e^{-E_2 z_0}) \right) , \tag{B.6}$$

where $b_i = \langle i|B\rangle$ are the projections of the boundary state on the basis of eigenstates of the Hamiltonian which corresponds to eigenstates with energy E_i. E_1 in Eq. (B.6) corresponds to the lowest energy of the states propagating from $|B\rangle$ compatible with the symmetries of $\mathcal{O}$. Similarly, to leading order one has $\mathcal{Z}_L = e^{-E_0 T/2} b_0$, so that

$$[\mathcal{O}(x_0)]_L \approx \langle 0| \mathcal{O}(x_0) |0\rangle + e^{-\Delta E_1 z_0} \left(\frac{b_1}{b_0} \right) \langle 0| \mathcal{O}(x_0) |1\rangle + \mathrm{O}(e^{-\Delta E_2 z_0}) , \tag{B.7}$$

where $\Delta E_i = E_i - E_0$.

Let us consider first the case of an observable with vanishing vacuum expectation value, such as $q(x_0)$, which is considered in Chapters 5 and 6. For this observable, the first term in Eq. (B.7) vanishes, and therefore, $[\mathcal{O}(x_0)]_L$ decays exponential with the distance to the boundary B. Clearly, the same is true for $[\mathcal{O}(y_0)]_R$, so that the term proportional to $1/n_0$ in Eq. (B.4) has the same decay rate with the distance between source and sink as the correlator itself. Similarly, the term proportional to $1/(n_0 n_1)$ in Eq. (B.4) is suppressed due to the presence of $[\mathcal{O}]_L$ and $[\mathcal{O}']_R$, provided that both x_0 and y_0 are sufficiently far from the boundary B[2]. On the other hand, as discussed in Ref. [17, 91], the signal to noise problem appears in the case where the variance of the correlator either remains constant with the distance, or decays

[1] In fact, all observables are measured after making sure that this is the case (see Sec. 4.4.1).

[2] Notice that if either source or sink are close to B, the term $e^{-\Delta E_1 z_0}$ might not be small enough to justify discarding the term proportional to $1/(n_0 n_1)$. In that case, one expects the errors in the multilevel update to scale the same way as those of the standard algorithm; a fact which is also discussed in the main text.

much slower than the signal itself. In this sense, the leading contribution must come from the first term proportional to $1/\left(n_0 n_1^2\right)$, provided both source and sink are sufficiently far away from B.

In the particular case of $q(x_0)$, once it is properly defined through the gradient flow, $\left\langle q^2(x_0)\right\rangle$ has a non-zero vacuum expectation value (see Figure 4.1), so $\Delta_L\left(q(x_0)\right) \approx \left\langle q^2(x_0)\right\rangle$, which means that the term proportional to $1/\left(n_0 n_1^2\right)$ in Eq. (B.4) remains constant with respect to the distance between source and sink in the correlator, and is therefore the leading contribution.

Let us now discuss the case where the operator $\mathcal{O}$ has a non-zero vacuum expectation value. In that case, the leading term in Eq. (B.6) is given by the vacuum expectation value itself $\langle 0|\,\mathcal{O}(x_0)\,|0\rangle$. For the term proportional to $1/n_0$ in Eq. (B.4) the vacuum expectation value of the observable is cancelled by $\bar{A}$, up to corrections that decay exponentially with the distance

$$\left\langle [\mathcal{O}]_L^2 \left[\mathcal{O}'\right]_R^2 \right\rangle_B - \bar{A}^2 = c\left(e^{-\Delta E_1 z_0}\right) + \mathrm{O}(e^{-\Delta E_2 z_0})\,, \tag{B.8}$$

where c is a numerical constant. Again, for this term to be subleading we require source and sink to be sufficiently far away from B. On the other hand, the term proportional to $1/\left(n_0 n_1\right)$, is not exponentially suppressed as the leading contribution from both $\left[\mathcal{O}\right]_L$ and $\Delta_L\left(\mathcal{O}\right)$ is O(1), which means that this term is of the same order as the one proportional to $1/\left(n_0 n_1^2\right)$. As discussed in the main text, for an observable with a non-zero vacuum expectation value, the term proportional to $1/(n_0 n_1)$ is only suppressed when the connected correlator is considered. In the following we list the terms required to evaluate Eq. (5.20)

$$\begin{aligned}\left\langle \left(\hat{A}-\bar{A}\right)\left(\hat{\mathcal{O}}-\bar{\mathcal{O}}\right)\right\rangle = \frac{1}{n_0 n_1}\left\langle \left[\mathcal{O}'\right]_R \Delta_L\left(\mathcal{O}\right)\right\rangle + \\ \frac{1}{n_0}\left(\left\langle \left[\mathcal{O}'\right]_R [\mathcal{O}]_L^2\right\rangle - \left\langle \left[\mathcal{O}'\right]_R [\mathcal{O}]_L\right\rangle \bar{\mathcal{O}}\right)\end{aligned} \tag{B.9}$$

$$\left\langle \left(\hat{\mathcal{O}}-\bar{\mathcal{O}}\right)\left(\hat{\mathcal{O}}'-\bar{\mathcal{O}}'\right)\right\rangle = \frac{1}{n_0}\left(\left\langle [\mathcal{O}]_L \left[\mathcal{O}'\right]_R\right\rangle - \bar{\mathcal{O}}\bar{\mathcal{O}}'\right) \tag{B.10}$$

$$\left\langle \left(\hat{\mathcal{O}}-\bar{\mathcal{O}}\right)^2\right\rangle = \frac{1}{n_0 n_1}\left\langle \Delta_L\left(\mathcal{O}\right)\right\rangle + \frac{1}{n_0}\left(\left\langle [\mathcal{O}]_L^2\right\rangle - \bar{\mathcal{O}}^2\right)\,, \tag{B.11}$$

and similarly for the terms where $\mathcal{O}$ is interchanged with $\mathcal{O}'$. Replacing these results into Eq. (5.20), one can check that the O(1) contributions cancel and one is left only with the terms that decay as $e^{-\Delta E_1 z_0}$. Note that when x_0 and y_0 are not at the same distance from the boundary B, z_0 must be replaced by $|x_0^B - x_0^M|$, where x_0^M is either x_0 or y_0, whichever is the closest to x_0^B.

C. β parametrization of t_0

Throughout this thesis we use the scale t_0 defined in Eq. (4.31) to match ensembles at different values of N. In practice, the only parameter to be tuned is the lattice coupling $\beta = 2N/g_0^2$, so we generated several ensembles for the different gauge groups at different β values in order to explore the β dependence of t_0. In all the cases, the configurations were generated with the hybrid over-relaxation algorithm with one update defined as N_{or} overrelaxation sweeps followed by one heatbath sweep of the full lattice. We report in Table C.1 the results of our preliminary measurements of t_0/a^2.

With this data, following the procedure from Ref. [136], the dependence of the scale t_0 on β is parametrized by a polynomial of the form

$$\ln\left(t_0/a^2\right) = \sum_{i=0}^{p} a_i \left(\beta - \beta_c\right)^i \,, \tag{C.1}$$

where β_c is chosen to shift the β values such that the fit formula has its intercept with zero in the range covered by our parameters [136]. We choose the values $\beta_c =$ 11.2, 17.8, 25.7 for SU(4), SU(5) and SU(6) respectively.

We include in the fit also the more precise values presented in Table 7.1. Notice that the error in such values is in some cases an order of magnitude smaller than those from Table C.1, so they will have the greater impact on the fit parameters. We find a good agreement with the data in the desired range using a fourth order polynomial, i.e., $p = 4$ in Eq. (C.1). The results for the interpolating fit formula are found to be

$$\ln\left(t_0/a^2\right) = \begin{cases} 1.6134 + 1.731\,(\beta - 11.2) - 0.21\,(\beta - 11.2)^2 + \\ 0.5\,(\beta - 11.2)^3 - 0.8\,(\beta - 11.2)^4 & \text{if} \quad N = 4 \\ 1.6904 + 1.120\,(\beta - 17.8) - 0.15\,(\beta - 17.8)^2 + \\ 0.026\,(\beta - 17.8)^3 + 0.09\,(\beta - 17.8)^4 & \text{if} \quad N = 5 \\ 1.58942 + 0.791\,(\beta - 25.7) - 0.53\,(\beta - 25.7)^2 + \\ 0.054\,(\beta - 25.7)^3 - 0.039\,(\beta - 25.7)^4 & \text{if} \quad N = 6\,. \end{cases} \tag{C.2}$$

N	β	$L/a \times T/a$	N_{meas}	N_{upd}	t_0/a^2
4	10.90	16×36	200	50	2.853(20)
4	11.10	20×42	200	80	4.206(22)
4	11.40	24×48	200	200	7.01(4)
4	11.70	32×72	160	300	11.48(4)
5	17.30	16×36	200	100	3.003(12)
5	17.60	20×42	200	100	4.272(19)
5	17.90	24×48	95	300	6.082(18)
5	18.40	32×72	240	400	10.26(4)
6	25.00	16×36	200	200	2.667(9)
6	25.40	20×42	200	200	3.827(14)
6	25.90	24×48	200	300	5.734(24)
6	26.50	32×72	80	500	9.03(4)

Table C.1: Preliminary simulations to measure the β dependence of the scale t_0/a^2.

The validity of Eq. (C.2) is only in the interpolating region, i.e., $\beta \in [10.90, 11.70]$ for SU(4), $\beta \in [17.30, 18.40]$ for SU(5), and $\beta \in [25.00, 26.50]$ for SU(6). For values of β in those ranges, we find the predictions of Eq. (C.2) to have errors on the per-mille level.

In order to display the interpolating equations in a single figure, we plot t_0/a^2 as a function of the inverse 't Hooft coupling $b = 1/\lambda = \beta/(2N^2)$. The data points and the result of the fit are shown in Figure C.1.

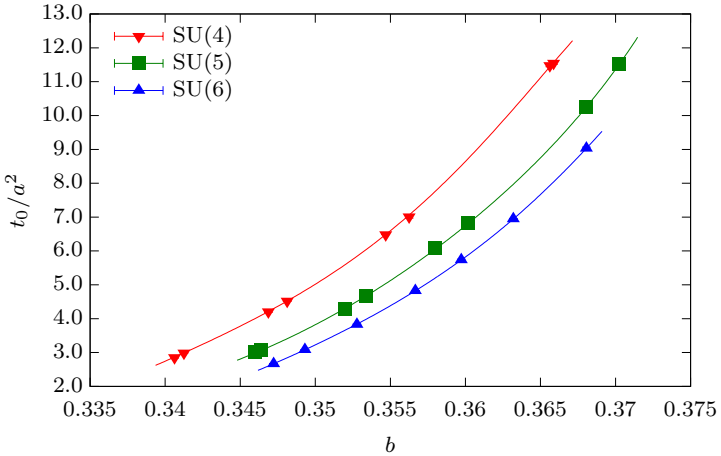

Figure C.1: Plot of t_0/a^2 as a function of the inverse 't Hooft coupling b and the fits from Eq. (C.2).

Bibliography

[1] K. G. Wilson, "Confinement of Quarks," *Phys. Rev.* **D10** (1974) 2445–2459. [,45(1974)].

[2] G. 't Hooft, "A Planar Diagram Theory for Strong Interactions," *Nucl. Phys.* **B72** (1974) 461.

[3] J. M. Maldacena, "The Large N limit of superconformal field theories and supergravity," *Int. J. Theor. Phys.* **38** (1999) 1113–1133, arXiv:hep-th/9711200 [hep-th]. [Adv. Theor. Math. Phys.2,231(1998)].

[4] S. S. Gubser, I. R. Klebanov, and A. M. Polyakov, "Gauge theory correlators from noncritical string theory," *Phys. Lett.* **B428** (1998) 105–114, arXiv:hep-th/9802109 [hep-th].

[5] E. Witten, "Anti-de Sitter space and holography," *Adv. Theor. Math. Phys.* **2** (1998) 253–291, arXiv:hep-th/9802150 [hep-th].

[6] S. S. Gubser and A. Karch, "From gauge-string duality to strong interactions: A Pedestrian's Guide," *Ann. Rev. Nucl. Part. Sci.* **59** (2009) 145–168, arXiv:0901.0935 [hep-th].

[7] J. Penedones, "TASI lectures on AdS/CFT," in *Proceedings, Theoretical Advanced Study Institute in Elementary Particle Physics: New Frontiers in Fields and Strings (TASI 2015): Boulder, CO, USA, June 1-26, 2015*, pp. 75–136. 2017. arXiv:1608.04948 [hep-th]. https://inspirehep.net/record/1481834/files/arXiv:1608.04948.pdf.

[8] **CP-PACS** Collaboration, S. Aoki *et al.*, "Quenched light hadron spectrum," *Phys. Rev. Lett.* **84** (2000) 238–241, arXiv:hep-lat/9904012 [hep-lat].

[9] G. S. Bali, F. Bursa, L. Castagnini, S. Collins, L. Del Debbio, B. Lucini, and M. Panero, "Mesons in large-N QCD," *JHEP* **06** (2013) 071, arXiv:1304.4437 [hep-lat].

[10] T. DeGrand and Y. Liu, "Lattice study of large N_c QCD," *Phys. Rev.* **D94** no. 3, (2016) 034506, arXiv:1606.01277 [hep-lat]. [Erratum: Phys. Rev.D95,no.1,019902(2017)].

[11] A. Athenodorou, R. Lau, and M. Teper, "On the weak N -dependence of SO(N) and SU(N) gauge theories in 2+1 dimensions," *Phys. Lett.* **B749** (2015) 448–453, arXiv:1504.08126 [hep-lat].

[12] A. Athenodorou, B. Bringoltz, and M. Teper, "Closed flux tubes and their string description in D=3+1 SU(N) gauge theories," *JHEP* **02** (2011) 030, arXiv:1007.4720 [hep-lat].

[13] B. Lucini and M. Panero, "SU(N) gauge theories at large N," *Phys. Rept.* **526** (2013) 93–163, arXiv:1210.4997 [hep-th].

[14] E. Witten, "THE 1 / N EXPANSION IN ATOMIC AND PARTICLE PHYSICS," *NATO Sci. Ser. B* **59** (1980) 403–419.

[15] S. R. Coleman, "1/N," in *17th International School of Subnuclear Physics: Pointlike Structures Inside and Outside Hadrons Erice, Italy, July 31-August 10, 1979*, p. 0011. 1980. http://www-public.slac.stanford.edu/sciDoc/docMeta.aspx?slacPubNumber=SLAC-PUB-2484.

[16] T. Eguchi and H. Kawai, "Reduction of Dynamical Degrees of Freedom in the Large N Gauge Theory," *Phys.Rev.Lett.* **48** (1982) 1063.

[17] G. Parisi, R. Petronzio, and F. Rapuano, "A Measurement of the String Tension Near the Continuum Limit," *Phys. Lett.* **B128** (1983) 418–420.

[18] M. Lüscher and P. Weisz, "Locality and exponential error reduction in numerical lattice gauge theory," *JHEP* **09** (2001) 010, arXiv:hep-lat/0108014 [hep-lat].

[19] G. 't Hooft, "A Two-Dimensional Model for Mesons," *Nucl. Phys.* **B75** (1974) 461–470.

[20] S. R. Wadia, "N = Infinity Phase Transition in a Class of Exactly Soluble Model Lattice Gauge Theories," *Phys. Lett.* **B93** (1980) 403–410.

[21] E. Brezin, C. Itzykson, G. Parisi, and J. B. Zuber, "Planar Diagrams," *Commun. Math. Phys.* **59** (1978) 35.

[22] G. Veneziano, "Some Aspects of a Unified Approach to Gauge, Dual and Gribov Theories," *Nucl. Phys.* **B117** (1976) 519–545.

[23] A. Chatterjee and D. Gangopadhyay, "FACTORIZATION IN LARGE N LIMIT OF LATTICE GAUGE THEORIES REVISITED," *Pramana* **21** (1983) 385–391.

[24] Y. Makeenko, "Large N gauge theories," arXiv:hep-th/0001047 [hep-th].

[25] Yu. M. Makeenko and A. A. Migdal, "Exact Equation for the Loop Average in Multicolor QCD," *Phys. Lett.* **B88** (1979) 135. [Erratum: Phys. Lett.B89,437(1980)].

[26] S. Chatterjee, "Rigorous solution of strongly coupled $SO(N)$ lattice gauge theory in the large N limit," arXiv:1502.07719 [math.PR].

[27] J. Jafarov, "Wilson loop expectations in $SU(N)$ lattice gauge theory," arXiv:1610.03821 [math.PR].

[28] S. Wadia, "A STUDY OF U(N) LATTICE GAUGE THEORY IN TWO-DIMENSIONS,".

[29] R. Gopakumar and D. J. Gross, "Mastering the master field," *Nucl. Phys.* **B451** (1995) 379–415, arXiv:hep-th/9411021 [hep-th].

[30] M. R. Douglas, "Stochastic master fields," *Phys. Lett.* **B344** (1995) 117–126, arXiv:hep-th/9411025 [hep-th].

[31] L. G. Yaffe, "Large n Limits as Classical Mechanics," *Rev. Mod. Phys.* **54** (1982) 407.

[32] G. Bhanot, U. M. Heller, and H. Neuberger, "The Quenched Eguchi-Kawai Model," *Phys. Lett.* **B113** (1982) 47–50.

[33] M. Okawa, "Monte Carlo Study of the Quenched Eguchi-kawai Model," *Phys. Rev. Lett.* **49** (1982) 705.

[34] J. Kiskis, R. Narayanan, and H. Neuberger, "Does the crossover from perturbative to nonperturbative physics in QCD become a phase transition at infinite N?," *Phys. Lett.* **B574** (2003) 65–74, arXiv:hep-lat/0308033 [hep-lat].

[35] P. Kovtun, M. Unsal, and L. G. Yaffe, "Volume independence in large N(c) QCD-like gauge theories," *JHEP* **06** (2007) 019, arXiv:hep-th/0702021 [HEP-TH].

[36] A. Gonzalez-Arroyo and M. Okawa, "The Twisted Eguchi-Kawai Model: A Reduced Model for Large N Lattice Gauge Theory," *Phys. Rev.* **D27** (1983) 2397.

[37] A. Gonzalez-Arroyo and M. Okawa, "A Twisted Model for Large N Lattice Gauge Theory," *Phys. Lett.* **B120** (1983) 174–178.

[38] A. Gonzalez-Arroyo and M. Okawa, "Large N reduction with the Twisted Eguchi-Kawai model," *JHEP* **07** (2010) 043, arXiv:1005.1981 [hep-th].

[39] M. Garcia Perez, A. Gonzalez-Arroyo, and M. Okawa, "Volume independence for Yang–Mills fields on the twisted torus," *Int. J. Mod. Phys.* **A29** no. 25, (2014) 1445001, arXiv:1406.5655 [hep-th].

[40] M. García Pérez, A. González-Arroyo, L. Keegan, and M. Okawa, "The $SU(\infty)$ twisted gradient flow running coupling," *JHEP* **01** (2015) 038, arXiv:1412.0941 [hep-lat].

[41] A. González-Arroyo and M. Okawa, "Large N meson masses from a matrix model," *Phys. Lett.* **B755** (2016) 132–137, arXiv:1510.05428 [hep-lat].

[42] M. Gell-Mann, "A Schematic Model of Baryons and Mesons," *Phys. Lett.* **8** (1964) 214–215.

[43] G. Zweig, "An SU(3) model for strong interaction symmetry and its breaking. Version 2," in *DEVELOPMENTS IN THE QUARK THEORY OF HADRONS. VOL. 1. 1964 - 1978*, D. Lichtenberg and S. P. Rosen, eds., pp. 22–101. 1964. http://inspirehep.net/record/4674/files/cern-th-412.pdf.

[44] L. Giusti, F. Rapuano, M. Talevi, and A. Vladikas, "The QCD chiral condensate from the lattice," *Nucl. Phys.* **B538** (1999) 249–277, arXiv:hep-lat/9807014 [hep-lat].

[45] F. Burger, V. Lubicz, M. Müller-Preussker, S. Simula, and C. Urbach, "Quark mass and chiral condensate from the Wilson twisted mass lattice quark propagator," *Phys. Rev.* **D87** no. 3, (2013) 034514, arXiv:1210.0838 [hep-lat]. [Phys. Rev.D87,079904(2013)].

[46] S. Weinberg, "The u(1) problem," *Phys. Rev. D* **11** (Jun, 1975) 3583–3593. http://link.aps.org/doi/10.1103/PhysRevD.11.3583.

[47] K. Fujikawa, "Path Integral Measure for Gauge Invariant Fermion Theories," *Phys. Rev. Lett.* **42** (1979) 1195–1198.

[48] S. L. Adler, "Axial vector vertex in spinor electrodynamics," *Phys. Rev.* **177** (1969) 2426–2438.

[49] J. S. Bell and R. Jackiw, "A PCAC puzzle: pi0 –> gamma gamma in the sigma model," *Nuovo Cim.* **A60** (1969) 47–61.

[50] S. L. Adler and W. A. Bardeen, "Absence of higher order corrections in the anomalous axial vector divergence equation," *Phys. Rev.* **182** (1969) 1517–1536.

[51] G. 't Hooft, "Symmetry Breaking Through Bell-Jackiw Anomalies," *Phys. Rev. Lett.* **37** (1976) 8–11.

[52] G. 't Hooft, "Computation of the Quantum Effects Due to a Four-Dimensional Pseudoparticle," *Phys. Rev.* **D14** (1976) 3432–3450. [Erratum: Phys. Rev.D18,2199(1978)].

[53] F. Bruckmann, "Topological objects in QCD," *Eur. Phys. J. ST* **152** (2007) 61–88, arXiv:0706.2269 [hep-th].

[54] K. Fujikawa, "Path Integral for Gauge Theories with Fermions," *Phys. Rev.* **D21** (1980) 2848. [Erratum: Phys. Rev.D22,1499(1980)].

[55] M. F. Atiyah and I. M. Singer, "The Index of elliptic operators. 1," *Annals Math.* **87** (1968) 484–530.

[56] E. Witten, "Current Algebra Theorems for the U(1) Goldstone Boson," *Nucl.Phys.* **B156** (1979) 269.

[57] G. Veneziano, "U(1) Without Instantons," *Nucl.Phys.* **B159** (1979) 213–224.

[58] P. Herrera-Siklody, J. I. Latorre, P. Pascual, and J. Taron, "Chiral effective Lagrangian in the large N(c) limit: The Nonet case," *Nucl. Phys.* **B497** (1997) 345–386, arXiv:hep-ph/9610549 [hep-ph].

[59] H. Leutwyler and A. V. Smilga, "Spectrum of Dirac operator and role of winding number in QCD," *Phys. Rev.* **D46** (1992) 5607–5632.

[60] T. Schäfer and E. V. Shuryak, "Instantons in QCD," *Rev. Mod. Phys.* **70** (1998) 323–426, arXiv:hep-ph/9610451 [hep-ph].

[61] L. Giusti, G. C. Rossi, M. Testa, and G. Veneziano, "The U(A)(1) problem on the lattice with Ginsparg-Wilson fermions," *Nucl. Phys.* **B628** (2002) 234–252, arXiv:hep-lat/0108009 [hep-lat].

[62] E. Seiler, "Some more remarks on the Witten-Veneziano formula for the eta-prime mass," *Phys. Lett.* **B525** (2002) 355–359, arXiv:hep-th/0111125 [hep-th].

[63] E. Witten, "Baryons in the 1/n Expansion," *Nucl. Phys.* **B160** (1979) 57–115.

[64] R. Kaiser and H. Leutwyler, "Pseudoscalar decay constants at large N(c)," in *Nonperturbative methods in quantum field theory. Proceedings, Workshop, Adelaide, Australia, February 2-13, 1998*, pp. 15–29. 1998. arXiv:hep-ph/9806336 [hep-ph]. http://alice.cern.ch/format/showfull?sysnb=0281519.

[65] T. Feldmann, "Quark structure of pseudoscalar mesons," *Int. J. Mod. Phys.* **A15** (2000) 159–207, arXiv:hep-ph/9907491 [hep-ph].

[66] **ALPHA** Collaboration, U. Wolff, "Monte Carlo errors with less errors," *Comput. Phys. Commun.* **156** (2004) 143–153, arXiv:hep-lat/0306017 [hep-lat]. [Erratum: Comput. Phys. Commun.176,383(2007)].

[67] M. Creutz, "Monte Carlo Study of Quantized SU(2) Gauge Theory," *Phys. Rev.* **D21** (1980) 2308–2315.

[68] N. Cabibbo and E. Marinari, "A New Method for Updating SU(N) Matrices in Computer Simulations of Gauge Theories," *Phys. Lett.* **B119** (1982) 387–390.

[69] A. D. Kennedy and B. J. Pendleton, "Improved Heat Bath Method for Monte Carlo Calculations in Lattice Gauge Theories," *Phys. Lett.* **B156** (1985) 393–399.

[70] K. Fabricius and O. Haan, "Heat Bath Method for the Twisted Eguchi-Kawai Model," *Phys. Lett.* **B143** (1984) 459–462.

[71] M. G. Pérez, A. González-Arroyo, L. Keegan, M. Okawa, and A. Ramos, "A comparison of updating algorithms for large N reduced models," *JHEP* **06** (2015) 193, arXiv:1505.05784 [hep-lat].

[72] K. M. Decker and P. de Forcrand, "PURE SU(2) LATTICE GAUGE THEORY ON 32**4 LATTICES," *Nucl. Phys. Proc. Suppl.* **17** (1990) 567–570.

[73] M. Creutz, "Overrelaxation and Monte Carlo Simulation," *Phys. Rev.* **D36** (1987) 515.

[74] F. R. Brown and T. J. Woch, "Overrelaxed Heat Bath and Metropolis Algorithms for Accelerating Pure Gauge Monte Carlo Calculations," *Phys. Rev. Lett.* **58** (1987) 2394.

[75] P. de Forcrand and O. Jahn, "Monte Carlo overrelaxation for SU(N) gauge theories," in *QCD and numerical analysis III. Proceedings, 3rd International Workshop, Edinburgh, UK, June 30-July 4, 2003*, pp. 67–73. 2005.

arXiv:hep-lat/0503041 [hep-lat]. http://inspirehep.net/record/679428/files/arXiv:hep-lat_0503041.pdf.

[76] **ALPHA** Collaboration, S. Schaefer, R. Sommer, and F. Virotta, "Critical slowing down and error analysis in lattice QCD simulations," *Nucl. Phys.* **B845** (2011) 93–119, arXiv:1009.5228 [hep-lat].

[77] L. Del Debbio, H. Panagopoulos, and E. Vicari, "theta dependence of SU(N) gauge theories," *JHEP* **08** (2002) 044, arXiv:hep-th/0204125 [hep-th].

[78] M. Lüscher, "Properties and uses of the Wilson flow in lattice QCD," *JHEP* **08** (2010) 071, arXiv:1006.4518 [hep-lat]. [Erratum: JHEP03,092(2014)].

[79] **ALPHA** Collaboration, M. Bruno, S. Schaefer, and R. Sommer, "Topological susceptibility and the sampling of field space in $N_f = 2$ lattice QCD simulations," *JHEP* **08** (2014) 150, arXiv:1406.5363 [hep-lat].

[80] M. Lüscher and S. Schaefer, "Lattice QCD without topology barriers," *JHEP* **07** (2011) 036, arXiv:1105.4749 [hep-lat].

[81] R. Narayanan and H. Neuberger, "Infinite N phase transitions in continuum Wilson loop operators," *JHEP* **03** (2006) 064, arXiv:hep-th/0601210 [hep-th].

[82] M. Lüscher and P. Weisz, "Perturbative analysis of the gradient flow in non-abelian gauge theories," *JHEP* **02** (2011) 051, arXiv:1101.0963 [hep-th].

[83] M. Lüscher, "Future applications of the Yang-Mills gradient flow in lattice QCD," *PoS* **LATTICE2013** (2014) 016, arXiv:1308.5598 [hep-lat].

[84] A. Ramos, "The Yang-Mills gradient flow and renormalization," *PoS* **LATTICE2014** (2015) 017, arXiv:1506.00118 [hep-lat].

[85] M. Lüscher and P. Weisz, "Computation of the relation between the bare lattice coupling and the MS coupling in SU(N) gauge theories to two loops," *Nucl. Phys.* **B452** (1995) 234–260, arXiv:hep-lat/9505011 [hep-lat].

[86] B. Alles, A. Feo, and H. Panagopoulos, "The Three loop Beta function in SU(N) lattice gauge theories," *Nucl. Phys.* **B491** (1997) 498–512, arXiv:hep-lat/9609025 [hep-lat].

[87] S. Borsanyi *et al.*, "High-precision scale setting in lattice QCD," *JHEP* **09** (2012) 010, arXiv:1203.4469 [hep-lat].

[88] R. Sommer, "Scale setting in lattice QCD," *PoS* **LATTICE2013** (2014) 015, arXiv:1401.3270 [hep-lat].

[89] M. Cè, M. García Vera, L. Giusti, and S. Schaefer, "The topological susceptibility in the large- N limit of SU(N) Yang–Mills theory," *Phys. Lett.* **B762** (2016) 232–236, arXiv:1607.05939 [hep-lat].

[90] T. DeGrand, "Simple chromatic properties of gradient flow," arXiv:1701.00793 [hep-lat].

[91] G. P. Lepage, "The Analysis of Algorithms for Lattice Field Theory," in *Boulder ASI 1989:97-120*, pp. 97–120. 1989. http://alice.cern.ch/format/showfull?sysnb=0117836.

[92] H. B. Meyer, "Locality and statistical error reduction on correlation functions," *JHEP* **01** (2003) 048, arXiv:hep-lat/0209145 [hep-lat].

[93] M. García Vera and S. Schaefer, "Multilevel algorithm for flow observables in gauge theories," *Phys. Rev.* **D93** (2016) 074502, arXiv:1601.07155 [hep-lat].

[94] **MILC** Collaboration, A. Bazavov *et al.*, "Topological susceptibility with the asqtad action," *Phys. Rev.* **D81** (2010) 114501, arXiv:1003.5695 [hep-lat].

[95] A. Chowdhury, A. Harindranath, and J. Maiti, "Open Boundary Condition, Wilson Flow and the Scalar Glueball Mass," *JHEP* **06** (2014) 067, arXiv:1402.7138 [hep-lat].

[96] S. Necco and R. Sommer, "The N(f) = 0 heavy quark potential from short to intermediate distances," *Nucl. Phys.* **B622** (2002) 328–346, arXiv:hep-lat/0108008 [hep-lat].

[97] M. Cè, C. Consonni, G. P. Engel, and L. Giusti, "Non-Gaussianities in the topological charge distribution of the SU(3) Yang–Mills theory," *Phys. Rev.* **D92** no. 7, (2015) 074502, arXiv:1506.06052 [hep-lat].

[98] M. Cè, M. García Vera, L. Giusti, and S. Schaefer, "The large N limit of the topological susceptibility of Yang-Mills gauge theory," *PoS* **LATTICE2016** (2016) 350, arXiv:1610.08797 [hep-lat].

[99] B. Lucini and M. Teper, "SU(N) gauge theories in four-dimensions: Exploring the approach to N = infinity," *JHEP* **06** (2001) 050, arXiv:hep-lat/0103027 [hep-lat].

[100] B. Lucini, M. Teper, and U. Wenger, "Topology of SU(N) gauge theories at T = 0 and T = T(c)," *Nucl. Phys.* **B715** (2005) 461–482, arXiv:hep-lat/0401028 [hep-lat].

[101] C. Bonati and M. D'Elia, "Comparison of the gradient flow with cooling in $SU(3)$ pure gauge theory," *Phys. Rev.* **D89** no. 10, (2014) 105005, arXiv:1401.2441 [hep-lat].

[102] C. Alexandrou, A. Athenodorou, and K. Jansen, "Topological charge using cooling and the gradient flow," *Phys. Rev.* **D92** no. 12, (2015) 125014, arXiv:1509.04259 [hep-lat].

[103] N. Cundy, M. Teper, and U. Wenger, "Topology and chiral symmetry breaking in SU(N(c)) gauge theories," *Phys. Rev.* **D66** (2002) 094505, arXiv:hep-lat/0203030 [hep-lat].

[104] M. Lüscher, "Topology of Lattice Gauge Fields," *Commun. Math. Phys.* **85** (1982) 39.

[105] A. Phillips and D. Stone, "Lattice Gauge Fields, Principal Bundles and the Calculation of Topological Charge," *Commun. Math. Phys.* **103** (1986) 599–636.

[106] M. J. Teper, "Physics from the lattice: Glueballs in QCD: Topology: SU(N) for all N," in *Confinement, duality, and nonperturbative aspects of QCD. Proceedings, NATO Advanced Study Institute, Newton Institute Workshop, Cambridge, UK, June 23-July 4, 1997*, pp. 43–74. 1997. arXiv:hep-lat/9711011 [hep-lat]. http://alice.cern.ch/format/showfull?sysnb=0261667.

[107] K. Osterwalder and R. Schrader, "AXIOMS FOR EUCLIDEAN GREEN'S FUNCTIONS," *Commun. Math. Phys.* **31** (1973) 83–112.

[108] K. Osterwalder and R. Schrader, "Axioms for Euclidean Green's Functions. 2.," *Commun. Math. Phys.* **42** (1975) 281.

[109] M. Teper, "Instantons in the Quantized SU(2) Vacuum: A Lattice Monte Carlo Investigation," *Phys. Lett.* **B162** (1985) 357–362.

[110] H. B. Nielsen and M. Ninomiya, "No Go Theorem for Regularizing Chiral Fermions," *Phys. Lett.* **B105** (1981) 219–223.

[111] P. H. Ginsparg and K. G. Wilson, "A Remnant of Chiral Symmetry on the Lattice," *Phys. Rev.* **D25** (1982) 2649.

[112] H. Neuberger, "Exactly massless quarks on the lattice," *Phys. Lett.* **B417** (1998) 141–144, arXiv:hep-lat/9707022 [hep-lat].

[113] M. Lüscher, "Exact chiral symmetry on the lattice and the Ginsparg-Wilson relation," *Phys. Lett.* **B428** (1998) 342–345, arXiv:hep-lat/9802011 [hep-lat].

[114] L. Del Debbio, L. Giusti, and C. Pica, "Topological susceptibility in the SU(3) gauge theory," *Phys. Rev. Lett.* **94** (2005) 032003, arXiv:hep-th/0407052 [hep-th].

[115] K. Fujikawa, "A Continuum limit of the chiral Jacobian in lattice gauge theory," *Nucl. Phys.* **B546** (1999) 480–494, arXiv:hep-th/9811235 [hep-th].

[116] R. Sommer, "A New way to set the energy scale in lattice gauge theories and its applications to the static force and alpha-s in SU(2) Yang-Mills theory," *Nucl. Phys.* **B411** (1994) 839–854, arXiv:hep-lat/9310022 [hep-lat].

[117] C. J. Morningstar and M. J. Peardon, "The Glueball spectrum from an anisotropic lattice study," *Phys. Rev.* **D60** (1999) 034509, arXiv:hep-lat/9901004 [hep-lat].

[118] C. Bonati, M. D'Elia, P. Rossi, and E. Vicari, "θ dependence of 4D $SU(N)$ gauge theories in the large-N limit," *Phys. Rev.* **D94** no. 8, (2016) 085017, arXiv:1607.06360 [hep-lat].

[119] A. Amato, G. Bali, and B. Lucini, "Topology and glueballs in $SU(7)$ Yang-Mills with open boundary conditions," *PoS* **LATTICE2015** (2016) 292, arXiv:1512.00806 [hep-lat].

[120] V. S. Dotsenko and S. N. Vergeles, "Renormalizability of Phase Factors in the Nonabelian Gauge Theory," *Nucl. Phys.* **B169** (1980) 527–546.

[121] R. A. Brandt, F. Neri, and M.-a. Sato, "Renormalization of Loop Functions for All Loops," *Phys. Rev.* **D24** (1981) 879.

[122] H. Dorn, "Renormalization of Path Ordered Phase Factors and Related Hadron Operators in Gauge Field Theories," *Fortsch. Phys.* **34** (1986) 11–56.

[123] R. Lohmayer and H. Neuberger, "Rectangular Wilson Loops at Large N," *JHEP* **08** (2012) 102, arXiv:1206.4015 [hep-lat].

[124] A. Gonzalez-Arroyo and M. Okawa, "The string tension from smeared Wilson loops at large N," *Phys. Lett.* **B718** (2013) 1524–1528, arXiv:1206.0049 [hep-th].

[125] R. Lohmayer and H. Neuberger, "Non-analyticity in scale in the planar limit of QCD," *Phys. Rev. Lett.* **108** (2012) 061602, arXiv:1109.6683 [hep-lat].

[126] M. Lüscher and S. Schaefer, "openQCD simulation program for lattice QCD with open boundary conditions." http://luscher.web.cern.ch/luscher/openQCD/, used version: openQCD-1.2, may 2013.

[127] I. Omelyan, I. Mryglod, and R. Folk, "Symplectic analytically integrable decomposition algorithms: classification, derivation, and application to molecular dynamics, quantum and celestial mechanics simulations," *Computer Physics Communications* **151** (2003) 272–314.

[128] M. Lüscher, "Schwarz-preconditioned HMC algorithm for two-flavor lattice QCD," *Computer Physics Communications* **165** no. 3, (2005) 199 – 220. http://www.sciencedirect.com/science/article/pii/S0010465504005016.

[129] M. Lüscher, "DD-HMC algorithm for two-flavour lattice QCD." http://http://luscher.web.cern.ch/luscher/DD-HMC/, used version: DD-HMC-1.2.2, sept. 2008.

[130] G. Amdahl, "Validity of the single-processor approach to achieving large-scale computing capabilities," pp. 483–485. 1967.

[131] **Alpha** Collaboration, G. de Divitiis, R. Frezzotti, M. Guagnelli, M. Lüscher, R. Petronzio, R. Sommer, P. Weisz, and U. Wolff, "Universality and the approach to the continuum limit in lattice gauge theory," *Nucl. Phys.* **B437** (1995) 447–470, arXiv:hep-lat/9411017 [hep-lat].

[132] M. Creutz and K. J. M. Moriarty, "Phase transition in su(6) lattice gauge theory," *Phys. Rev. D* **25** (Mar, 1982) 1724–1726. http://link.aps.org/doi/10.1103/PhysRevD.25.1724.

[133] L. Del Debbio, H. Panagopoulos, P. Rossi, and E. Vicari, "Spectrum of confining strings in SU(N) gauge theories," *JHEP* **0201** (2002) 009, arXiv:hep-th/0111090 [hep-th].

[134] C. Allton, M. Teper, and A. Trivini, "On the running of the bare coupling in SU(N) lattice gauge theories," *JHEP* **0807** (2008) 021, arXiv:0803.1092 [hep-lat].

[135] A. Ramos and S. Sint, "Symanzik improvement of the gradient flow in lattice gauge theories," *Eur. Phys. J.* **C76** no. 1, (2016) 15, arXiv:1508.05552 [hep-lat].

[136] **ALPHA** Collaboration, M. Guagnelli, R. Sommer, and H. Wittig, "Precision computation of a low-energy reference scale in quenched lattice QCD," *Nucl. Phys.* **B535** (1998) 389–402, arXiv:hep-lat/9806005 [hep-lat].

List of publications

- **M. García Vera and S. Schaefer**, "Multilevel algorithm for flow observables in gauge theories," Phys. Rev. D93 (2016) 074502, arXiv:1601.07155 [hep-lat].
- **M. Cè, M. García Vera, L. Giusti, and S. Schaefer**, "The topological susceptibility in the large- N limit of SU(N) Yang–Mills theory," Phys. Lett. B762 (2016) 232–236, arXiv:1607.05939 [hep-lat].
- **M. Cè, M. García Vera, L. Giusti, and S. Schaefer**, "The large N limit of the topological susceptibility of Yang-Mills gauge theory," PoS LATTICE2016 (2016) 350, arXiv:1610.08797 [hep-lat].

Selbständigkeitserklärung

Ich erkläre, dass ich die Dissertation selbständig und nur unter Verwendung der von mir gemäß §7 Abs. 3 der Promotionsordnung der Mathematisch-Naturwissenschaftlichen Fakultät, veröffentlicht im Amtlichen Mitteilungsblatt der Humboldt-Universität zu Berlin Nr. 126/2014 am 18.11.2014, angegebenen Hilfsmittel angefertigt habe.

Berlin, 16.03.2017 Miguel García Vera